

UNIVERSIDADE DE SÃO PAULO
INSTITUTO DE ENERGIA E AMBIENTE
PROGRAMA DE PÓS-GRADUAÇÃO EM ENERGIA

RENAN DE SOUZA CARVALHO

**MODELING AND SIMULATION OF A SOLAR CAVITY RECEIVER FOR LOW
LATITUDES**

SÃO PAULO

2020

RENAN DE SOUZA CARVALHO

MODELING AND SIMULATION OF A SOLAR CAVITY RECEIVER FOR LOW LATITUDES

Dissertação apresentada ao Programa de Pós-Graduação em Energia da Universidade de São Paulo para obtenção do título de Mestre em Ciências

Orientador: Prof. Dr. José Roberto Simões Moreira

Versão Corrigida

(Versão original disponível na Biblioteca do Instituto de Energia e Ambiente e na Biblioteca Digital de Teses e Dissertações da USP)

SÃO PAULO

2020

AUTORIZO A REPRODUÇÃO E DIVULGAÇÃO TOTAL OU PARCIAL DESTES TRABALHOS, POR QUALQUER MEIO CONVENCIONAL OU ELETRÔNICO, PARA FINS DE ESTUDO E PESQUISA, DESDE QUE CITADA A FONTE.

FICHA CATALOGRÁFICA

Carvalho, Renan de Souza.

Modelagem e simulação de um receptor solar de cavidade para baixas latitudes. / Renan de Souza Carvalho; orientador: José Roberto Simões Moreira. – São Paulo, 2020.

122 f.: il; 30 cm.

Dissertação (Mestrado em Ciências) – Programa de Pós-Graduação em Energia – Instituto de Energia e Ambiente da Universidade de São Paulo.

1. Energia solar. 2. Fontes alternativas e energia. 3. Fontes renováveis de energia. Título.

Elaborado por Maria Penha da Silva Oliveira CRB-8/6961

AGRADECIMENTOS

Primeiramente agradeço aos meus pais, José Aduino de Carvalho, Elaine Calegari de Souza Carvalho, Roberto Cardoso de Oliveira, e Roseli Calegari de Oliveira, que sempre me ajudaram e ampararam, principalmente nas fases mais difíceis.

Agradeço também aos meus orientadores, Prof. Simões e Prof. Celso Oliveira, que em muito me ajudaram durante todo o trabalho, e também ao Dr. Gilles Maag, que tanto me ensinou sobre modelagem matemática e simulação numérica, com toda calma e paciência existente no mundo.

Agradeço também aos colegas presentes no desenvolvimento do trabalho, tanto do Laboratório de Eficiência Energética e Simulação de Processos (LEESP) em Pirassununga, quanto do Laboratório de Sistemas Energéticos Alternativos (SISEA), em São Paulo, sem me esquecer do grande amigo Maicon Danilo Bastos pelas boas conversas durante as refeições que nos ajudam a aliviar o estresse de todo dia.

Agradeço, por fim, aos meus colegas de classe do IEE, aos professores, aos membros da secretaria de pós-graduação que tanto me ajudaram na busca de recursos para apresentação de trabalhos em congressos, aos laboratórios de pesquisa e a todos demais que me ajudaram tanto nas disciplinas quanto na elaboração do trabalho.

RESUMO

CARVALHO, Renan de Souza. **Modelagem e simulação de um receptor solar de cavidade para baixas latitudes**, 2020, 122 f. Dissertação (Mestrado em Ciências) – Programa de Pós-Graduação em Energia da Universidade de São Paulo, São Paulo, 2020.

A energia solar concentrada, também conhecida como heliotérmica, vem sendo proposta como uma alternativa renovável promissora para diversificar a matriz elétrica brasileira. Atualmente, não existem usinas heliotérmicas em operação no Brasil. Entretanto, projetos de P&D estão em desenvolvimento. Neste contexto, o presente trabalho teve como objetivo analisar o comportamento receptor solar de cavidade para geração direta de vapor baseado na tecnologia SG4 a ser instalado em uma planta de receptor de torre central de 50 kW_{el}, atualmente em construção em Caiçara do Rio do Vento (RN), bem como possíveis melhorias (*Compound Parabolic Concentrator* – CPC, e janela de quartzo). A simulação transiente utilizou dados reais coletados no local, aplicando o método de elementos agrupados para discretização espacial da cavidade, e o método explícito de Euler para discretização temporal, bem como o Método de Volumes Finitos para as trocas de calor entre tubo e água em um segundo modelo, mais detalhado. A validação foi realizada através da comparação dos resultados com um modelo em regime permanente considerando dois dias diferentes, com diferentes valores de irradiação e horários. Os resultados apontaram perdas de calor por convecção desprezíveis em comparação com perdas por reflexão e re-irradiação. Os resultados apontaram também que a eficiência do receptor é superior à do receptor adjunto às melhorias estudadas. A eficiência térmica do modelo da cavidade foi 91.33% ao longo do dia, e 90.18% após a implementação do modelo do tubo, com geração de 1.898,93 kg e 1.883,54 kg de vapor, respectivamente. Os resultados da validação demonstraram boa concordância entre os modelos transiente e em regime permanente.

Palavras-chave: Energia solar concentrada; Torre central; Receptor solar de cavidade; Geração direta de vapor; Simulação transiente.

ABSTRACT

CARVALHO, Renan de Souza. **Modeling and Simulation of a Solar Cavity Receiver for Low Latitudes**, 2020, 122 f. Dissertation (MSc) – Graduate Program on Energy, Universidade de São Paulo, São Paulo, 2020.

Concentrated Solar Power (CSP) has been proposed as a promising renewable alternative to diversify the Brazilian electricity matrix. No CSP plants are operational in Brazil, but R&D projects are under development. In this context, the present work aimed to assess the behavior of a Direct Steam Generation (DSG) cavity receiver based on the SG4 technology to be installed in a 50 kW_{el} central tower receiver plant, currently under construction in Caiçara do Rio do Vento, RN, Brazil, and possible improvements. The transient simulation used real data collected at the site, applying the lumped-element method for cavity spatial discretization, and Euler forward method for temporal discretization, as well as the Finite Volume Method (FVM) for the heat transfer between the steel tube and water in a more detailed second model. Validation was carried out by comparison of results with a steady-state model considering two different days, with different irradiation values and times of the day. The results showed negligible convective heat losses compared to reflection and re-radiation losses. In addition, the receiver efficiency is higher than the receiver attached to the assessed improvements. The receiver thermal efficiency was 91.33% for the first model, and 90.18% for the detailed model, with 1,898.93 kg and 1,883.54 kg of steam generation, respectively. The validation results showed good agreement between the transient and steady-state models.

Keywords: Concentrated solar power; Central tower; Cavity receiver; Direct steam generation; Transient simulation.

LIST OF FIGURES

Figure 2.1 - Average annual growth in global oil demand over the years.	20
Figure 2.2 - Total final energy consumption in 2016.....	21
Figure 2.3 - Global share of electricity production in 2017.	22
Figure 2.4 - Global carbon dioxide emissions over the years.	23
Figure 2.5 - Domestic Energy Offer in 2017.....	24
Figure 2.6 - (a) Industry, (b) Transport and (c) Energy Consumptions by Source in 2017.....	24
Figure 2.7 - Brazilian Electricity Mix in 2017.	25
Figure 2.8 - Wind generation, in TWh, between 2007 and 2017.	26
Figure 3.1 - “Solar Engine One” parabolic trough assembly in Al Meadi, Egypt, 1913.	27
Figure 3.2 - “Solar Electricity Generating Systems” in California, USA.	28
Figure 3.3 - CSP technologies: (a) parabolic trough, (b) linear Fresnel, (c) solar tower, (d) dish concentrators.....	29
Figure 3.4 - Sun-earth relationships.	30
Figure 3.5 - Sun’s movement over the day in different seasons.....	31
Figure 3.6 - ASTM G-173 extraterrestrial, global and direct normal spectral irradiance.	31
Figure 3.7 - (a) Acceptance half-angle, aperture and absorber areas relation, and (b) parabolic trough.....	33
Figure 3.8 - Solar Two power plant with an external cylinder receiver.	35
Figure 3.9 – “T-type” heliostat configuration.	36
Figure 3.10 – (a) Sener’s 178m ² heliostat and (b) eSolar’s 2m ² tripod heliostat.	36
Figure 3.11 – DLR’s 9m ² rim drive heliostat.....	37
Figure 3.12 – Thermal storage flexibility in a CSP system over a day.....	38
Figure 3.13 – Gemasolar tower system configuration with two TES molten salt tanks.....	39
Figure 3.14 – DNI assessed by satellite – SWERA project.	40
Figure 3.15 – The SMILE project configurations: (a) 100 kW _{el} Pirassununga and (b) 50 kW _{el} Caiçara do Rio do Vento.	41
Figure 3.16 – Solar receivers: (a) external receiver (Pirassununga’s configuration) and (b) cavity receiver (Caiçara do Rio do Vento’s configuration).	42
Figure 3.17 – Caiçara do Rio do Vento schematic diagram.....	42
Figure 3.18 – “T x s” diagram with operational points.....	43
Figure 3.19 – Rim drive heliostat: (a) front and (b) back views, and (c) driving chain gear....	44
Figure 3.20 – Rim drive heliostat with primary and secondary axis.	44
Figure 3.21 – ANU’s SG4 original solar receiver.....	45
Figure 3.22 – Simplified demonstration of the receiver’s inclination of 11°.....	45
Figure 3.23 - External (left) and cavity (right) receivers.	49
Figure 3.24 – (a) Surrounding field and (b) polar field configurations.....	49
Figure 3.25 - (a) External cylindrical receiver used in Crescent Dunes (USA) and (b) cavity receiver used in PS10 (Spain).....	50
Figure 3.26 - (a) Reheater, Evaporator and Superheater physical locations; (b) Receiver heat input distribution over the surfaces.....	50
Figure 3.27 - (a) Open volumetric and (b) pressurized volumetric receiver.	52
Figure 3.28 - Solid-based graphite central receiver in Australia.	52
Figure 3.29 - Thermal losses results obtained by Fang et al. (2011) under windy conditions.	55
Figure 3.30 - Convective losses based on different cavity inclinations.....	58
Figure 3.31 - Prakash, Kedare & Nayak (2009) cavity receiver.	59

Figure 4.1 – (a) Caiçara’s tower and heliostat field, and (b) the cavity receiver in detail.	61
Figure 4.2 – Simplified geometry and dimensions.	62
Figure 4.3 – Energy balance in a small section of the tube.	65
Figure 4.4 – (a) All stagnant, and (b) large stagnant zone with small convective area.	67
Figure 4.5 – Overview of convection loss studies.	68
Figure 4.6 – Cavity receiver geometrical parameters.	70
Figure 4.7 – Thermal resistance concept for the tube and foam (cross section view of an infinitesimal element).	71
Figure 4.8 - Control volume for a Finite Volume Method.	76
Figure 4.9 – Bisection method algorithm.	78
Figure 4.10 – Separate models for the Solar Field, CPC and cavity receiver efficiency calculation.	82
Figure 4.11 – 3-D CPC-type attached to the solar receiver.	82
Figure 4.12 – Quartz transmittance as function of wavelength.	83
Figure 4.13 – Solar receiver and quartz window scheme.	84
Figure 5.1 – (a) DNI (blue) and Temperature (orange); and (b) wind speed at ground level (blue) and extrapolation (orange) variations throughout the day.	86
Figure 5.2 – Heliostat’s Cartesian positions (blue dots) in relation to the tower (red dot).	88
Figure 5.3 – Total, Section 1, and Section 2 efficiencies for May 16 th , 2018.	89
Figure 5.4 – COMSOL’s velocity profile, convective and stagnant zones within the receiver.	89
Figure 5.5 – COMSOL’s temperature profile in the cavity.	90
Figure 5.6 – Convective losses for both Sections.	91
Figure 5.7 – DNI, steel and foam temperatures for Section 1 and Section 2.	92
Figure 5.8 – DNI, “S1”, and “S2” temperature transient behavior on start-up (a), cloud passage (b), and shutdown (c).	93
Figure 5.9 – “S1” reflection, convection, re-radiation losses, and conduction added to outer convection losses.	94
Figure 5.10 – “S2” reflection, convection, re-radiation losses, and conduction added to outer convection losses.	95
Figure 5.11 – Sankey diagram for Section 1.	95
Figure 5.12 – Sankey diagram for Section 2.	96
Figure 5.13 – Energy, thermal losses, and incident radiation from solar field for Sections 1 and 2, for May 16 th , 2018.	96
Figure 5.14 – Incident radiation, thermal losses, and net power transferred to the water.	97
Figure 5.15 – Sankey diagram for the average thermal losses.	97
Figure 5.16 – DNI and water mass flow pattern throughout the day.	98
Figure 5.17 – Steel and ceramic foam temperatures, respectively, over the day for Section 1 (a) and (b), and Section 2, (c) and (d).	99
Figure 5.18 – Incident radiation, thermal losses, net heat to water, and thermal efficiency regarding the insulation length.	100
Figure 5.19 – Enthalpy criteria to select the number of elements for each Section.	101
Figure 5.20 – Steel tube and ceramic foam temperature patterns for May 16 th , 2018.	102
Figure 5.21 – DNI, “S1”, “S2”, and “S3” steel tube temperature transient behavior on start-up (a), cloud passage (b), and shutdown (c).	103
Figure 5.22 – DNI and water mass flow considering dynamic effects within the tube.	105
Figure 5.23 – Detailed DNI vs water mass flow.	105
Figure 5.24 – Sankey diagram for May 16 th , 2018, considering the dynamic effects within the tube.	106

Figure 5.25 – Variation of steam outlet temperature (a) and thermal efficiency (b) as function of inlet water mass flow and DNI.	107
Figure 5.26 – “T” and “SS” comparisons for (a) thermal efficiency, and (b) water mass flow, for January and June 21 st	108
Figure 5.27 – Collecting efficiency as function of the Concentration Factor.....	110
Figure 5.28 – CPC efficiency, flux and power ratios as functions of the Concentration Factor.	111
Figure 5.29 – Receiver efficiency as function of Concentration Factor.	111
Figure 5.30 – Total efficiency as function of Concentrating Factor.	112
Figure 5.31 – CPC efficiency as function of temperature and CPC radius.	113
Figure 5.32 – Fractional function curve fitting.	114
Figure 5.33 – DNI, steel and ceramic foam behaviors for May 16 th , 2018, applying a quartz window.	116
Figure 5.34 – Incident radiation from solar field, radiation from radiosity method, net heat transferred to water, and thermal losses.	116
Figure 5.35 – Sankey diagram for the quartz window.	117
Figure 5.36 – DNI and water flow for May 16 th , 2018, applying the quartz window.....	118

LIST OF TABLES

Table 3.1 – First central receiver demonstration projects.....	34
Table 3.2 – Temperature, pressure, specific enthalpy and entropy of the operational points.....	43
Table 3.3 – Most frequent use of energy and equipment in dairies.	47
Table 3.4 – Total energy consumption for different types of factories.	47
Table 3.5 – Main thermal processes for pasteurized milk.....	48
Table 4.1 – Coil dimensions for each section.	63
Table 4.2 – Coil mass for each section.....	63
Table 4.3 – Blanket insulation mass for each section.	64
Table 4.4 – Constants for the ensemble length scale.....	70
Table 4.5 – Thermal conduction and convection resistances for each Section.	72
Table 4.6 – Conduction and convection heat transfer equations for each Section.....	73
Table 4.7 – Energy balance equations for each Section.....	74
Table 4.8 – Caiçara parameters used in the CPC model.	80
Table 4.9 – Quartz window optical properties.....	83
Table 4.10 – Cavity optical properties.....	84
Table 5.1 – Thermal resistances applied in the model.	91
Table 5.2 – Pressure analysis results.	102
Table 5.3 – Incoming radiation on the window for each wavelength interval.....	115

ACRONYMS LIST

AM	Air Mass
ANU	Australian National University
ASTM	American Society for Testing and Materials
BNDES	<i>Banco Nacional de Desenvolvimento Econômico e Social</i>
CFD	Computational Fluid Dynamics
CPC	Compound Parabolic Concentrator
CSP	Concentrating Solar Power
DLR	German Aerospace Center
DNI	Direct Normal Irradiation
DSG	Direct Steam Generation
EPE	<i>Empresa de Pesquisa Energética</i>
FVM	Finite Volume Method
GDP	Gross Domestic Product
GREEN	Research Group on Recycling, Energy Efficiency and Numerical Simulation
HTF	Heat Transfer Fluid
IEA	International Energy Agency
LCoE	Levelized Cost of Electricity
MCRT	Monte-Carlo Ray Tracing
OECD	Organization for Economic Co-operation and Development
ORC	Organic Rankine Cycle
PLC	Programmable Logic Controller
PROINFA	<i>Programa de Incentivo às Fontes Alternativas de Energia</i>
R&D	Research and Development
REN21	Renewable Energy Policy Network for the 21 st Century
SEGS	Solar Electricity Generating Systems
SMILE Project	“Solar-hybrid microturbine systems for cogeneration in agro-industrial electricity and heat production” Project
SWERA	Solar and Wind Energy Resource Assessment
TES	Thermal Energy Storage
USP	<i>Universidade de São Paulo</i>

NOMENCLATURE

A_{ap}	Aperture area [m ²]
A_{cav}	Cavity area [m ²]
A_{ext}	Steel and foam external area [m ²]
A_{mirror}	Mirror area [m ²]
A_s	Surface area [m ²]
C	Concentration factor [-]
C_{CPC}	CPC concentration ratio [-]
\bar{c}_p	Average specific heat at constant pressure [kJ/kg.K]
dp	Pressure decay [Pa]
E_λ	Emittance per spectral band [-]
$e_{\lambda b}$	Incoming radiation per spectral band [W]
F	View factor [-]
f	Friction factor [-]
g	Gravity [m/s ²]
Gr	Grashof Number [-]
h	Enthalpy [kJ/kg.K]
\bar{h}	Average convective heat transfer coefficient [W/m ² .K]
k	Thermal conductivity [W/m.K]
L_c	Characteristic length [m]
L_t	Steel tube length [m]
\dot{m}	Mass flow rate [kg/s]
\bar{Nu}	Average Nusselt Number [-]
Pr	Prandtl Number [-]
\dot{q}_c	Radiation going into the cavity [W]
\dot{Q}_{conv}	Convection losses [W]
\dot{q}_{CPC}	CPC incoming flux [W/m ²]
\dot{Q}_{CPC}	CPC net power [W]
\dot{Q}_{inc}	Incident radiation from solar field [W]
\dot{Q}_{rad}	Re-radiation losses [W]
\dot{Q}_{ref}	Reflection losses [W]
\dot{q}_w	Radiation going back to the window [W]
r_{ap}	Aperture radius [m]
Ra_L	Rayleigh Number [-]

R_c	Convection resistance [W/K]
r_{CPC}	CPC radius [m]
r_e	External steel tube radius [m]
r_i	Internal steel tube radius [m]
R_k	Conduction resistance [W/K]
R_λ	Reflectance per spectral band [-]
s	Entropy [kJ/kg.K]
T_c	Ceramic foam temperature [K/°C]
T_s	Steel tube temperature [K/°C]
T_∞	Ambient temperature [K/°C]
u	Water/steam velocity [m/s]
V_λ	Transmittance per spectral band [-]
V_{rdx}	Element volume [m ³]
x_c	Ceramic foam length [m]

GREEK LETTERS

α	Thermal diffusivity [m ² /s]
β	Thermal expansion coefficient [1/K]
γ_{az}	Azimuth angle
δ	Flat plate inclination [°]
ε_{ap}	Apparent emissivity [-]
η_{Aap}	Aperture area efficiency [-]
η_{col}	Solar field collecting efficiency [-]
η_{cos}	Solar field cosine efficiency [-]
η_{CPC}	CPC efficiency [-]
η_{rec}	Receiver efficiency [-]
η_{ref}	Solar field reflective efficiency [-]
η_{sf}	Solar field efficiency [-]
θ	Cavity inclination [°]
θ_{max}	Maximum heat loss angle [°]
θ_{stag}	Stagnation angle [°]
ρ	Density [kg/m ³]
σ	Stefan-Boltzmann constant [W/m ² .K]
ν	Kinematic viscosity [m ² /s]
φ_{el}	Elevation angle
ϕ	Receiver inclination [°]

SUMMARY

1. Introduction	17
1.1. Justification	17
1.2. Objective	18
2. Global and Nationwide Energy Demand	20
2.1. Global Energy Demand	20
2.2. Brazilian Energy Mix.....	23
3. Literature Review	27
3.1. Historical Overview.....	27
3.2. Concentrating Solar Power	29
3.2.1. The Sun	30
3.2.2. Optical Concentration	32
3.3. Solar Tower Technology	33
3.3.1. The Heliostats.....	35
3.3.2. The Receiver	37
3.3.3. Storage and Hybridization	37
3.4. CSP in Brazil	39
3.4.1. The SMILE Project.....	40
3.5. Central Solar Receivers	48
3.5.1. The Cavity Receiver	53
4. Methodology	61
4.1. Meteorological Data	61
4.2. The Heliostat Field	61
4.3. The Receiver	62
4.3.1. The Receiver Properties	62
4.3.2. The Receiver Model.....	64
4.3.3. Ceramic Foam Sensitivity Analysis	75
4.3.4. Finite Volume Method.....	75
4.3.4. Model Comparison.....	79
4.4. The Compound Parabolic Concentrator (CPC) Receiver	79
4.5. The Quartz Window Receiver	82
5. Results and Discussion.....	86
5.1. Meteorological Data	86
5.2. The Heliostat Field	87
5.3. The Receiver.....	89

5.3.1. Thermal Model Results	89
5.3.2. Ceramic Foam Sensitivity Analysis	98
5.3.3. Finite Volume Method	100
5.3.4. Model Comparison.....	107
5.4. The Compound Parabolic Receiver.....	109
5.5. The Quartz Window Receiver	113
6. Conclusions	119
7. Future Work Recommendation	120
References	121
Appendix A	132
Appendix B	134
Appendix C	136
Appendix D.....	138

1. Introduction

1.1. Justification

Over the last years, the interest over renewable energy have been growing substantially, driven by environmental issues, the growing energy consumption (which grows essentially with several parameters such as world's population), and costs associated to it (NASCIMENTO; ALVES, 2016).

Nevertheless, *caveat emptor*, fossil fuels still represents the majority of final energy consumption worldwide, as well as for electricity generation (REN21, 2018). Hence, to face this, aiming a transition environment, a long-term consistent energy planning must be carried, added to public incentives for technological innovation regarding energy efficiency and alternatives to fossil fuels.

Concerning electricity generation, historically, the Brazilian mix has largely relied on hydropower. However, in the past years, a need for diversification of the electricity matrix has arisen, given the decreasing relative storage capacity (OLIVEIRA; SALOMÃO, 2017) of the hydro sector and its consequent increased vulnerability to seasonal drought phenomena (CASTRO, 2015).

Brazil has several regions have the benefit of high-level solar irradiation when compared to conventional sites, as can be noticed with the large expansion of installed photovoltaics (PV). Nevertheless, while the PV and wind power capacity in the Brazilian power grid is under way, the widespread use of those technologies entails the requirement of sufficient grid storage and backup capacity. CSP offers a mitigation of those issues, thanks to its more flexible dispatchability in combination with thermal energy storage.

Also, the industries, and in special agro-industry, are searching for new ways to produce their energy, environmentally friendly, looking for self-sufficiency, sustainability, and competitiveness improvement (BEZERRA; SERAPHIM; OLIVEIRA, 2018). In this context, CSP presents the possibility of process heat cogeneration, which can lead to cost reductions, e.g. for industrial or agro-industrial consumers.

Given these perspectives, pilot/demonstration endeavors aiming in this direction are under development, such as the SMILE ("Solar-hybrid micro-turbine

systems for cogeneration in agro-industrial electricity and heat production”) Project, specifically aiming at hybridization with bio-fuels and co-generation of heat for agro-industrial consumers.

In this framework, two pilot solar tower plants are currently under construction, one at the University of São Paulo campus in Pirassununga, São Paulo; and the other in Caiçara do Rio do Vento, Rio Grande do Norte (MAAG et al., 2015).

Nevertheless, is imperative to firstly simulate the power plant components, assessing how they would behave under realistic conditions. Regarding this, the present work target is to analyze the solar receiver to be applied in Caiçara do Rio do Vento, as explained ahead.

1.2. Objective

This work aims at numerically predicting and analyzing the transient response of the DSG solar receiver (system dynamics), under realistic irradiation and temperature conditions based on data collected at the installation site, as part of the SMILE project.

The goal of studying the dynamics of systems is to comprehend and predict its dynamic behavior, and sometimes improve it. There are three stages that characterize this study (GARCIA, 1997): obtain a mathematical model to represent the physical phenomenon which adapts accurately to the real system (an idealization); study the mathematical model dynamic behavior by simulation; and finally apply the model to solve a problem.

To reach this target, an accurate receiver model for the hybrid (phenomenological and empirical) modeling must be primarily made. Therefore, the following specific objectives shall be included:

- Model partially the heliostat field, considering the rim drive heliostat parameters and constraints, outputting the optimized field layout and efficiencies to calculate the incident radiation into the receiver;
- Derive a mathematical model for the physical receiver, considering its material, geometry, constraints and thermal losses to accurately predict the net thermal power absorbed by it in reality;

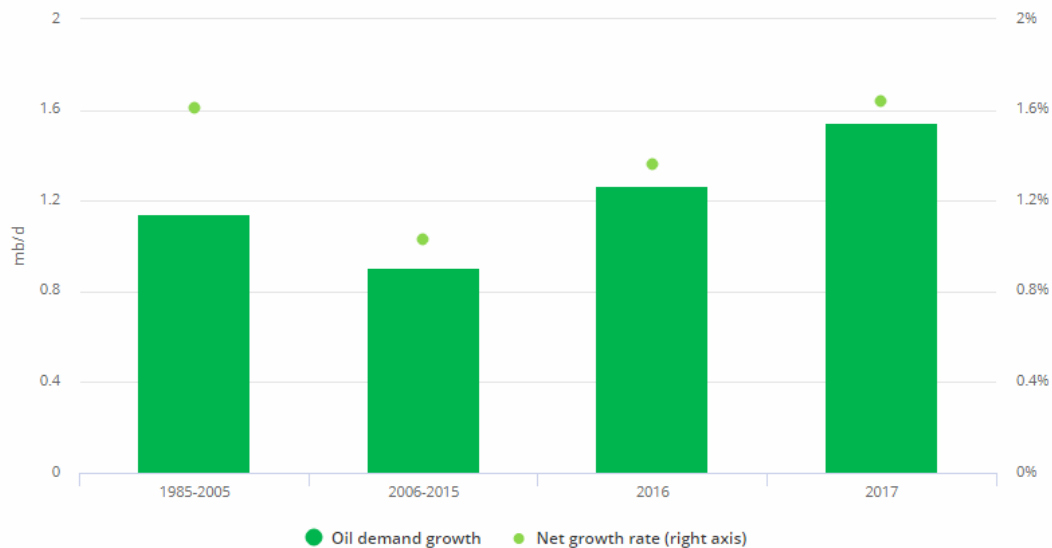
- Model and simulate the solar receiver adding a Compound Parabolic Concentrator (CPC);
- Model and simulate the solar receiver with a quartz window;
- Compare results of both improvements in relation to current receiver design.

2. Global and Nationwide Energy Demand

2.1. Global Energy Demand

Energy has been one of the main drivers of societies throughout the centuries, and in a historical point of view, by using natural resources such as wood to create heat, to cook, among others, energy has helped humans to evolve to a modern society with high patterns of life (HINRICHS; KLEINBACH, 2003). Through this evolution, fossil fuels were always present in daily human life. However, this presence and necessity were felt harshly with the 1973 oil embargo and its sequential shortages over the world, when oil represented 45% of the global energy mix, added to the Iranian Revolution in 1979 and the Persian Gulf War in 1991, which claimed the attention of how crucial oil was for the day-to-day modern society. Another crucial concern arose in that time concerning climate change, with CO₂ emissions, acid rain and radioactive residues that still alarm us, each one of them related to how energy is used nowadays (HINRICHS; KLEINBACH, 2003; IEA, 2017).

Figure 2.1 - Average annual growth in global oil demand over the years.



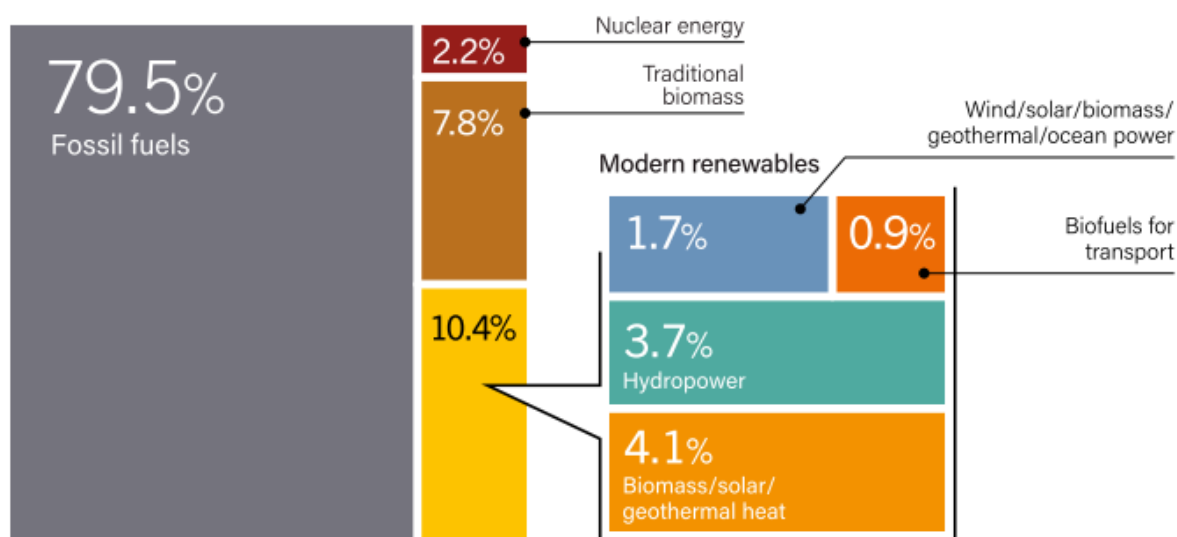
Source: IEA (2018).

The International Energy Agency World Energy Outlook Report from 2017 points out that oil still represents 32% of the global energy mix (IEA, 2017). Even though this decrease of the percentages gives us the perception of a decrease in dependency, the energy demand grew substantially over the years, *pari passu* with several different parameters (e.g. an increase of population). This can be noticed through the Figure 2.1 shown above, where the average annual growth in global oil

demand has risen since the oil embargo from slightly below 1.2 million barrels per day up to almost 1.6 million barrels per day.

Under this scope, according to REN21 “Global Status Report” from 2018, fossil fuels still make up the overwhelming majority in total final energy consumption in 2016, as shown in Figure 2.2. It’s possible to notice that the so called “modern renewables” represented only 10.4%, with biomass, solar and geothermal heat being the predominant ones among them; where traditional biomass, composed mainly of wood, shares 7.8%, which means that people still burns wood to cook or produce heat in obsolete equipment, which can cause health problems through its hazardous waste.

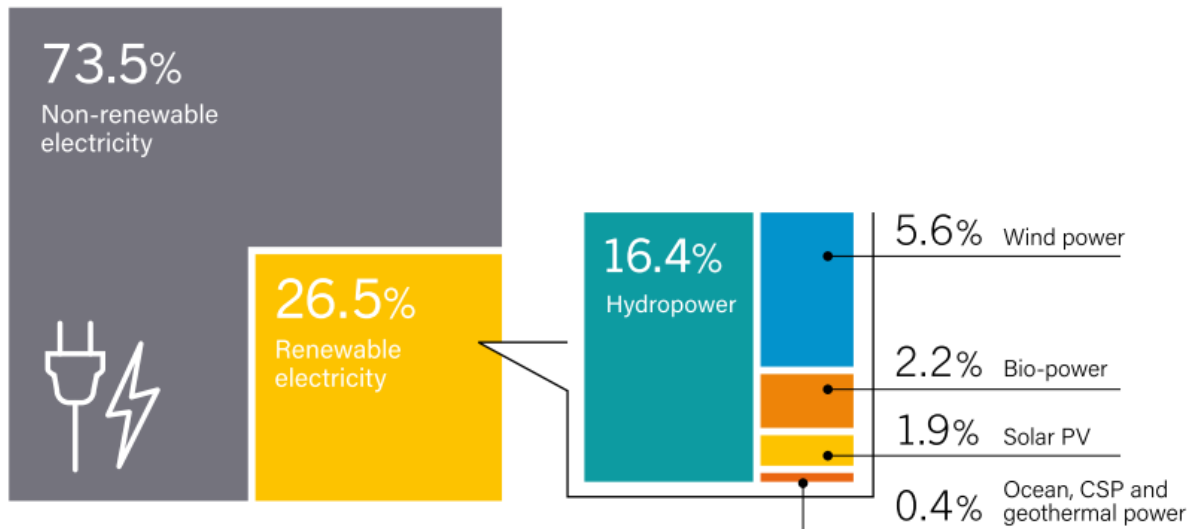
Figure 2.2 - Total final energy consumption in 2016.



Source: REN21 (2018).

Figure 2.3 shows the global share of electricity production in the end of 2017, where fossil fuels, like in primary energy consumption shown above, composes the biggest share, 73.5%. In renewable electricity, hydropower has the highest share, with 16.4%, followed by wind, with 5.6%. This scenario demonstrates how the world is still strongly dependent on fossil fuels. However, the REN21 report also presents 2017 as being the year with the largest increase in renewable power capacity; falling costs, especially wind and photovoltaic technologies; increases in investments; added to countries promising to become coal-free, like China.

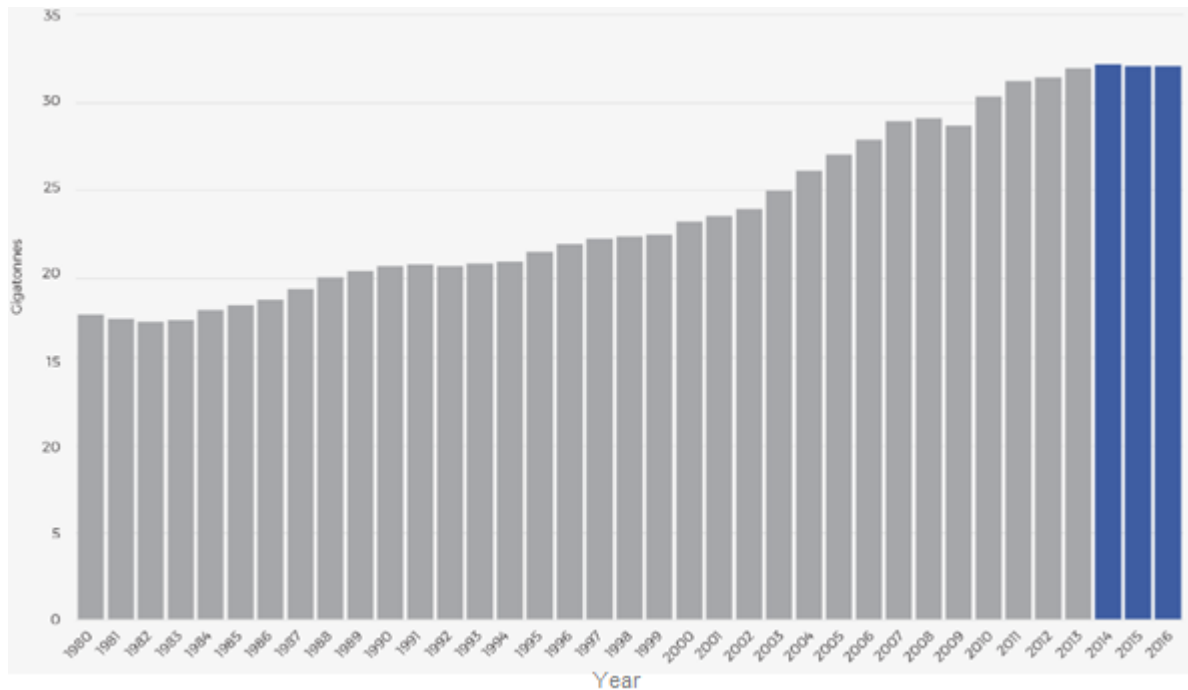
Figure 2.3 - Global share of electricity production in 2017.



Source: REN21 (2018).

Thus, the concerns with climate change are still in vogue, since carbon emissions have been rising over the years, as shown below in Figure 2.4. As can be seen, the global emissions were somewhere between 15 and 20 gigatons of CO₂, and in 2016 were slightly above 30 gigatons of CO₂. Another important aspect also shown below is that those emissions remained nearly flat since 2014, which could be perhaps a turnaround that can be explained by several factors like a fall in global coal use, especially in China, as mentioned above; a switch from oil to natural gas in USA; a reduction in energy intensity of gross domestic product (GDP) globally, i.e. less energy used to produce the same; improvements in energy efficiency; and a crucial factor that is the expansion of low-carbon power generation, where the main technologies are wind and solar photovoltaic (IEA, 2017; REN21, 2017). Nevertheless, in 2017, for the first time in four years, the emissions rose by 1.4%, in comparison with an estimated increase in energy demand of 2.1% (REN21, 2018).

Figure 2.4 - Global carbon dioxide emissions over the years.



Source: IEA (2018).

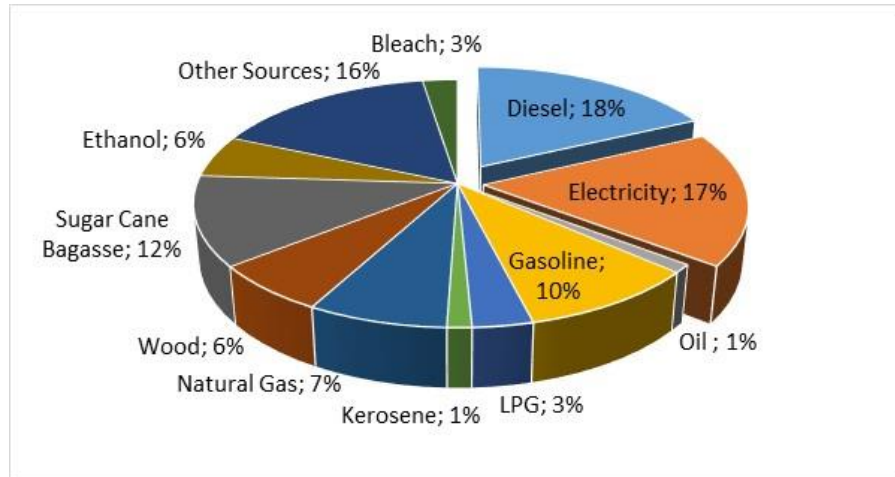
Traditionally, those previously presented assessments of data about energy were divided into the countries of the Organization for Economic Co-operation and Development (OECD) and non-OECD. However, this way of categorizing, which once made sense since developed countries used to be the major energy-consuming countries, no longer does, once developing countries such as Brazil, China, India, Morocco, among others, are now the drivers for the global energy demand growth (IEA, 2017), demanding special attention regarding the increasing demand and how to supply it in a sustainable way. Brazil, as an example, according to EPE (2016), will have an increasing electricity demand by an average of 3.1% yearly between 2013 and 2050, resulting in almost 1,500 TWh in the latter.

2.2. Brazilian Energy Mix

Brazil, similarly to the rest of the world, still relies on non-renewable sources to supply its domestic demand, which represented 56.8% of the Internal Energy Offer in 2017. According to the Energy Balance Report from 2018 provided by the Energetic Research Company (*“Empresa de Pesquisa Energética” – EPE*), in 2017 diesel composed the majority of that offer with 18%, followed closely by electricity with 17.4%, and sugar cane bagasse with 11.7%, as shown ahead in Figure 2.5. The other sources

are biodiesel, gasoline for aviation, gas from refinery, naphtha, asphalt, among others (EPE, 2018).

Figure 2.5 - Domestic Energy Offer in 2017.

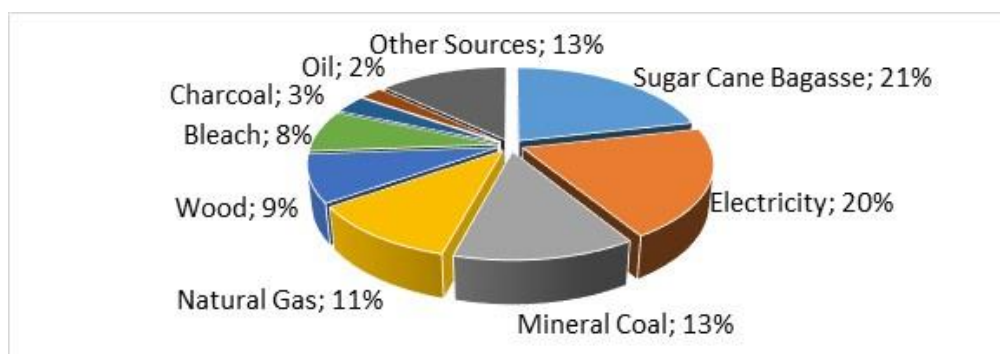


Source: The author, with data from EPE (2018).

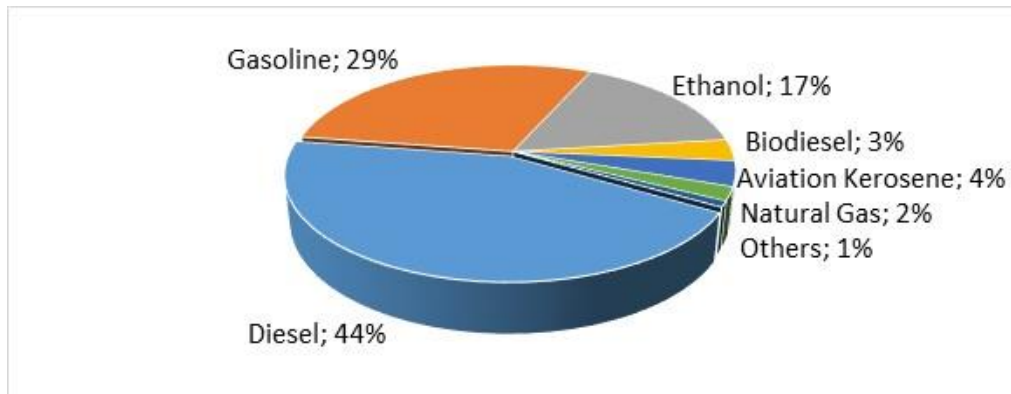
In this aspect, the higher consumers are the Industry and Transports sectors, which correspond to 33.3% and 32.5% of the total, respectively, followed by the Energy sector, with 10%, all represented below through Figures 2.6 (a), (b) and (c) (EPE, 2018). Through those shares, it's possible to notice that renewables were preponderant (only in the Transport sector renewable sources stayed underneath 50%), and the highlights stays with sugar cane bagasse, that represents 21% of the Industry consumption, and 17% of the Transport consumption through ethanol as the larger crop used to produce this byproduct, as well as in the electricity production, as will be shown in the next section, where the bagasse still represents a considerable share.

Figure 2.6 - (a) Industry, (b) Transport and (c) Energy Consumptions by Source in 2017.

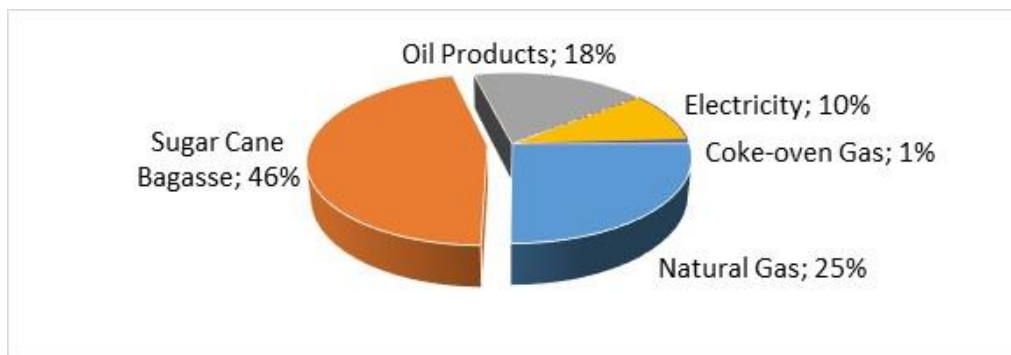
(a)



(b)



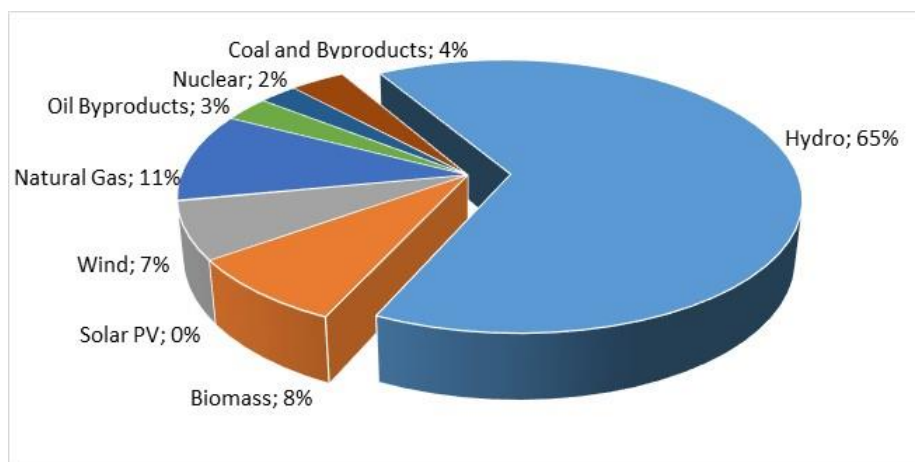
(c)



Source: The author, with data from EPE (2018).

When the subject is electricity generation, which represented 17% of the Internal Energy Offer in 2017, the matrix was essentially renewable (80.4%), which can be seen as a historical characteristic of the Brazilian matrix. The hydro generation, predominant source of power through the last century in Brazil, still claims its higher share, with 65.3%, as shown below in Figure 2.7.

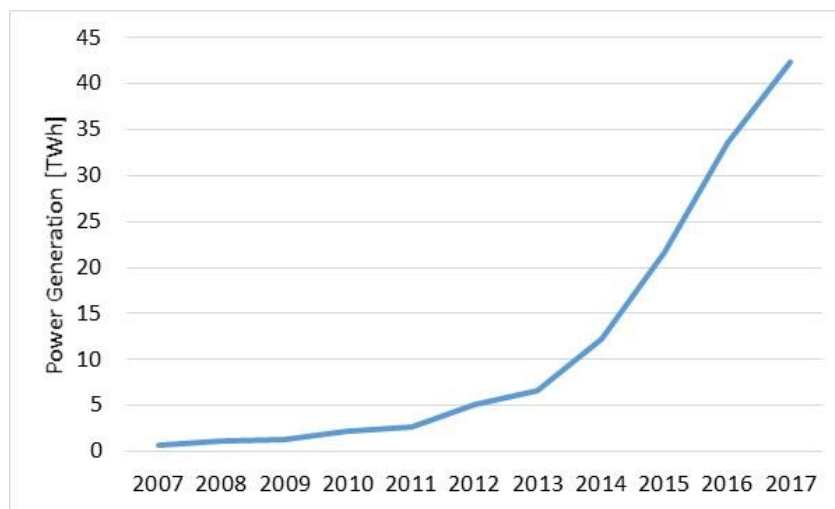
Figure 2.7 - Brazilian Electricity Mix in 2017.



Source: The author, with data from EPE (2018).

Nevertheless, the highlights of the last few years stays with the solar photovoltaic, with an increase in generation of 875.6% between 2016 and 2017, and wind generation, which had an exponential increase trend in generation (Figure 2.8). This development represents a natural tendency worldwide as abovementioned (e.g. “Energiewende”). In the Brazilian case, several energy policies, such as the Alternative Source of Energy Incentive Program (“*Programa de Incentivo às Fontes Alternativas de Energia*” – PROINFA), are being held to sustain the development of these modern renewables.

Figure 2.8 - Wind generation, in TWh, between 2007 and 2017.



Source: The author, with data from EPE (2018).

However, big hydro power plants are out of scope due to several environmental and social problems caused by flooding areas for big reservoirs. In addition, those intermittent energy sources presented above alone cannot support a sustainable supply for the growing domestic demand, as mentioned above to be of 3.1% yearly. Thus, dispatchable energy technologies that guarantee reliability to the grid such as CSP emerge as a possibility to turn that dispatch flexible throughout the day. The CSP technology is detailed discussed in [Chapter 3.2.2](#).

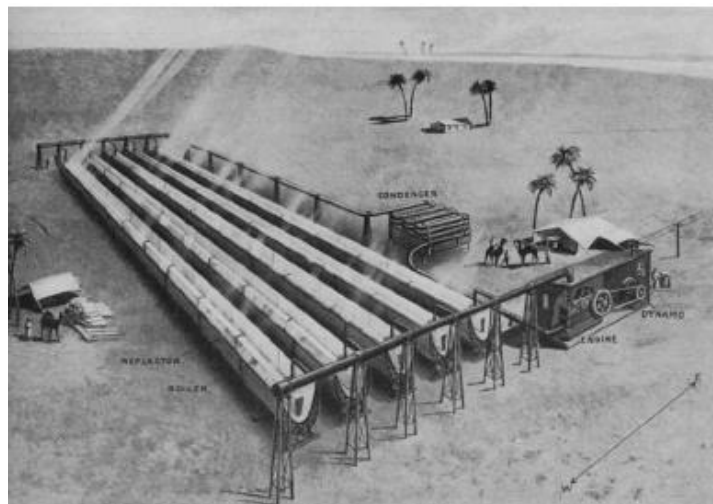
3. Literature Review

3.1. Historical Overview

The concentration concepts have been applied in several projects over time. A first application was described by Archimedes around 200 B.C., in which mirrors were used to concentrate the solar radiation. Subsequently, the Greek mathematician Diocles described the optical properties of a parabolic trough in the second century (LOVEGROVE; STEIN, 2012).

The first documented larger CSP project, however, was conducted by the North American engineer Frank Schuman in 1913, in Al Meadi, Egypt, called "Solar Engine One" (Figure 3.1). In such a system, five parabolic concentrators with 62 meters long and 4 meters of aperture equipped with a tracking system were used to pump water for irrigation, being able to pump 6,000 gallons of water per minute, equivalent to 27,260 liters per minute. The solar system achieved an efficiency of 4%, compared to the most advanced technology at the time, the steam engine, which had an efficiency of 10% (LOVEGROVE; STEIN, 2012; RAGHEB, 2014).

Figure 3.1 - "Solar Engine One" parabolic trough assembly in Al Meadi, Egypt, 1913.



Source: Ragheb (2014).

Thus, the use of the CSP concept for energy generation has been occurring for long now. Nevertheless, its birth as an industry for electricity generation dates from the end of the 20th century, driven by concerns regarding the previous mentioned external oil uncertainty and dependency of that time, where alternative energy sources such as CSP spurred to help out the growing energy demand (WAGNER, 2008; RAGHEB,

2014). In this context, through favorable governmental policies, in 1980, in the Mojave Desert in California started the implementation of the first CSP complex called “Solar Electricity Generating Systems” (SEGS) (Figure 3.2), composed by nine parabolic trough power plants with 354 MW_{el} of capacity. The first power plants used thermal oil as a heat transfer fluid (HTF), which transferred heat to water through heat exchangers, producing steam that expanded in a turbine in a common Rankine cycle (KALOGIROU, 2009; LOVEGROVE; STEIN, 2012).

Figure 3.2 - “Solar Electricity Generating Systems” in California, USA.



Source: Kalogirou (2009).

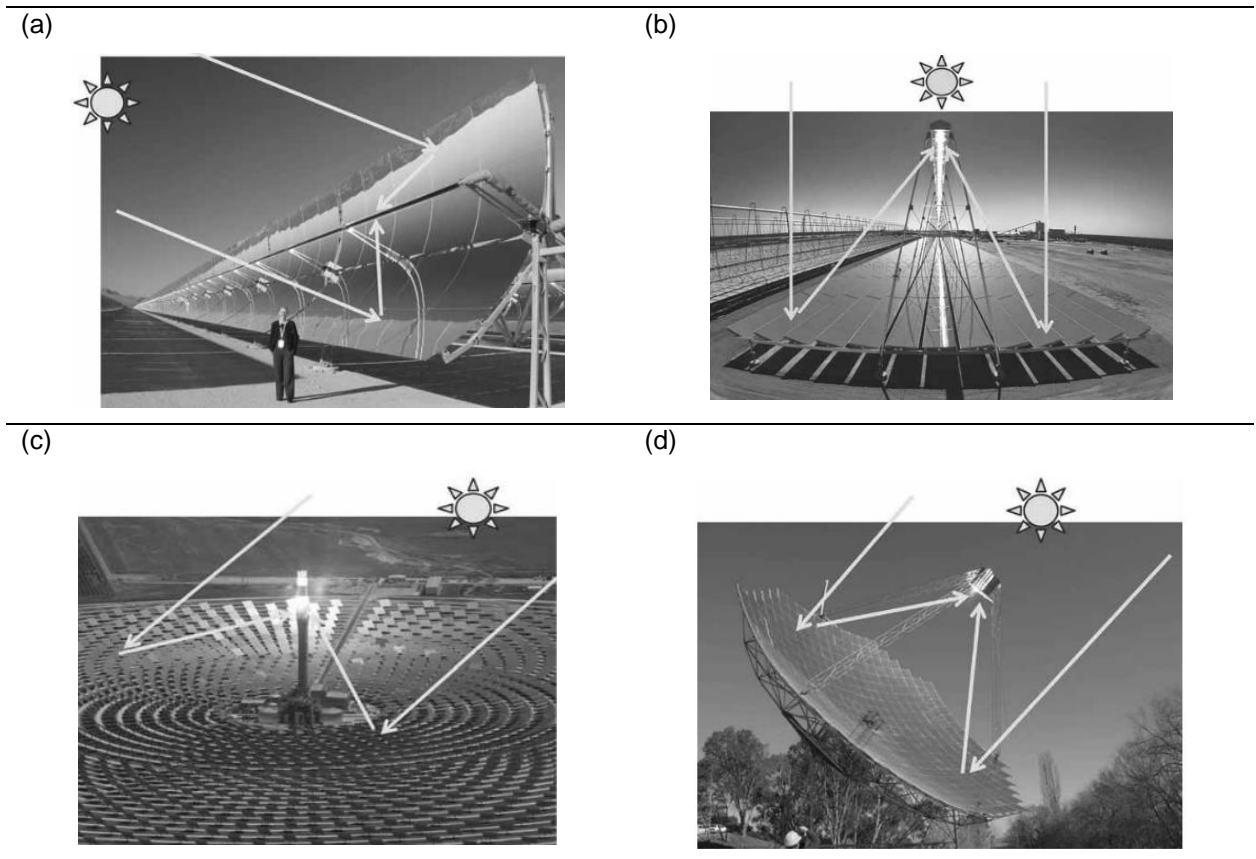
The fact that these solar plants with more than 2,000,000 m² of mirror area still being in operation establishes the CSP as a commercially proven technology with a high level of technical credibility and trust for investors and technology promoters. In addition, SEGS has also made possible the existence of an industry capable of satisfying the initial demand for essential components such as receiver tubes and reflecting mirrors (KALOGIROU, 2009; LOVEGROVE; STEIN, 2012).

Due to Research and Development (R&D), economy of scale, and accumulated experience, the cost of electricity generated, known as "Levelized Cost of Electricity" (LCoE), reduced from USD 0.30/kWh in 1985, when the first SEGS was built, to USD 0.14/kWh in 1989, when the seventh plant was built, representing a decrease of more than 50% in four years. In 2009 the plants had already generated more than 15,000 GWh, of which 12,000 GWh were generated only from solar energy (SEGS had hybridization through natural gas for periods of intermittence), which represented around \$2 billion of electricity sold over the years mentioned (KALOGIROU, 2009).

3.2. Concentrating Solar Power

The CSP technology consists of mirrors or lenses that concentrate the Direct Normal Irradiation (DNI) onto a receiver that can be punctual or longitudinal (Figure 3.3) by tracking the Sun throughout the day, heating up a fluid that can achieve high temperatures, aiming to produce useful energy as heat, electricity or fuels through different systems (LOVEGROVE; STEIN, 2012).

Figure 3.3 - CSP technologies: (a) parabolic trough, (b) linear Fresnel, (c) solar tower, (d) dish concentrators.



Source: Lovegrove and Stein (2012).

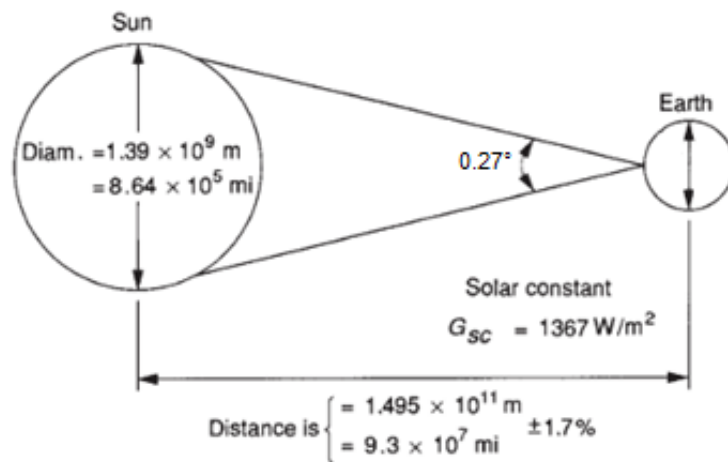
The longitudinal technologies are the parabolic troughs, which are composed by parabolic mirrors that reflects the radiation onto a tube where a fluid passes through; and linear Fresnel reflectors composed by small facets with independent tracking systems that when integrated composes a parable, with the facets reflecting the radiation onto a receiver similarly to the parabolic trough technology. In the case of such technologies, the temperatures achieved are smaller than punctual receivers, with the first ones are driven by one-axis tracking, whereas the latter ones are driven by a two-axis tracking system, therefore achieving higher temperatures (above

1,000°C). The punctual technologies are the solar tower, where assemblies of mirrors called heliostats reflects the DNI onto a receiver atop a tower, heating up a fluid; and dish concentrators, which also reflects the DNI with a two-axis tracking system onto a receiver, heating the working fluid (KALOGIROU, 2009; LOVEGROVE; STEIN, 2012).

3.2.1. The Sun

The sun is a sphere made of hot gases with an effective blackbody temperature of approximately 5,780 K. In relation to the sun, the earth's eccentricity (how much the orbit deviates from a perfect circle) is such that the distance between both varies by 1.7%. The considered astronomical unit, which is the distance between the earth and the sun, is 1.495×10^{11} m, where subtends an angle of 0.27° (4.7 mrad). The radiation emitted by the sun is almost fixed in terms of intensity, called solar constant (G_{sc}) (DUFFIE; BECKMAN; WOREK, 2013). Its value is $1,367 \text{ W/m}^2$, as shown in Figure 3.4 ahead.

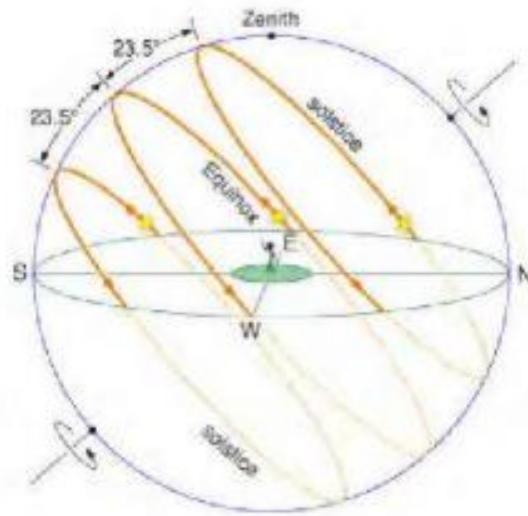
Figure 3.4 - Sun-earth relationships.



Source: Duffie, Beckman, and Worek (2013), adapted by the author.

These variations in the sun-earth distance does lead to variations in the incident flux of radiation, which can achieve up to 3.3% of flux variations according to Duffie, Beckman & Worek (2013). In addition, the extraterrestrial solar radiation varies throughout the year with seasons and variations in the earth's inclination (23.5°). Figure 3.5 ahead shows the summer (larger orange line) and winter (smaller orange line) solstices, as well as the equinox (intermediary orange line) sun's path over those particular days. As can be seen, the winter solstice has less sun hours over the day in comparison with the summer solstice, proportionally to the line's arc distance.

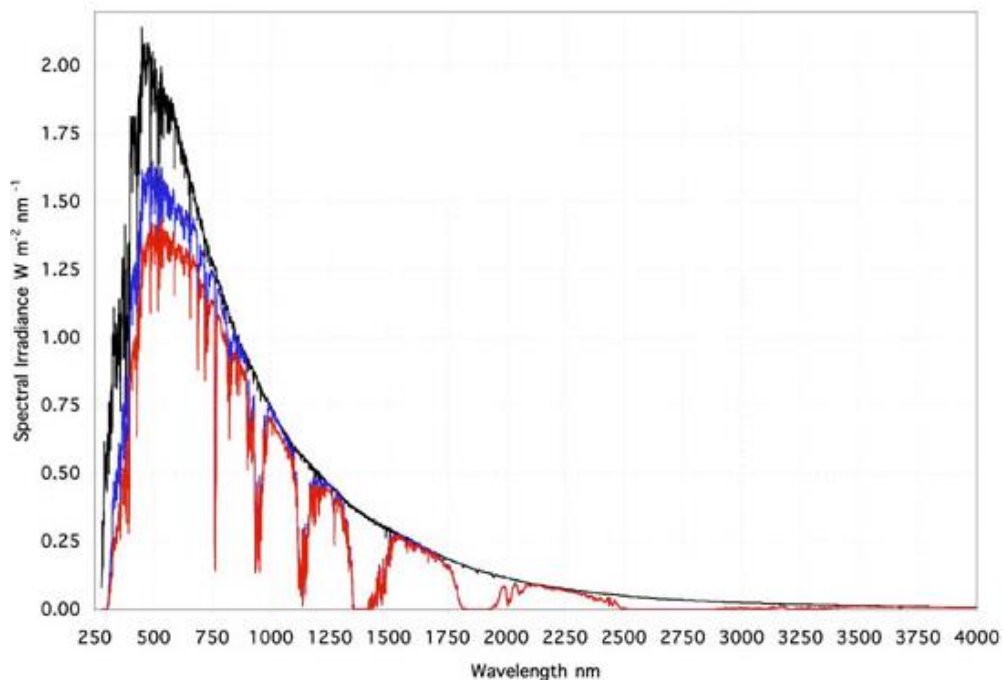
Figure 3.5 - Sun's movement over the day in different seasons.



Source: Prinsloo and Dobson (2015).

In addition, this solar radiation varies accordingly to the wavelength. So it is useful to know the radiation that would be received without atmosphere (AM 0, where AM stands for “air mass”), as well as the incoming radiation in the presence of atmosphere (also called AM 1.5). Figure 3.6 shows the extraterrestrial (black), global (blue) and direct normal spectral irradiance in a 37° sun-facing tilted surface provided by the American Society for Testing and Materials (ASTM) G-173 (NREL, 2019).

Figure 3.6 - ASTM G-173 extraterrestrial, global and direct normal spectral irradiance.



Source: NREL (2019).

3.2.2. Optical Concentration

CSP systems are composed by a receiver, a concentrator, and a tracking system. The receiver is the element in the system in where the DNI is absorbed and converted in another energy form, whereas the concentrator is the optical part of the system, i.e. the element that redirects the DNI onto the receiver. These concentrators can be cylindrical or surfaces of revolution, continuous or segmented, while the receivers can be convex, flat, or concave, and covered or uncovered (DUFFIE; BECKMAN; WOREK, 2013).

The concentration factor (C [-]), can be expressed as the ratio of the aperture area (A_a [m²]), which is the opening area where the solar radiation enters the concentrator, and the receiver area, or absorption area (A_A [m²]), as expressed in Eq. (3.1) (DUFFIE; BECKMAN; WOREK, 2013; HORTA, 2016). This definition is applied strictly to geometric concentrations (RABL, 1985).

$$C = \frac{A_a}{A_A} [-] \quad (3.1)$$

Nevertheless, when applied optical concentrations some constraints appear: the acceptance angle is reduced. The acceptance angle (θ_a [°]) is a measure of the hemispherical region from which the radiation that reaches the aperture is directed to the absorber surface, and decreases with an increasing concentration factor. This explains the need for a tracking system to follow the sun's path throughout the day and over the year (seasonality). For an ideal concentrator, the relation between concentration factor and acceptance half-angle (upper limit) can be expressed as follows for 2D, as in Eq. (3.2), and 3D, as in Eq. (3.3), concentrators with absorbers surrounded by vacuum (RABL, 1985; SEGAL, 2010):

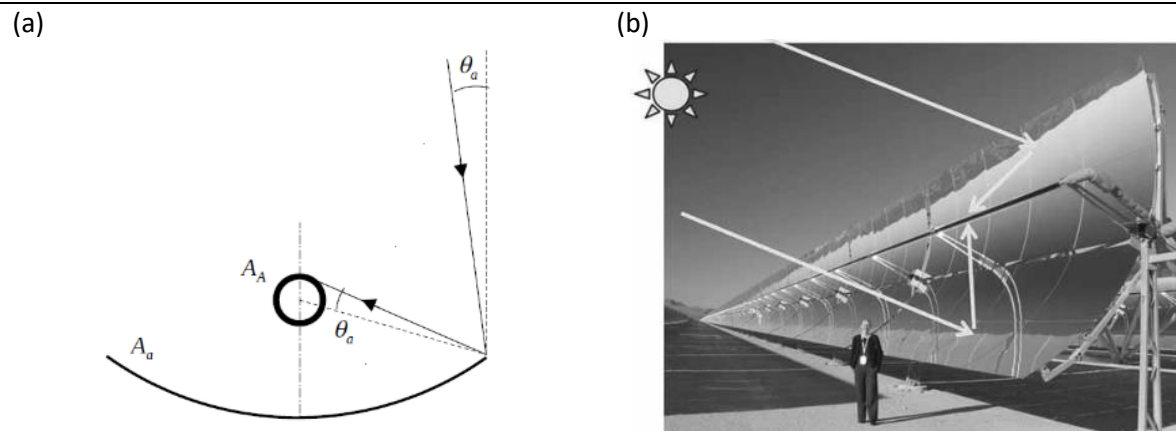
$$C_{2D} = \frac{A_a}{A_A} = \frac{1}{\sin(\theta_a)} [-] \quad (3.2)$$

$$C_{3D} = \frac{A_a}{A_A} = \frac{1}{\sin^2(\theta_a)} [-] \quad (3.3)$$

The angular radius of the sun (sun disk), as commented in Figure 3.4, is 0.27° (or 4.7 mrad), which means that a concentration limit of a 2D geometry system (line focus) is 213 suns, and a 3D geometry (point focus) is 45,300 suns (RABL, 1985).

Figure 3.7 (a) demonstrates schematically the relations between the acceptance half-angle, aperture and absorber areas, which can be longitudinal, as in is this example, as shown in parabolic trough in Figure 3.7 (b), or punctual (solar tower receiver and parabolic dish).

Figure 3.7 - (a) Acceptance half-angle, aperture and absorber areas relation, and (b) parabolic trough.



Source: (a) Horta (2016), (b) Lovegrove and Stein (2012).

The higher the temperature that must be reached by the system, the higher the concentration factor, and more precise must be the concentrators, i.e. optical system, and tracking system as well (DUFFIE; BECKMAN; WOREK, 2013).

3.3. Solar Tower Technology

As shown above, the solar tower systems consist of mirror assemblies (concentrators) with a two-axis tracking system, so called “heliostats”, that reflects the sun beam into a receiver atop a tower, which absorbs and transfers the heat to a fluid that can either go direct to the power cycle (direct cycle) or transfer heat to a working fluid of the power cycle (indirect cycle), or used as process heat (LOVEGROVE; STEIN, 2012; REINER et al., 2014).

The concentration factor of this technology is in the ranges from 500 up to 1,000 suns, and the commercial plants solar-to-electricity efficiency range from 15% to 18%, achieving 30% under design point conditions (REINER et al., 2014). One of the main advantages of the tower system is that the energy conversion happens in the receiver, avoiding the need of long pipes to transfer the fluid to the power block. However, since the receiver is fixed atop the tower, heliostats do not point directly at the sun, so the

amount of area which reflects the sun beam is reduced (cosine effect) when compared with the dish technology, where the receiver is not fixed, i.e. moves with the tracking dish (LOVEGROVE; STEIN, 2012).

The power block is similar to the conventional thermal power plants (e.g. coal or nuclear, most commonly using Rankine cycles and superheated steam), however with a smaller power level, where the power block is designed for the specific operation conditions of the solar configuration in question, and wet, dry or hybrid cooling methods are also applied (REINER et al., 2014).

Alongside the construction of SEGS in the Kramer Junction (USA), several test facilities and pilot plants were build and operate between the 80's and 90's. Most of them applied the "north field" designs using flat panels or small cavity receivers, due to their small scale, apart from Solar One and Solar Two, which were above 10 MW_{el}, applying a surrounding field and a cylindrical receiver (LOVEGROVE; STEIN, 2012). Table 3.1 summarizes these pilot projects.

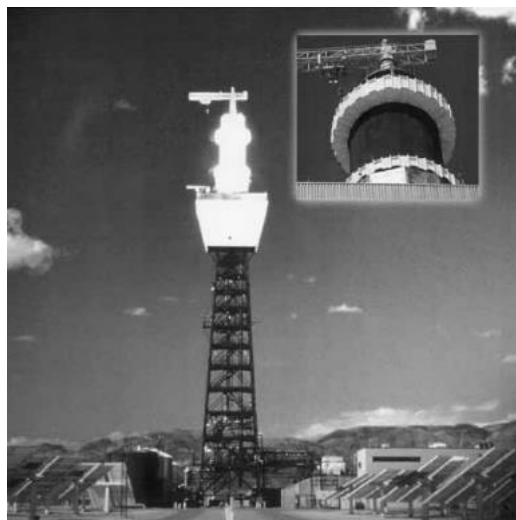
Table 3.1 – First central receiver demonstration projects.

	Eurelios (Italy)	IEA- CRS (Spain)	CESA-1 (Spain)	Weizmann (Israel)	Solar One (USA)	Solar Two (USA)
Net Turbine	1 MW _{el}	1 MW _{el}	1.2 MW _{el}	0.5 MW _{el}	10 MW _{el}	10 MW _{el}
Thermal Power	-	7.7 MW _{th}	7.7 MW _{th}	-	43.4 MW _{th}	56 MW _{th}
Mirror Area	6,260 m ²	12,912 m ²	11,880 m ²	3,500 m ²	71,095 m ²	81,344 m ²
Target Height	55 m	43 m	60 m	80 m		
Heat Transfer Fluid	Water/Steam	Sodium	Water/Steam	Beam down air	Water/Steam	Molten Salt
Receiver Type	Cavity	Cavity	Cavity	CPC + Cavity	External Cylinder	External Cylinder
Period of Service	1980-81	1981-85	1983-84	2001-	1982-88	1996-99

Source: adapted from Lovegrove and Stein (2012).

Over the projects presented above, Solar One, later re-configured and re-launched as Solar Two, deserves a special attention, since they were the first system worldwide configured as a pre-commercial pilot plant. Solar One used an external cylinder superheated steam receiver, with allowable flux of only 300 kW/m², hence a large receiver (13.7 m high and 7 m diameter for the maximum energy), and a single rocks-sand and oil-thermo-cline storage for 4 hours of operation. The thermal gradients with stresses limited the allowable flux density on the receiver, and in addition, rapid changes in the receiver power due to intermittency made control difficult, with the turbine subjected to rapid changes. Thus, the heliostat field, tower and turbine were reconfigured in Solar Two (Figure 3.8), with molten salts being applied as HTF. The low pressure of those salts in comparison to steam made possible to use much thinner walled tubes in the receiver, reducing thermal stresses, added to better heat transfer characteristics, increasing the allowable flux up to 1MW/m², and a use of a smaller receiver than the used in Solar One. However, several problems made the plant to be shut down in 1999 just after it had been completed, before significant commercial operation (LOVEGROVE; STEIN, 2012).

Figure 3.8 - Solar Two power plant with an external cylinder receiver.



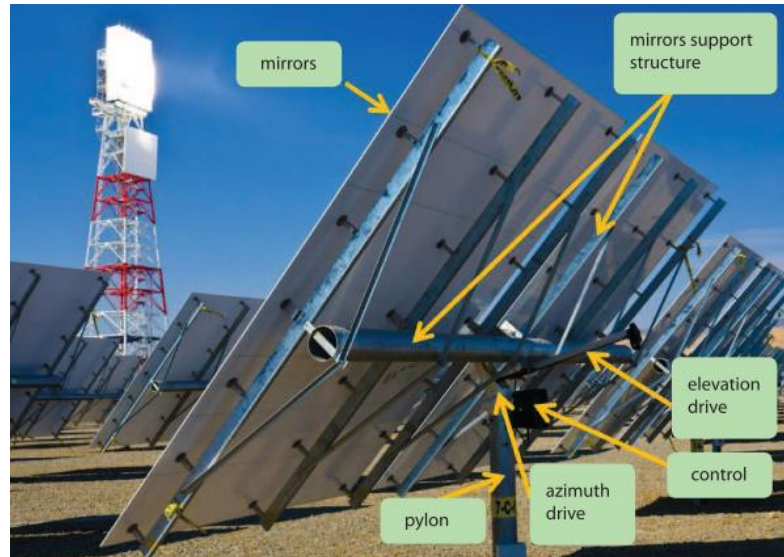
Source: Lovegrove and Stein (2012).

3.3.1. The Heliostats

The role of a heliostat in a field is to track the Sun, thus they must be precise enough to do their job accurately (beam reflection error of less than 3 mrad) while sustaining gravity and wind loads, even when they are located far from the tower (e.g.

1 km far). The most common setting, the so-called “T-type” heliostat (Figure 3.9), is composed by the mirrors and a structure that sustains it, the elevation and azimuth drives, the control system, and the pylon mounted on the foundation.

Figure 3.9 – “T-type” heliostat configuration.



Source: Reiner et al. (2014)

The heliostat field is the central cost component within a solar tower plant, since it can achieve 50% of the total costs (KOLB et al., 2007). Thus, designs that can both reduce the costs and increase performance are the main goal for engineers. Over the years, several different designs of heliostats have been made trying to achieve such goal, with different structures and sizes.

Figure 3.10 – (a) Sener’s 178m² heliostat and (b) eSolar’s 2m² tripod heliostat.

(a)



(b)



Source: Pfahl et al. (2017).

Currently, the conventional heliostats concepts (“T-type” heliostats, like Sener’s heliostat) can hardly reduce costs (PFAHL et al., 2013). In this concept, the German Aerospace Center (DLR) developed the light-weight rim drive heliostats (Figure 3.11), which has several advantages regarding wind loads, reflectivity, low cost drive demand (the drives, especially the azimuth drive, can achieve 35% of the solar field costs (REINER et al., 2014)), the foundation, among others (PFAHL et al., 2013).

Figure 3.11 – DLR’s 9m² rim drive heliostat.



Source: Pfahl et al. (2017).

3.3.2. The Receiver

The receivers absorb the solar radiation, converting it into useful heat transferred to a working medium. Since they are exposed to high solar flux added to high temperatures and their consequent losses, their requirements are high, demanding an efficient conversion of heat, inhomogeneous heat flux acceptance, and long-term operation with an acceptable cost (REINER et al., 2014). Their main configurations and characteristics are discussed in detail in [Chapter 3.5](#), ahead.

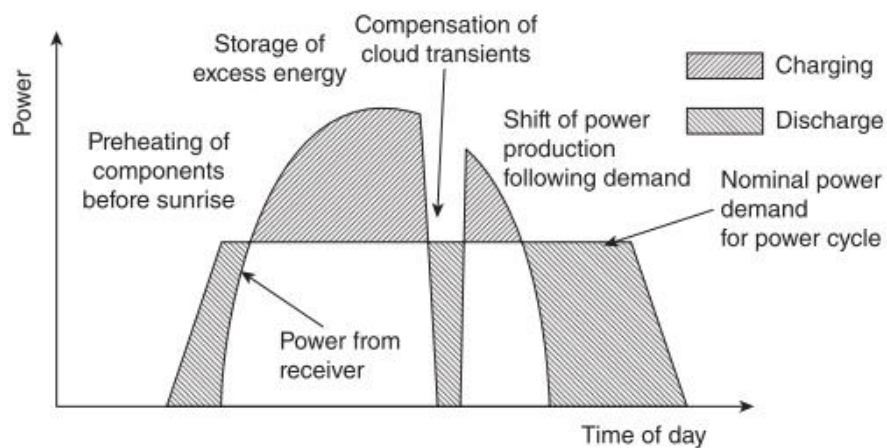
3.3.3. Storage and Hybridization

As said before, CSP can provide a flexibility and reliability to the grid, since it can both store thermal energy as well as be integrated in conventional power plants such as coal or biomass plants, or hybridized with natural gas or biomass. This is a key advantage of CSP in comparison with other technologies such as photovoltaic or wind, where batteries are a complex and independent system with extra investment

needed. On CSP, the thermal energy storage (TES) can be integrated in a cost-effective way where its benefits can be reached with a small or null impact in the overall efficiency of the system as well as in the cost of energy (LOVEGROVE; STEIN, 2012).

The Figure 3.12 ahead presents how the shifting on electricity generation throughout the day. This is crucial for a grid reliability since electricity can be generated in periods of high demand, as well as improved efficiency due to generation in periods of clouds, reduced external backup demand that usually are met by fossil fuels, and reduce startup periods with heat coming from the storage system (LOVEGROVE; STEIN, 2012).

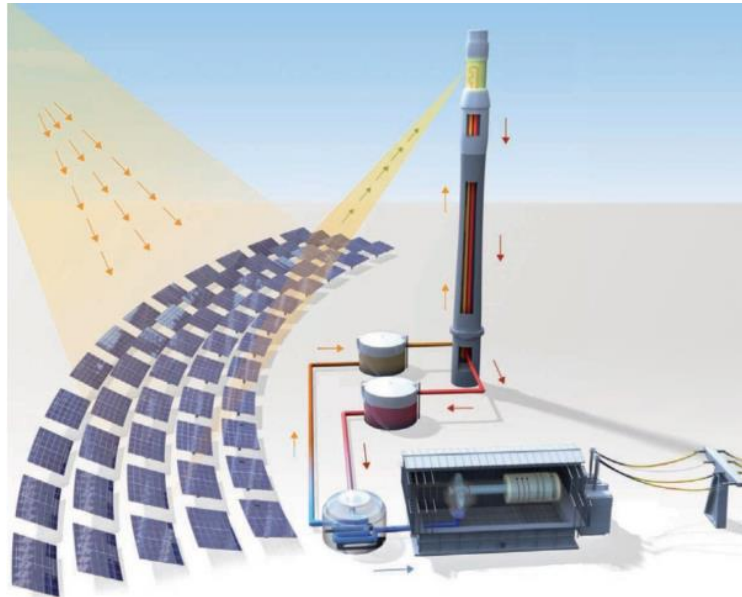
Figure 3.12 – Thermal storage flexibility in a CSP system over a day.



Source: Lovegrove and Stein (2012).

The functionality of a thermal storage system is quite simple, as shown in Figure 3.13 below, which represents the Gemasolar solar tower configuration with molten salt (eutectic mixture of 60% of NaNO_3 and 40% KNO_3) as HTF, the most common configuration with thermal storage used nowadays. In this case, the HTF is heated in the receiver atop the tower, going directly to the hot tank (red arrows), then goes to the heat exchanger generating steam, passes through the cold tank and goes up to the receiver (orange arrows), closing the so called “solar loop”. In this case, when molten salt is used, is crucial to pay attention to the temperature in the tanks, since molten salt freezes under 290°C , and cracks over 590°C , which are the range of operation temperatures in this solar field (SCHLIPF; STENGLEIN; SCHNEIDER, 2014; REN21, 2018).

Figure 3.13 – Gemasolar tower system configuration with two TES molten salt tanks.



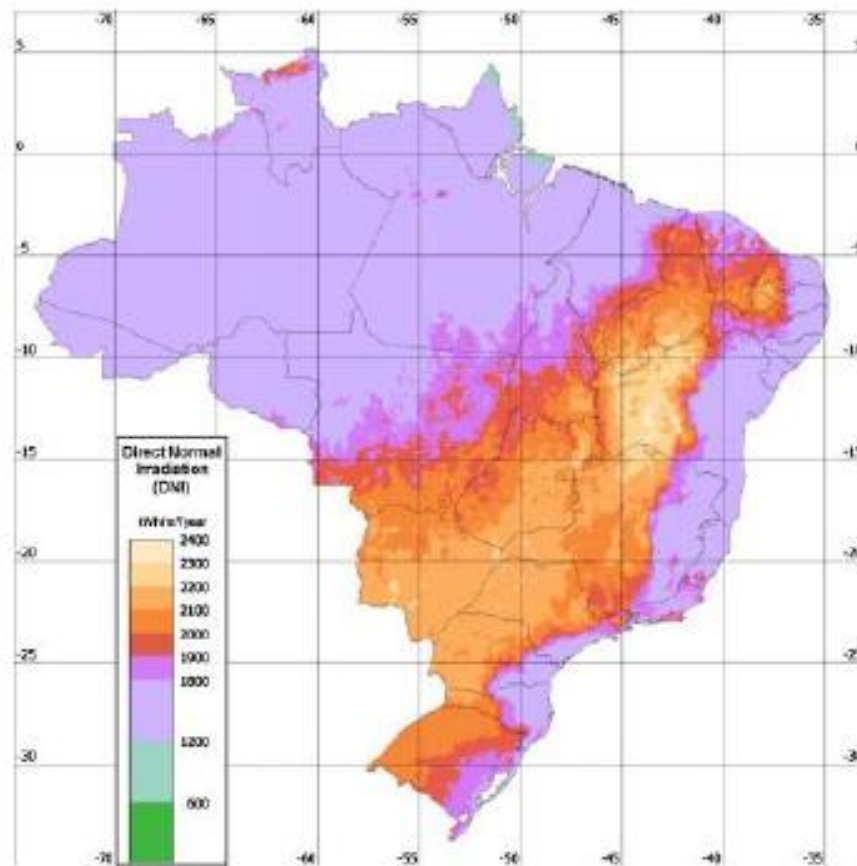
Source: Schlipf, Stenglein, and Schneider (2014).

Even though CSP inception dates from the 80's, the deployment is still in its infancy. In the end of 2017, the installed capacity was 5.5 GW, mostly located in Spain and USA (MEHOS, 2019). However, several projects are under construction over the world, especially in China, where the CSP industry is gaining momentum, and in the Middle East and North Africa (MENA) region, in places with high DNI levels like Morocco. Another aspect that must be commented is that among the projects under construction, the vast majority will incorporate TES in their configuration, providing dispatchable or baseload power (REN21, 2018).

3.4. CSP in Brazil

Brazil has a vast territory with great DNI levels, which are the main resource regarding the CSP technology. Figure 3.14 below demonstrates the incidence of DNI over the Brazilian territory, where a large portion of it has incidences over 2,000 kWh/m².year, which are indicated for CSP implementations.

Figure 3.14 – DNI assessed by satellite – SWERA project.



Source: Viana et al. (2010).

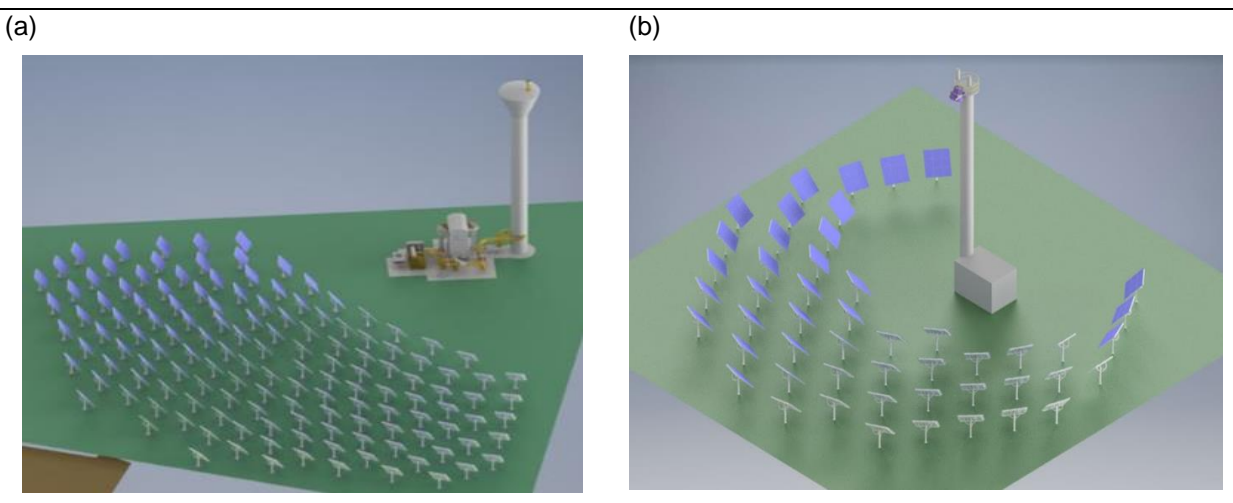
To provide a background, several studies regarding the CSP implementation have been made over the past years, from a general overview (LODI, 2011), to financial (PARENTE, 2015), hybridization (SORIA; SCHAEFFER; SZKLO, 2014; LANGER, 2016), storage (CASTRO, 2015), environmental guide (GARCIA; RAMOS; CASTRO, 2017), meteorological data assessments (VIANA et al., 2011; TIBA et al., 2014), transient analysis (CORGOZINHO; HENRIQUE; NETO, 2014), trigeneration (MALAGUETA; SZKLO; DUTRA, 2014), among others. Even though several studies were conducted, currently there are no operational CSP plants in Brazil. Nevertheless, Research and Development (R&D) projects are under development and construction, such as the SMILE Project, explained ahead.

3.4.1. The SMILE Project

The SMILE Project is a partnership between the University of São Paulo (USP), the company Solinova, the Brazilian National Bank (BNDES), the Elektro utility, and the German Aerospace Center (DLR). In this project, two solar tower plants with 70

kW_{el} and $50 kW_{el}$ will be constructed, one in Pirassununga, São Paulo ($21^{\circ}57' S$, $47^{\circ}26' W$), in the USP *campus*, which will provide power to the university internal grid, exporting to the utility grid if surpluses occur, and heat to a slaughterhouse next by; and another in Caiçara do Rio do Vento, Rio Grande do Norte ($5^{\circ}42' S$, $36^{\circ}4' W$), providing electricity to the utility grid and heat to a dairy (GREEN, 2018). The Figure 3.15 ahead demonstrates the cogeneration plants' configurations.

Figure 3.15 – The SMILE project configurations: (a) $100 kW_{el}$ Pirassununga and (b) $50 kW_{el}$ Caiçara do Rio do Vento.

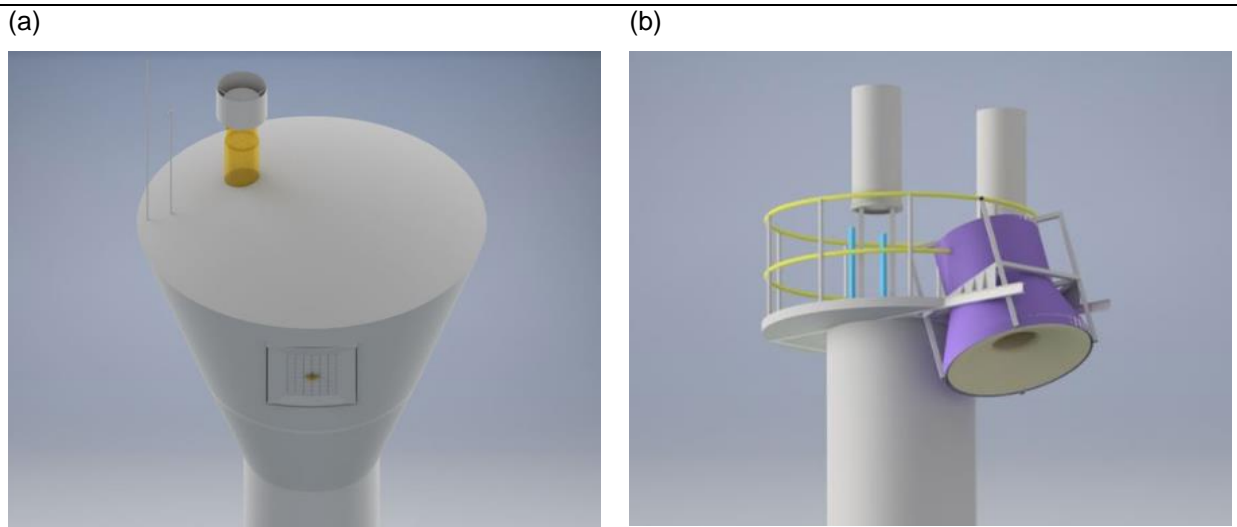


Source: GREEN (2018).

In Pirassununga's case, the heliostats reflect the DNI onto an external receiver located atop a tower, heating up air, which works as HTF, transferring heat to an organic fluid through a heat exchanger, closing the solar loop. Subsequently, the organic fluid expands on a microturbine, generates electricity, goes to a regenerator and a condenser, where transfers heat to water for the slaughterhouse, closing the Organic Rankine Cycle (ORC) loop. The solar loop will have a backup boiler moved by biodiesel produced in the University.

In the Caiçara do Rio do Vento case, however, the heat provided by the solar field heats up the water that passes through a cavity receiver, generating steam in a so-called Direct Steam Generation. Figure 3.16 shows the different receivers used in the project.

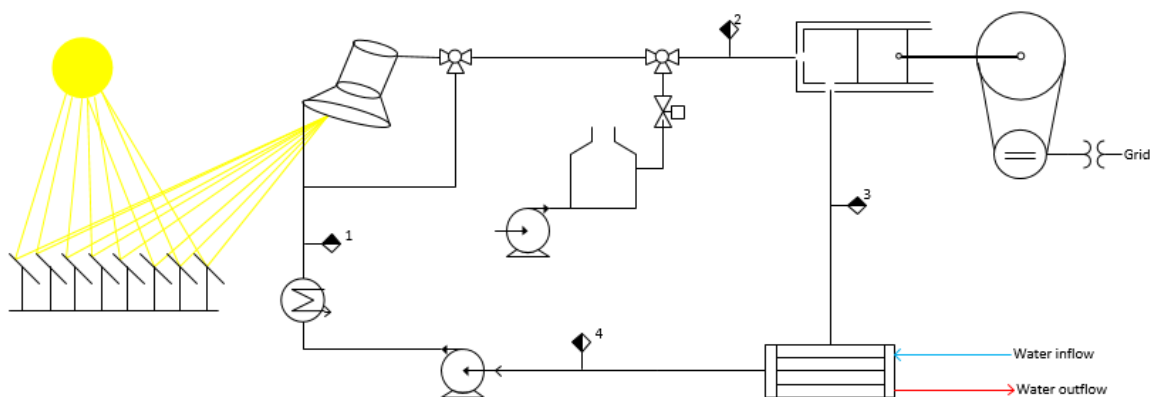
Figure 3.16 – Solar receivers: (a) external receiver (Pirassununga’s configuration) and (b) cavity receiver (Caiçara do Rio do Vento’s configuration).



Source: GREEN (2018).

Figure 3.17 shows the schematic diagram of the Caiçara cogeneration system. Here, after the pump in (1), water enters the receiver at 45 °C and 1.4 MPa (14 bar), and is heated up to produce superheated steam. The receiver generates superheated steam at 225 °C in the outlet (2). The backup is present to guarantee that superheated steam enters in the steam engine in 225 °C, exiting in (3) at 100 kPa (1 bar) and approximately 100 °C. After cooling down by losing heat to warm up the dairy water and preheat the water that will go to the receiver, the saturated water in (4) is at 100 kPa (1 bar), 45 °C, closing the loop.

Figure 3.17 – Caiçara do Rio do Vento schematic diagram.



Source: The author.

Table 3.2 summarizes the temperature, pressure and specific enthalpy and entropy of the operational points presented above.

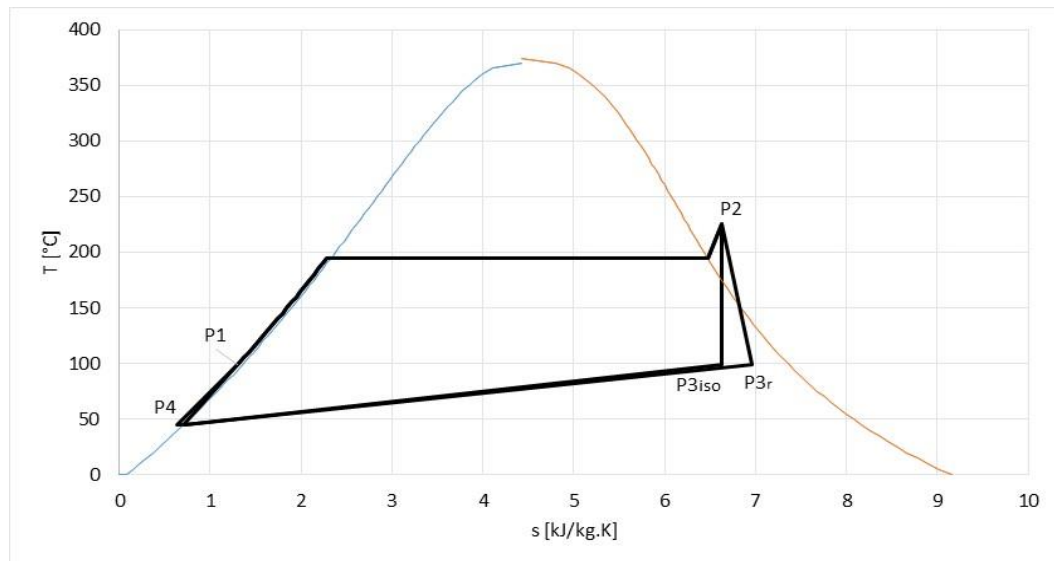
Table 3.2 – Temperature, pressure, specific enthalpy and entropy of the operational points.

Operational Point	Temperature	Pressure	Specific Enthalpy [kJ/kg]	Specific Entropy [kJ/kg.K]
Point 1	45 °C	1.4 MPa	189.476	0.638
Point 2	225 °C	1.4 MPa	2867.95	6.631
Point 3 isentropic	99.60 °C	100 kPa	2400.34	6.631
Point 3 Real	99.60 °C	100 kPa	2587.38	6.965
Point 4	45 °C	100 kPa	188.51	0.638

Source: The author.

The points presented in Figure 3.17 and Table 3.2 are also shown in the “T x s” diagram presented ahead in Figure 3.18.

Figure 3.18 – “T x s” diagram with operational points.

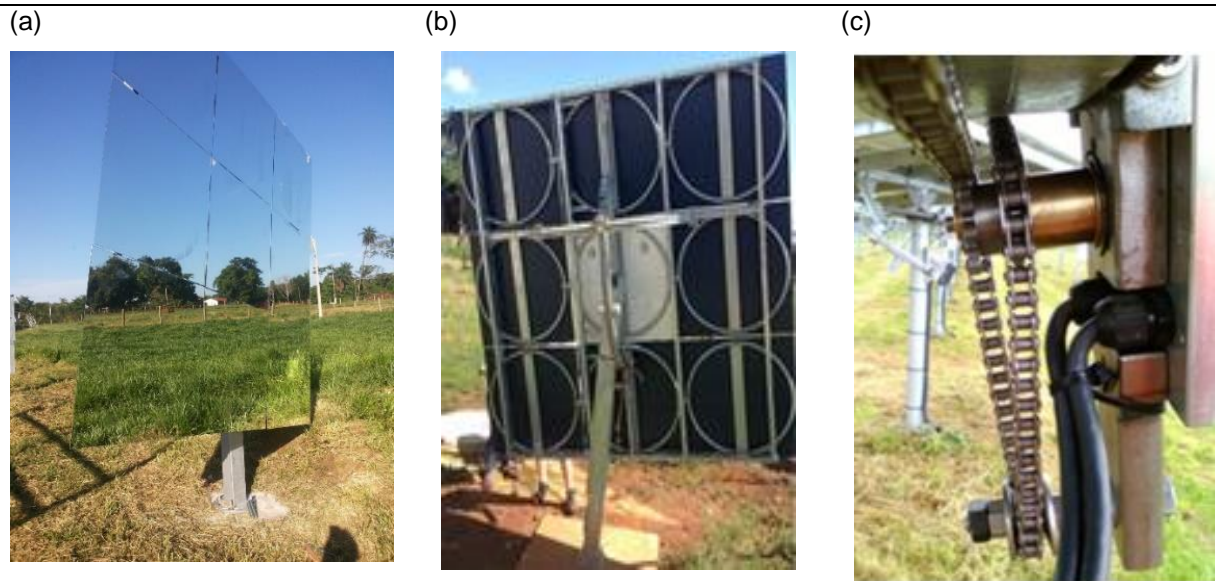


Source: The author.

3.4.1.1. The heliostats

The SMILE Project will use rim drive heliostats developed by DLR. They are composed by 9 x 1 m² facts with 5 mm glass mirrors (95% reflectivity) (Figure 3.19 (a)), which are glued in steel rings (Figure 3.19 (b)), and a pylon of 2.3 m height (optical height). The system uses a low cost chain gears with sprockets (Figure 3.19 (c)) to reduce costs without losing accuracy (LIEDKE et al., 2016).

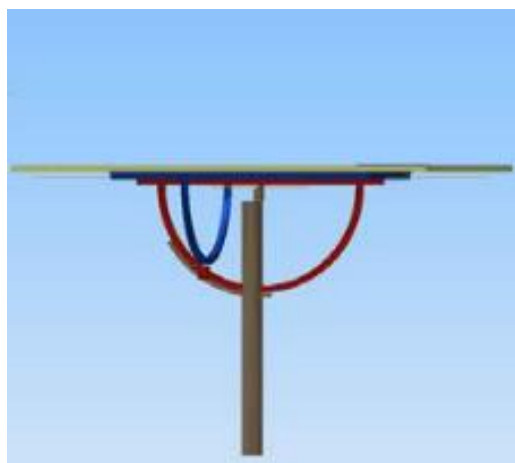
Figure 3.19 – Rim drive heliostat: (a) front and (b) back views, and (c) driving chain gear.



Source: GREEN (2018).

The heliostat has a horizontal fixed primary axis, where the red rim in Figure 3.20 moves itself; and vertical secondary axis not fixed, with the blue rim mounted in the mirror assembly. The drive for the primary axis is mounted in the pylon, while the drive for the secondary axis is mounted in the red rim. The last configuration of the rim heliostat, improved in Brazil, has an inclination of 11° in the second rim as a structure improvement (primary axis no longer passes through the pylon), as shown in Figure 3.19 (b) above.

Figure 3.20 – Rim drive heliostat with primary and secondary axis.



Source: Pfahl et al. (2013).

3.4.1.2. The Solar Receiver

The SMILE project will use a derivative design of the Australian National University (ANU) SG4 solar receiver (Figure 3.21). Firstly, the SG4 was designed for a dish concentrator (500 m² SG4 Big Dish, as shown in Figure 3.3 (d)). *A priori*, the ANU assessed the design, which could not fulfill the SMILE operational requirements (pressure, steam velocity and temperature). Thus, must be applied a modified design.

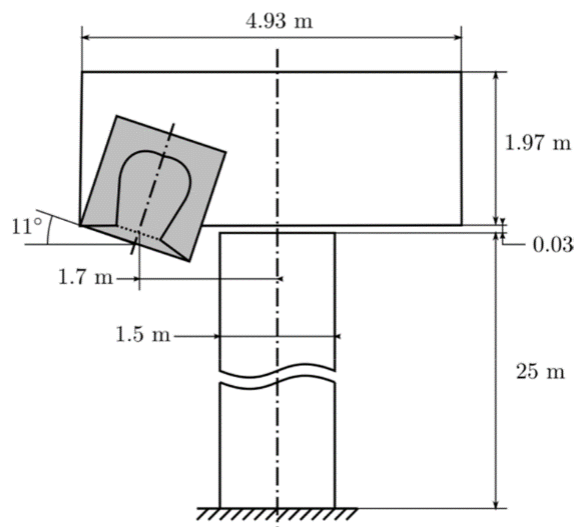
Figure 3.21 – ANU’s SG4 original solar receiver.



Source: Pye et al. (2017).

The receiver, placed atop a tower with 11° of inclination (Figure 3.22), has loops of coils made of Stainless Steel 316, divided in three different sections with different diameters each (i.e. the “wind skirt”, the cavity middle part, and the cavity dome).

Figure 3.22 – Simplified demonstration of the receiver’s inclination of 11°.



Source: ANU (2017).

3.4.1.3. The power cycle and hybridization

In a Rankine cycle, there are four conventional expanders: turbine, screw or scroll machine, and a reciprocating piston engine. Steam turbines are not commonly applied in micro-scale Rankine cycles, mainly due to their complexity and costs, often with capacities for bigger power plants, not being economically used in micro-scale power plants (QIU; LIU; RIFFAT, 2011).

Instead of steam turbines, turbine expander are usually used. Nevertheless, in small-scale systems, reciprocating steam engines started to gain attention for power generation due to their simplified engine architecture, as well as for the valve distribution system (DELLICOMPAGNI et al., 2018).

In the Caiçara project, due mainly to costs constraints, a reciprocating piston engine with 50 kW_{el} is being considered and studied as an expansion option to generated electricity for the dairy, and in times with no consumption or surplus of electricity generation, export to the grid.

To support periods of high demand or intermittence, as well as for night periods with schedule demand, the system will comprise an auxiliary boiler running with eucalyptus pallets.

3.4.1.4. The cogeneration process

Since the SMILE process involves both electricity and heat generation for agro-industrial processes, and in Caiçara's case, a dairy, it's necessary to understand the unit processes for milk production in a dairy, gathering information about the electrical and heat demands in conventional dairies.

The dairy industry encompasses several operations and activities that may differ as a function of the final products. However, there are operations that are fundamental and common for any kind of final product, like the reception of milk and ingredients, the processing (which involves pasteurization, for example), the thermal treatment, the storage, and the final products expedition. Over those operations, unit processes such as pasteurization and sterilization, refrigeration and storage demands some kind of energy (MAGANHA, 2006; SHARMA et al., 2017). Table 3.3 summarizes the most frequent use of energy in conventional dairies.

Table 3.3 – Most frequent use of energy and equipment in dairies.

Energy	Use	Equipment
Thermal	Water and steam generation, cleaning	Pasteurizers/sterilizers, cleaning systems (CIP)
Electric	Refrigeration, lighting, ventilation, equipment operation	Electrical equipment (e.g. pumps, mixers), fans, compressed air

Source: The author, adapted from Maganha (2006).

Accordingly to Maganha (2006), it is estimated that 80% of the total energy consumption is thermal, and the remaining 20% are electric. Nevertheless, the energy consumption varies regarding the final product as well as from the factory equipment conditions, automation degree, used technology, energy efficiency measures, among others, as presented in Table 3.4.

Table 3.4 – Total energy consumption for different types of factories.

Type of Factory	Total energy consumption [kWh/liter of processed milk]	
Modern with high efficiency pasteurizer and new boiler	0.09	ND
Modern with hot water for process	0.13	ND
Old using steam	0.27	ND
Average of the majority of factories	0.14 up to 0.33	0.05 up to 0.21

Source: The author, adapted from Maganha (2006).

Therefore, to precisely assess the energy demand, one must determine the final product aimed, equipment used, and unit processes applied to produce it. In Caiçara's case, it is assumed that the dairy will produce only milk through pasteurization. Maganha (2006) summarizes the main thermal processes in a dairy, accordingly to the final product. For pasteurized milk, the thermal processes can be:

Table 3.5 – Main thermal processes for pasteurized milk.

Type	Temperature Range [°C]	Duration	Process Observation
Thermalization	57 – 68	1 minute and 15 seconds	Used in raw milk to stabilize its qualities for long storage periods
Slow or Low Pasteurization	62 – 65	30 minutes	
Quick Pasteurization	71 – 75	15 – 45 seconds	Relatively mild treatment, and more used among all
High Pasteurization	85 - 92	8 – 15 seconds	Used mainly for milk cream

Source: The author, adapted from Maganha (2006).

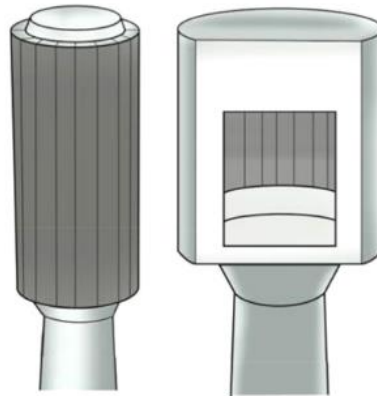
3.5. Central Solar Receivers

Central solar receivers are an object of study for Research and Development (R&D) since the 70's. In comparison to the other linear-focus CSP technologies such as parabolic troughs, they are able to achieve higher concentration ratios, higher temperatures, hence, higher efficiencies. Throughout the years, central receivers used different media regarding the heat transfer fluid, as well as heat storage medium liquid media, such as water or molten salts; gas media, such as air; and solid media, such as ceramic particles, where different receivers are applied accordingly to the media used (HO, 2017).

A standard solar receiver does not exist. However, traditionally, solar receivers are classified as external receivers or cavity receivers, both of them tubular receivers. In the first case, individual panels are assembled vertically in a cylinder that is located atop a tower, and in the latter, the configuration is almost the same. The main differences is that in the first case, the tubes are exposed to ambient conditions such as wind loads, hail and ambient temperatures, increasing radiation and convective losses for example; whereas in the second case the receiver has some protection from the ambient conditions, since it is located inside an open cavity, reducing the mentioned losses, where higher efficiencies (more than 10%) can be achieved. For liquid media, those two configurations are commonly used, where the panels of tubes

are heated up by the incident irradiation, and cooled by the fluid flowing (WAGNER, 2008; THIRUMALAI et al., 2014; HO, 2017).

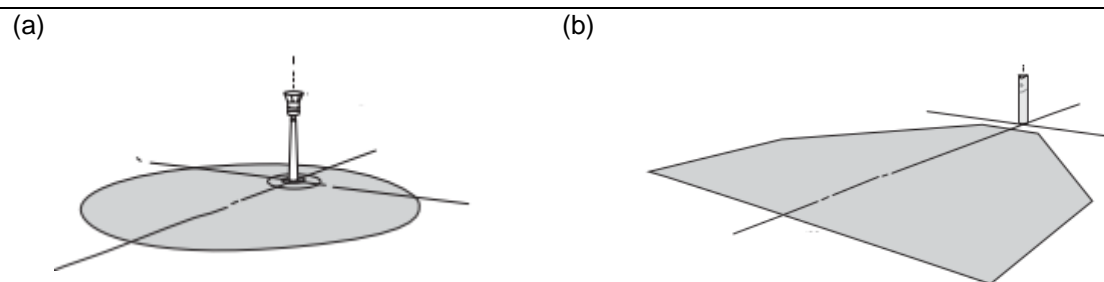
Figure 3.23 - External (left) and cavity (right) receivers.



Source: Ho and Iverson (2014).

External receivers are typically applied in surrounding fields, whereas cavity receivers are more commonly used in northern or southern fields. Another feature of cavity receivers in comparison with external receivers is that the first ones require taller towers to comprise all the heliostats for a given power requirement (LOVEGROVE; STEIN, 2012; HO, 2017). Figure 3.24 (a) shows a surrounding field configuration, whereas Figure 3.24 (b) shows a polar field configuration, both proposed for the Solar One facility.

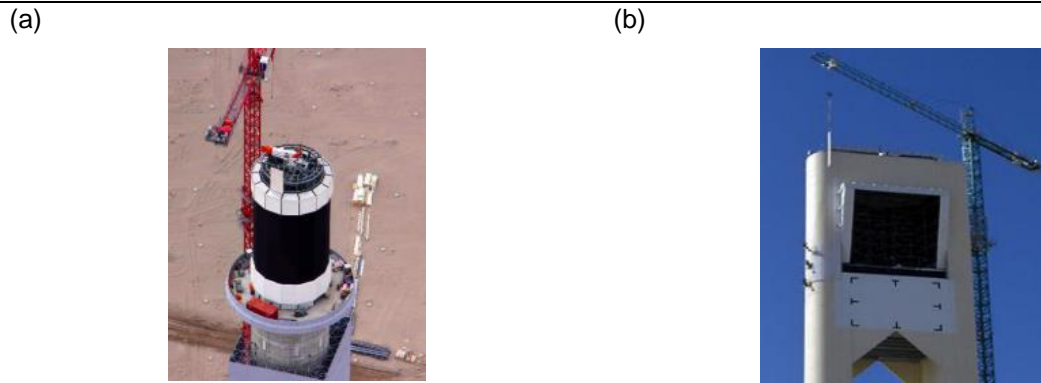
Figure 3.24 – (a) Surrounding field and (b) polar field configurations.



Source: Lovegrove and Stein (2012).

Up to 2015, those two configurations were the majority in solar tower power plants. Cavity receivers were used in CSP power plants like Sierra Sun Tower in USA, PS 10 and 20 and Solugas in Spain, and Dahan Power Plant in China, and external receivers were used in power plants like Gemasolar in Spain, Crescent Dunes and Ivanpah in USA (BEHAR; KHELLAF; MOHAMMEDI, 2013; THIRUMALAI et al., 2014).

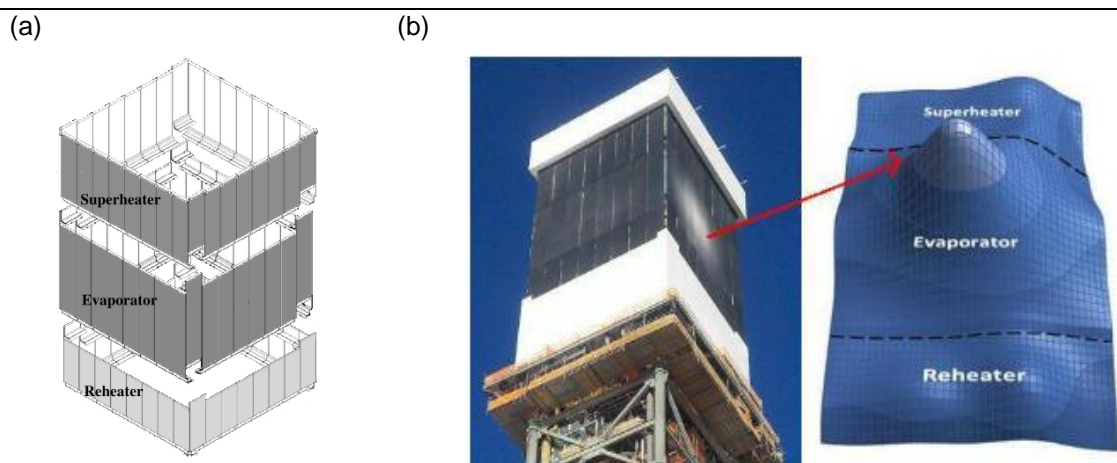
Figure 3.25 - (a) External cylindrical receiver used in Crescent Dunes (USA) and (b) cavity receiver used in PS10 (Spain).



Source: Thirumalai et al. (2014).

A good example of external rectangular receiver for superheated DSG is the concept applied in the “Ivanpah Solar Electric Generating System” facility, consisting in three 126 MW_{el} unities, where in order to generate steam through solar energy, the solar receivers are divided in three distinct heating surfaces: a reheater, an evaporator, and a superheater. The receiver is located atop a tower 122 m height, designed to produce 106.5 kg/s of superheated steam at 545 °C and 165 bar, as well as 104.7 kg/s of reheat steam at 485 °C and 41 bar. Figure 3.26 (a) demonstrates the three mentioned parts, and Figure 3.26 (b) shows the heat input distribution over the three surfaces (PLOTKIN et al., 2011).

Figure 3.26 - (a) Reheater, Evaporator and Superheater physical locations; (b) Receiver heat input distribution over the surfaces.



Source: (a) Plotkin et al. (2016); (b) Thirumalai et al. (2014).

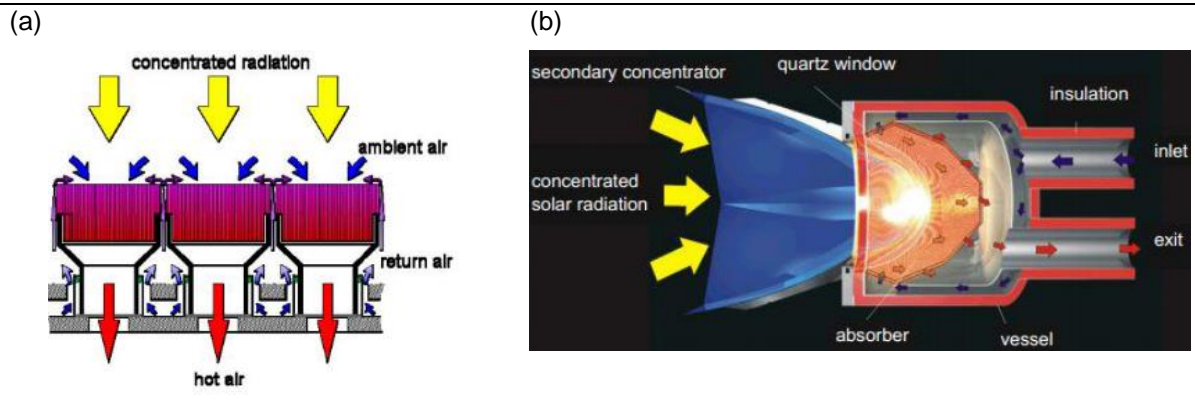
However, to increase efficiency of power cycles, higher temperatures than currently achieved by operational power-tower plants, where the gross thermal-to-electric efficiency typically ranges from 30% to 40% at turbine inlets lower than 600 °C, must be reached. These cycles include combine air Brayton, supercritical-CO₂ (sCO₂), and ultra-supercritical steam cycles. Nevertheless, in such cycles molten salts, the most common HTF currently, cannot be applied, since it becomes chemically unstable above 600 °C, producing corrosive oxide ions and resulting in significant mass loss (BLANCO; SANTIGOSA, 2017; HO, 2017).

Gas receivers present themselves as an opportunity, by using tubes or volumetric honeycombs and channels to heat most commonly air to high temperatures (HO, 2017). The associated advantages of air receivers are several, like the availability and non-toxicity of the fluid, no trace heating necessary, achieving higher thermodynamic efficiencies, where receiver thermal efficiencies may be larger than 75%, since the volumetric effect reduces radiation losses (ÁVILA-MARÍN, 2011). However, some challenges are included, like the low thermal conductivity and heat capacitance, generation of flow instabilities, and potential for expensive equipment and materials if extra heat exchangers or high pressure piping is needed (HO, 2017).

The volumetric receivers are characterized as open volumetric and closed or pressurized volumetric. In the first case, ambient air is pulled into the porous media, heating up by the concentrated solar irradiation, and the ambient air outside cools the surface, avoiding damages to the material. The tower power plant owned by DLR in Jülich applies an open volumetric receiver, where ceramic absorber modules absorb the solar radiation up to 1,000 °C, heating the air up to 680 °C at ambient pressure, generating steam in a heat exchanger (HOFFSCHMIDT, 2014; DLR, 2019).

Figure 3.27 (a) presents the concept of a volumetric receiver such as the used in Jülich, whereas Figure 3.27 (b) shows the closed or pressurized volumetric receiver. In the latter, the HTF is blown to the dome-shaped quartz glass window. This receiver is used in order to heat up air as HTF in a high pressure module of a gas turbine in a Brayton cycle (THIRUMALAI et al., 2014; DLR, 2019).

Figure 3.27 - (a) Open volumetric and (b) pressurized volumetric receiver.



Source: Thirumalai et al. (2014).

Solid-based receivers are still incipient. A first-of-kind power plant is operational in Australia, where eight solar storage receivers composed of graphite blocks are located atop a tower, with a facing down aperture that is irradiated by surrounding heliostats. The graphite blocks produce steam from 200 °C to 500 °C, powering a 3 MW_{el} turbine in a Rankine cycle. Figure 3.28 shows the central receiver system. Particle receivers have been studied extensively, but no commercial applications are deployed yet (HO, 2017).

Figure 3.28 - Solid-based graphite central receiver in Australia.



Source: Ho (2017).

Nonetheless, several emerging technologies for central receivers are being extensively studied, like particle-based receivers. In this case, particles can achieve high temperatures of more than 1,000 °C without decomposition or corrosion like molten salts, and work in temperatures below 200 °C without freezing, which occur with molten salts. Different direct heating methods have been studied, such as free-

falling particles, centrifugal, obstructed and fluidized, as well as indirect methods, like gravity-driven flow through tubes and fluidized particle flow in tubes (HO, 2017).

3.5.1. The Cavity Receiver

Cavity receivers have been widely used in solar tower plants for many years. In this conception, the radiation coming from the mirrors enters the aperture to a box-like structure before reaching the heat transfer surface (tubes), therefore reducing convection and radiation losses when compared to external receivers, resulting in higher efficiencies.

Cavities have positive characteristic in which the radiation that enters the receiver aperture can be spread over the absorbing surface to reduce the problems of excessive flux density, which results in a significant amount of diffuse solar beams leaping inside the cavity, with some of them finding the aperture and being effectively reflected. Another effect is that a large part of the cavity absorbs and reradiates the radiation at temperatures above of the surface that is transferring heat, where a portion of this infrared also finds the aperture. Lastly, the cavity is in contact with enclosed air, heating it to high temperatures, which instigates turbulent convective circulations, which can carry heat out of the aperture, feature strongly stimulated by ambient air, which can play the major role in a cavity receiver performance. Therefore, as a contrast and a consequence, a bad designed cavity receiver can experience greater losses than billboard or external receivers (LOVEGROVE; STEIN, 2012; SAMANES; GARCÍA-BARBERENA; ZAVERSKY, 2015).

Throughout the years, several different studies were carried focusing on cavity receivers, ranging from different geometries and inclinations to thermal losses with different heat transfer fluids. This is quite important, since poorly designed cavities could increase losses instead of reducing them. Ahead, a survey shows several studies about cavity receivers. It is possible to notice that convective heat transfer mechanism, mainly due to its complexity, is highlighted in several studies, as well as its relation with the air temperature inside the cavity, the inclination and geometry, and the wind conditions.

Regarding receiver geometries, Harris & Lenz (1985) carried an investigation with five different cavity receiver geometries (cylindrical, hetero-conical, spherical, elliptical and conical), where varying the concentrator rim angle and geometry can

strongly affect the cavity power profile, but with little effect on overall system efficiency. Paitoonsurikarn & Lovegrove (2006) also conducted a numerical simulation with three different cavity geometries, establishing a Nusselt Number correlation for natural convection.

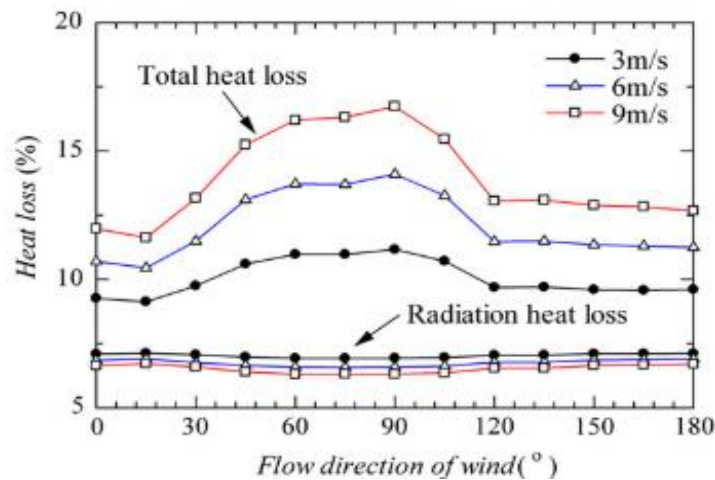
Different studies were also well conducted regarding thermal losses. Clausing (1981) presented an analytical model to estimate convective losses from cavity receivers, and used evidence of experiments to test the hypothesis. The results indicated that convective losses in the receivers are considerable, and that the wind influence over the convective losses in operational conditions are minimal. Another work conducted by Clausing (1983) compares analytical predictions of convective losses, and experimental results, since the amount of hot air inside the cavity frequently controls those, i.e. a large amount of inactive hot wall area experiences large convective losses. His results show good agreement between the model and experimental results. Clausing, Waldvogel & Lister (1987) carried an experimental investigation of natural convection in an isothermal cubic cavity with a diversity of side-facing apertures in a cryogenic wind tunnel, focusing in large Rayleigh number and large ratios of the cavity wall and ambient temperatures, aiming to understand the mechanisms in large solar-receivers. Their results provided a global Nusselt number correlation, however limited to large Rayleigh numbers, as mentioned above ($3 \cdot 10^7 < Ra < 3 \cdot 10^{10}$).

Steinfeld & Schubnell (1993) describe a semi empirical method to determine the optimum aperture size and operating temperature of a cavity receiver. Their results showed that this optimization depends strongly on the incident flux distribution at the aperture of the receiver. Ma (1993) performed tests to determine the convective heat loss behavior of a cavity receiver with various tilt angles and wind speeds ranging from 0 to 24 mph (38.6 km/h) in sideways and head-on conditions. The results showed that natural convective was maximum when the receiver was facing horizontally, and negligible when the receiver was facing downwards. The same trend was found for side-on wind tests, whereas for head-on wind, convective heat loss is generally lower than for side-on wind. The author also made correlations for convection losses that are said to be only for the particular receiver in which the tests were made.

A controlled experiment was made by McDonald (1995) in order to quantify thermal losses (radiative, conductive, and convective), determining the effects of receiver angle, aperture size, and operating temperature on those losses. He proposes a convective loss correlation, approaching the mentioned parameters.

Fang et al. (2011) proposed a combined method for evaluate the thermal performance of a cavity receiver to produce saturated steam under different wind behaviors by applying a Monte-Carlo method added to the boiling flow heat transfer correlations and the calculation of the air flowing around the receiver. The results demonstrate that the velocity of air around the tubes affects directly the receiver heat loss, and when the wind comes from the lateral of the receiver, the air velocity reaches the maximum value. Figure 3.29 shows the heat loss over the flow direction of wind, where the maximum heat loss occurs when the wind comes from the side of the receiver (90°) with the maximum wind speed analyzed (9 m/s).

Figure 3.29 - Thermal losses results obtained by Fang et al. (2011) under windy conditions.



Source: Fang et al. (2011).

Hinojosa et al. (2005) demonstrates numerical results of transient and steady state heat transfer and airflow (natural convection and radiation losses) in an open 2D cavity based applying a Boussinesq approximation with laminar flow. Similarly work was done by Gonzalez, Palafox & Estrada (2012), where numerical results of natural convection and radiation in an 2D open cavity receiver with large temperature differences (between 100 K to 400 K) were calculated, also using variable fluid properties, where they concluded that for large temperature differences the radiative heat transfer is more important than convective one.

Kumar & Reddy (2007) investigates a 2D model of a modified cavity receiver to estimate the total and natural convection heat loss over two configurations of insulation (with and without insulation) and two receiver inclinations (0° , facing sideways, and 90° , facing down). The maximum convection heat loss occurs at 0° inclination for both cases, with insulation, it represented 63% of the total losses, and without insulation it represented 42.8% of the total amount, and declines uniformly with the angle rising to 90° .

Wu et al. (2013) conducted an experimental investigation of the effects of tilt angle, heat flux, and surface boundary condition on the heat loss of a fully open cavity receiver, analyzing the bottom surface heated, the side surface heated, and all of them heated, with the receiver rotating from 0° (horizontal) to 90° (facing downwards). The authors concluded that temperatures in the bottom surface fluctuates in a small region, whereas, the side surface temperature decreases with an increasing tilt angle. Natural convection losses are also more sensitive regarding the tilt angle than radiation and conduction losses. The authors also presented empirical correlations of natural convection, radiation and total heat loss Nusselt numbers as function of the Grashof number, tilt angle, and ambient temperature.

Li et al. (2010) developed a $100 \text{ kW}_{\text{th}}$ molten salt cavity receiver steady-state thermal model, analyzing the receiver area, heat loss (convective, emissive, reflective and conductive), the number of tubes in the panel, the tube's diameter and the receiver surface temperature. Their results shown that a receiver area of 0.2895 m^2 with 2 panels could satisfy the $100 \text{ kW}_{\text{th}}$ requirements with inlet temperature of $290 \text{ }^\circ\text{C}$ and outlet temperature of $560 \text{ }^\circ\text{C}$.

Samanes, García-Barberena & Zaversky (2015) made a survey of different natural convection correlations presented by different authors in order to model natural convective heat losses in cavity receivers, applying their model in simulations in Modelica. She presents four studies as the most relevant ones. The simulation results have shown that three models have similar performance characteristics, while one tends to overestimate the convective heat losses for the cavity.

Leibfried & Ortjohann (1995) used a test facility to show flow patterns and temperature behavior in a hot cavity receiver for different parameters and inclinations. They used two geometries (spherical and hemispherical cavity) with inner diameter of

400 mm and aperture ranging between 60 mm to 195 mm, and temperatures ranging from 573 K (300 °C) to 873 K (600 °C). They concluded that for upward-facing cavity receivers the convective losses are dominant, where the maximum was located between -30° and -60° from the horizon in a counterclockwise rotation, depending on the cavity geometry. In addition, for small wind speed, the dependence on wind is much smaller in sideward and downward-facing cavities, when it can even reduce the effect.

Taumoefolau et al. (2004) carried a testing with an electrically heat model receiver, with varying inclinations (from -90°, cavity facing up, to 90°, cavity facing down), with temperatures varying from 450 °C to 650 °C, and different ratios of aperture diameters to cavity diameter between 0.5 to 1, and performed a CFD simulation. Their experimental and simulation results agree. The authors comment that published models predict zero convection losses when the receiver is 90 degrees, i.e. facedown, where their contribution says it to be incorrect.

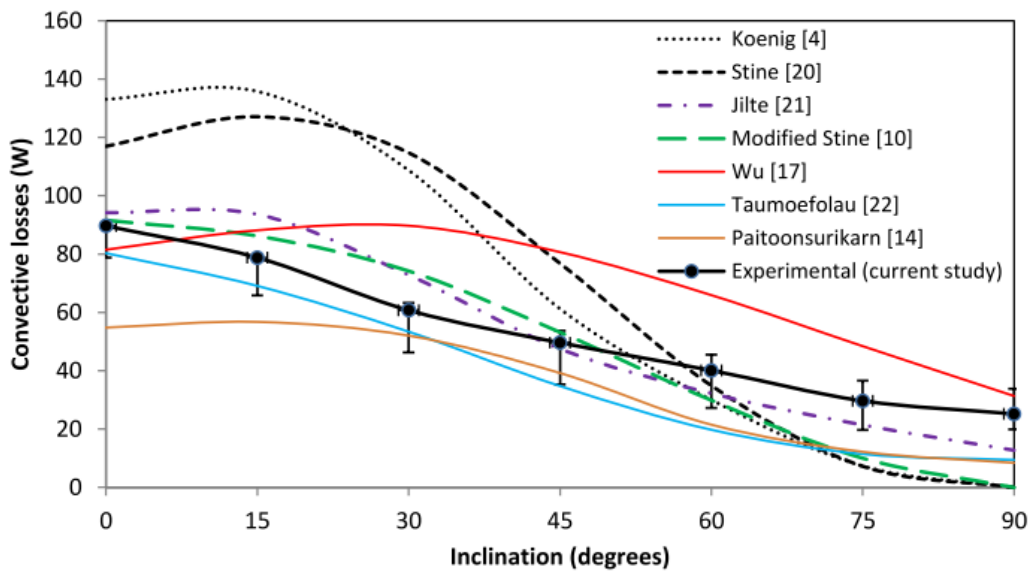
Siebers & Kraabel (1984), from Sandia National Energy Laboratories, reported a global heat transfer coefficient for a cavity cubical receiver and external cylindrical receiver as function of the Grashoff number, average temperature inside the cavity and ambient temperature.

Wan et al. (2017) used xenon lamps to supply the energy needed in an experimental platform, studying the cold startup and steady state performance of a cavity receiver with water as fluid, and 0.5 MPa of inlet pressure. The results have shown that temperature over the boiling panels are affected not only by heat flux, but other parameters like fluid flow and wind effect, result in a non-uniform temperature distribution on the boiling panels. They also say that the stagnation zone, i.e. a point in a flow field where the fluid velocity is zero, does exist and its boundary varies with a different energy input, hence affecting the convective loss.

Abbasi-Shavazi, Hughes & Pye (2014) examined experimentally cylindrical cavity models with cavity length to diameter ratios of 1 and 2, and aperture diameter to cavity diameter ratios of 0.5 and 1, subjecting the cavities to heat input through heating cables and different inclinations, where the operating temperature (650 °C) provided a better understanding of the heat losses mechanisms. The results showed to be consistent with the stagnation and convection zones present in cavities, with increasing inclination angle, and the temperature distribution over the cavity varies

naturally due to local radiative and convective losses. They demonstrate an increasing trend in radiative losses with the cavity inclination proportionally. In Figure 3.30, the authors made a comparison of convective losses in relation to the receiver inclination presented in the literature. Some works overestimated convection losses in inclinations of 15° and 30°, and underestimate the losses in higher inclinations. In addition, it is possible to notice a contrary trend from the convection losses with inclination when in comparison with radiation losses. Here, convection losses tend to decrease with an increase on the receiver inclination.

Figure 3.30 - Convective losses based on different cavity inclinations.



Source: Abbasi-Shavazi, Hughes, and Pye (2014).

Pye et al. (2017) handled an experimental testing of a high-flux cavity receiver, called “SG4”. The receiver achieved a 97.1% thermal efficiency, which is said to be in agreement with an integrated model at running at the design conditions, where a thermal efficiency of 98.7% was estimated (the cause of this variation is said to be the wind presence during experiments, which was not considered in the model). In addition, they reached a *quasi*-steady-state outlet steam temperature of 560 °C.

Prakash, Kedare & Nayak (2009) used a similar tubular cavity receiver to analyze both experimentally and numerically the heat losses in the receiver, presented in Figure 3.31. The receiver dimensions are 0.3 m of internal diameter, 0.5 m height, and 0.5 m diameter and 0.08 m height wind skirt. The experiments were conducted with temperatures ranging from 50 °C up to 70 °C and different receiver inclinations (0°, facing sideways, 30°, 45°, 60°, and 90°, facing downwards). The numerical CFD

study used temperatures ranging from 50°C to 300 °C and 0°, 45° and 90° inclinations. The results showed that convective losses increase with mean receiver temperature, and decreases with receiver inclination. In addition, the authors proposed a Nusselt Number correlation, where the correlations existing on the literature under-predict convective losses at mean temperatures (100 °C to 300 °C), because the correlations are developed for certain geometries where the ratio of aperture diameter to the receiver diameter are equal or lesser than one.

Figure 3.31 - Prakash, Kedare & Nayak (2009) cavity receiver.



Source: Prakash, Kedare, and Nayak (2009).

Flesch et al. (2016) applied two different measures to reduce convective losses (an air curtain and a partial wood window covering on third of the aperture). The systems were analyzed in a cryogenic wind tunnel at -173 °C, which allows the results to be extrapolated to large scale receivers, and were analyzed with CFD model also (the curtain had only numerical analysis). Their results showed that although the calculated losses were lower than the measured, the model can give a good prediction of changes, and both strategies are capable of increasing the efficiency by reducing the losses, where the air curtain showed best results (up to 50% of loss reduction) especially for low inclination angle.

Lee et al. (2017) assessed the effect of aspect ratio and head-on wind speed on force and natural convective heat loss and area-averaged convective heat flux from a cylindrical solar cavity receiver. Their results have shown that by increasing the aspect ratio varying the cavity length resulted in an increase increases not only the surface area on the air side of the cavity driving convective heat loss, but also of the area exposed to the transfer heat fluid, which can drive useful heat gain for conversion

to heat power, leading to potential efficiency increase. In addition, a small increase in the wind speed from zero reduces the combined convective heat loss below the value for natural convection. Added to that, the higher the aspect ratio, the smaller the effect of wind speed on combined convective heat loss per unit of area.

In order to improve the performance of receivers, different strategies have already been used. As an example, in order to reduce the aperture size, a nonimaging secondary concentrator are placed in the receiver's aperture, such as a Compound Parabolic Concentrator (CPC). In this scope, Blázquez, Carballo & Silva (2016) conducted a study to optimize the shape of a cavity receiver using a concentrator in order to fulfill the requirements of flux distribution on the walls of the receiver (homogeneous temperature distribution over the absorber surface). The ray-tracing software Tonatiuh was used, taking into account different geometrical parameters from both the CPC and the receiver cavity.

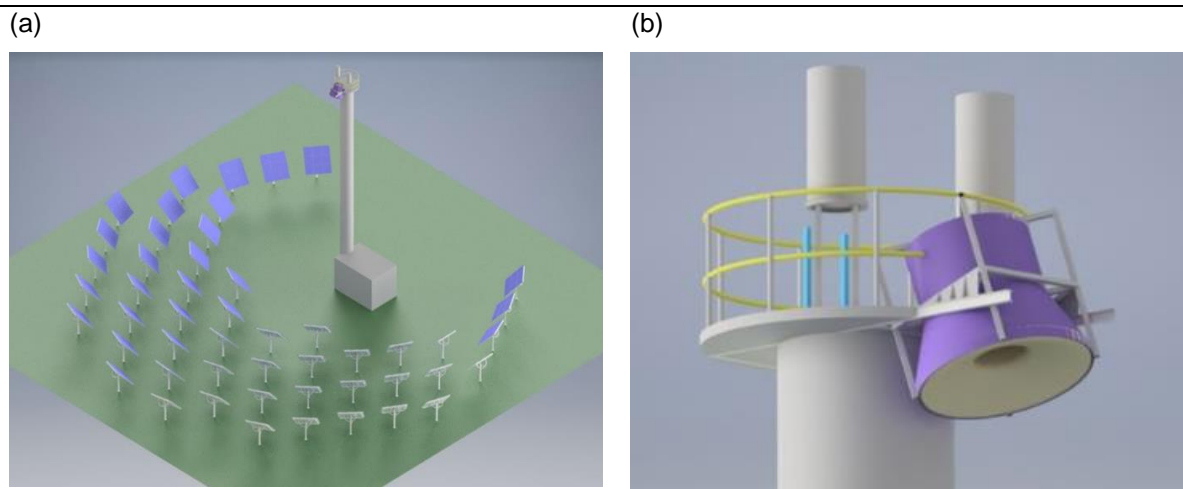
Another strategy is a window on the aperture, aiming to reduce convection losses. Z'graggen & Steinfeld (2004) analyzed a solar thermochemical reactor with two cavities in series with a spectrally selective quartz window positioned at its aperture and an insulated enclosure where the cavity is located, and compares the results afterwards with a windowless case. Their results demonstrate that the reactor with window reaches a higher maximum temperature than the windowless case. However, the insertion of a window has a negative effect on the absorption efficiency at lower temperatures, whereas at higher temperatures this issue is less significant.

Maag, Falter & Steinfeld (2011) also studied a high-temperature solar cavity receiver with a spectrally selective quartz and sapphire window. The window and cavity temperatures were calculated as function of incoming radiative flux and solar energy absorption efficiency, and compared with a windowless case. The results (temperatures) increase with the incoming radiative flux, and decreased with the solar energy absorption efficiency. The sapphire window temperatures were lower than the quartz window due to its higher reflectance.

4. Methodology

The target of this work is to simulate numerically the cavity receiver to be applied in Caiçara's cogeneration plant, depicted in detail in Figure 4.1 (b). Nevertheless, the heliostat field, shown in Figure 4.1 (a), must also be studied in detail to foresee the incoming radiation into the receiver in order to assess its transient behavior, water mass flow, steam generation, thermal efficiency, among other parameters. Hence, the next subchapters describe the methodology to achieve that goal.

Figure 4.1 – (a) Caiçara's tower and heliostat field, and (b) the cavity receiver in detail.



Source: GREEN (2018).

4.1. Meteorological Data

The first step consists in reducing the meteorological raw data from Caiçara's on site weather station, available from May 16th until August 12th, 2018, with minute time step data acquisition. Here occurs the parameters' filtering, such as average ambient temperature [°C] and DNI [W/m²], to exclude implausible values (e.g. DNI above 1,100 W/m² or wind speed values below 0 m/s).

4.2. The Heliostat Field

DLR dimensioned and designed the solar field through the software STRAL. For this analysis, a Monte Carlo ray-tracing model using the software Tonatiuh was applied to the DLR design in order to determine the field efficiency matrix, i.e. the optical efficiency of the heliostat-receiver system in function of solar position (azimuth angle – γ_{az} , and elevation angle – φ_{el}).

The conception of the solar field efficiency (η_{sf} [-]) as function of the collecting efficiency (η_{col} [-]), which is a function of the receiver aperture radius (r_{ap} [m²]); the cosine efficiency (η_{cos} [-]); and the mirror reflectivity efficiency (η_{ref}) is presented in Eq. (4.1). The efficiency of each Section (η_{Aap} [-]), as presented next, was related to the collecting area.

$$\eta_{sf}(\gamma_{az}, \varphi_{el}) = \eta_{col}(r_{ap}) * \eta_{cos} * \eta_{ref} [-] \quad (4.1)$$

The heliostat field Cartesian position is presented on [Appendix A](#).

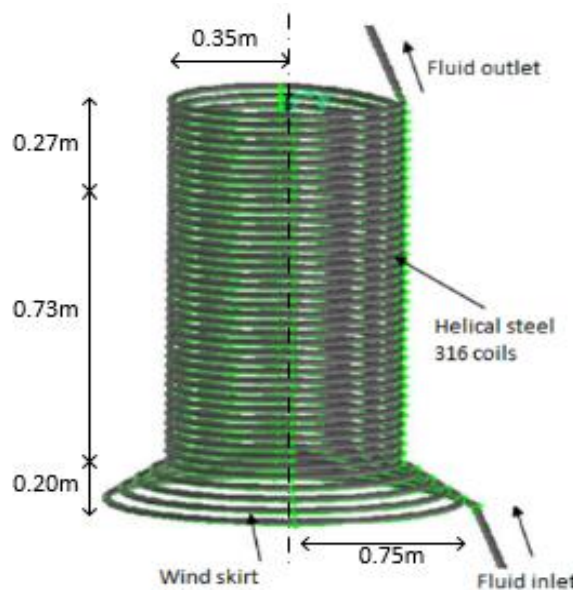
4.3. The Receiver

4.3.1. The Receiver Properties

The main goal for a detailed receiver thermal model is to predict with accuracy the thermal power that is absorbed by the receiver, comprising the net flux that reaches the receiver and its losses to the environment, considering the receiver's geometry and materials (WAGNER, 2008).

The Caiçara's system, as mentioned above, will use the ANU SG4 with modified coil dimensions. Figure 4.2 depicts the simplified geometry adopted on this work, with three different sections and its dimensions.

Figure 4.2 – Simplified geometry and dimensions.



Source: The author, adapted from Prakash, Kedare, and Nayak (2009).

Schedule 10 DN15 pipes will compose Section 1, whereas Schedule 10 DN20 will compose the first 20 loops of Section 2, and Schedule 10 DN25 pipes will compose Section 2 dome. Table 4.1 summarizes the dimensions. Also, the pipes are coated with Pyromark 2500 with solar absorptance of 0.95 and long wavelengths emittance of 0.85 (HO et al., 2012).

Table 4.1 – Coil dimensions for each section.

Section	Outer Diameter [m]	Inner Diameter [m]	Pipe Length [m]
Section 1 (DN15)	0.02134	0.01582	42.479
Section 2 (DN20)	0.02667	0.02093	59.420
Section 3 (DN25)	0.03340	0.02664	21.700

Source: The author.

Through those dimensions, and using Stainless Steel 316 density of 7,960 kg/m³ (KARDITSAS; BAPTISTE, 2019), was possible to determine the mass of coil for each section, as presented ahead. The average specific heat \bar{c}_p of 512.25 J/kg.K was used also through polynomial correlation as function of the temperature (KARDITSAS; BAPTISTE, 2019).

Table 4.2 – Coil mass for each section.

Section	Mass [kg]
Section 1	54.474
Section 2	101.497
Section 3	55.062

Source: The author.

The thermal conductivity as a function of the temperature (in K) as a polynomial correlation used is presented in Eq. (4.2) (KARDITSAS; BAPTISTE, 2019):

$$k = 9.0109 + 0.015298 * T \left[\frac{W}{m.K} \right] \quad (4.2)$$

In addition, the assumption of a Thermofelt blanket insulation from Unifrax with 0.2 m width to reduce losses was made. The foam blanket has a thermal conductivity of 0.04 W/m.K, considered constant, and a 96 kg/m³ density, and a considered constant specific heat \bar{c}_p of 480 J/kg.K.

Table 4.3 – Blanket insulation mass for each section.

Section	Mass [kg]
Section 1	17.405
Section 2	30.427
Section 3	13.916

Source: The author.

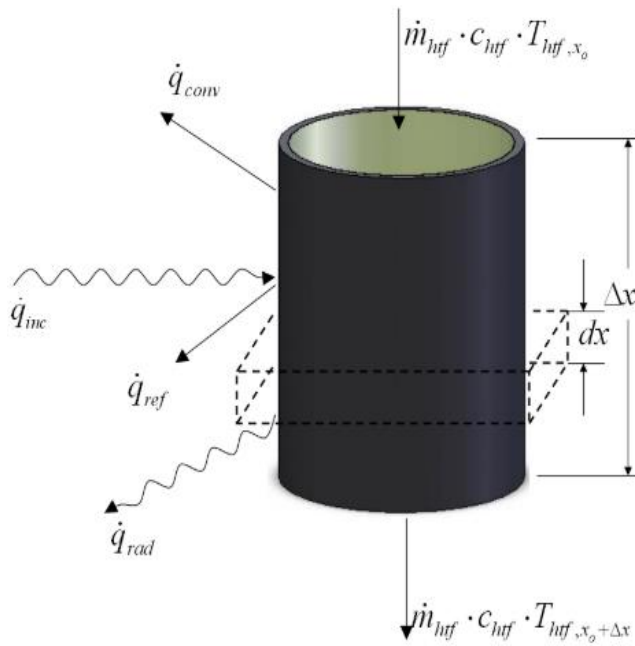
Sections 2 and 3 were considered together for the receiver model, whereas for the tube model, these Sections are considered separately.

4.3.2. The Receiver Model

A one dimensional (1-D) spatial and temporal discretization was applied on the receiver. The thermal model consists of an energy balance between the net power that reaches its sections, from now on named Section 1 (“S1”, also called “wind skirt”) and Section 2 (“S2”, sum of previous Sections 2 and 3, where the cavity is located), and thermal losses.

Figure 4.3 presents a 2-D exemplification of the model heat transfer mechanisms as fluxes: incident radiation flux (\dot{q}_{inc}) coming from the heliostat field; convection losses flux (\dot{q}_{conv}) due to the presence of external flow (wind speed) in the pipes; reflection losses flux (\dot{q}_{ref}); and re-radiation losses flux (\dot{q}_{rad}) to the surroundings, all which are expressed in W/m²; the water mass flow (\dot{m}), specific heat (c_{HTF}), temperature (T_{HTF}), the tube’s length (Δx), and infinitesimal length (dx).

Figure 4.3 – Energy balance in a small section of the tube.



Variables:

- $\dot{q}_{inc} \left[\frac{W}{m^2} \right]$ – incident radiation flux
- $\dot{q}_{conv} \left[\frac{W}{m^2} \right]$ – convection losses flux
- $\dot{q}_{ref} \left[\frac{W}{m^2} \right]$ – reflection losses flux
- $\dot{q}_{rad} \left[\frac{W}{m^2} \right]$ – re-radiation losses flux
- $\dot{m}_{HTF} \left[\frac{W}{m^2} \right]$ – heat transfer fluid mass flow rate
- $c_{HTF} \left[\frac{J}{kg.K} \right]$ – heat transfer fluid specific heat
- $T_{HTF} [K]$ – heat transfer fluid temperature
- $dx [m]$ – arc length of an infinitesimal element
- $\Delta x [m]$ – tube length

Source: Wagner (2008).

The incident radiation ($\dot{Q}_{inc} [W]$) is a relation between the DNI that reaches the heliostat field, the solar field efficiency as a whole ($\eta_{sf} [-]$), the collect efficiency of the aperture of each section ($\eta_{Aap} [-]$), all variable throughout the day, and the mirror area, which is the heliostat mirror area (9 m²) times the number of heliostats (50), resulting in 450 m² of mirror area, as in Eq. (4.3).

$$\dot{Q}_{inc} = DNI * \eta_{sf} * \eta_{Aap} * A_{mirror} [W] \quad (4.3)$$

The reflection losses ($\dot{Q}_{ref} [W]$) are a relation between the absorptance ($\alpha [-]$), here considered 0.85 for Section 1 and 0.99 for Section 2 (cavity effect), and proportionally to the incident radiation, as in Eq. (4.4).

$$\dot{Q}_{ref} = (1 - \alpha) * \dot{Q}_{inc} [W] \quad (4.4)$$

The re-radiation ($\dot{Q}_{rad} [W]$) and convective losses ($\dot{Q}_{conv} [W]$) applied are as follows. The first consists in the Stefan-Boltzmann law as the multiplication between the Stefan-Boltzmann constant (σ), which is $5.67 * 10^{-8} \left[\frac{W}{m^2.K^4} \right]$, the apparent emissivity ($\varepsilon_{ap} [-]$), considered 0.85 for Section 1 and 0.99 for Section 2, the aperture area of each

section, and the difference between the object temperature (T_s [K]), i.e. steel or foam and ambient temperature (T_∞ [K]), both raised to the fourth power (WAGNER, 2008):

$$\dot{Q}_{rad} = \sigma * \varepsilon_{ap} * (T_s^4 - T_\infty^4) * A_{ap} [W] \quad (4.5)$$

Approaching convective losses, the segmentation between the two Sections with different methodologies was applied. The general equation of convective losses is presented in Eq. (4.6), which consists in the multiplication of the average heat convection coefficient ($\overline{h_{air}}$ [W/m².K]), the aperture area, and the temperature difference between the steel and the air.

$$\dot{Q}_{conv} = \overline{h_{air}} * (T_s - T_\infty) * A_{ap} [W] \quad (4.6)$$

The air convective heat transfer coefficient can be calculated through the relation between the Nusselt number, the air thermal conductivity (k_{air} [W/m.K]) and the characteristic length (expressed as the ration between the surface area and the perimeter, i.e. $L_c \approx A_s/P$ [m]) (INCROPERA et al., 2007):

$$\overline{h_{air}} = \frac{Nu * k_{air}(T)}{L_c} \left[\frac{W}{m^2.K} \right] \quad (4.7)$$

The air thermal conductivity (k [W/m.K]), Prandtl number (Pr [-]), kinematic viscosity (ν [m²/s]), and thermal diffusivity (α [m²/s]) were calculated as a function of temperature, in Kelvin, through a polynomial correlation with tabulated data (ÇENGEL; BOLES, 2015). However, the Nusselt number demands other parameters that must be calculated firstly. All the fluid properties were evaluated at the thin film temperature, i.e. $T_f \equiv (T_s + T_\infty)/2$ [K].

$$k_{air}(T) = -1.10^{-8} T^2 + 7.10^{-5} T + 0.0242 \left[\frac{W}{m.K} \right] \quad (4.8)$$

$$Pr_{air}(T) = 7.10^{-14} T^4 - 3.10^{-10} T^3 + 5 * 10^{-7} T^2 - 3 * 10^{-4} T + 0.73 [-] \quad (4.9)$$

$$\nu(T) = 5.10^{-10} T^2 + 1.10^{-6} T + 0.0001 \left[\frac{m^2}{s} \right] \quad (4.10)$$

$$\alpha(T) = 4.10^{-9} T^4 - 2.10^{-7} T^3 + 4.10^{-6} T^2 - 3.10^{-5} T + 6.10^{-5} \left[\frac{m^2}{s} \right] \quad (4.11)$$

The Nusselt number (Nu [-]) can be calculated by applying the inclined plate in free convection configuration, according to Incropera et al. (2007), for $Pr \geq 0.7$ and $10^4 \leq Ra_L \leq 10^9$. The relation is shown below.

$$\overline{Nu}_L = 0.52 * Ra_L^{\frac{1}{5}} [-] \quad (4.12)$$

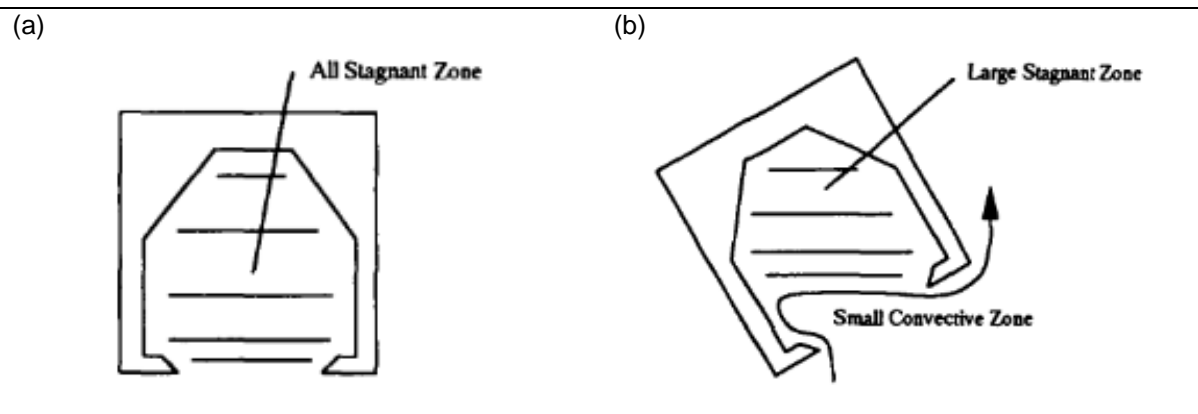
The Rayleigh Number (Ra_L [-]) can be determined as in Eq. (4.13), where g [m/s²] stands for the gravity, T_s [K] for the steel tube temperature, T_∞ [K] for the environment temperature, β [1/K] for the coefficient of thermal expansion (approximated as $1/\bar{T}_\infty$), L_c [m] for the characteristic length, ν for the kinematic viscosity, and α for the thermal diffusivity. In this case, since the receiver has an approximate 60° inclination (δ [°]), it is recommended that g is replaced by $g * \cos(\delta)$:

$$Ra_L = \frac{g * \cos(\delta) * \beta * (T_s - T_\infty) * L_c^3}{\nu * \alpha} [-] \quad (4.13)$$

4.3.2.1. Cavity Convection Methodology

Convection losses are particularly difficult to assess, since they are related to the air temperature inside the cavity, the inclination and geometry, and the wind conditions. According to Clausing (1983), if the aperture is located in the lower portion of the cavity, the air inside it supposedly stratifies and stay located in the upper region. Figure 4.4 illustrates the stagnant zone, with the receiver facing downwards, as well as the high tilt angle (regarding the horizontal). Similar zones patterns are were also presented by Prakash, Kedare & Nayak (2010).

Figure 4.4 – (a) All stagnant, and (b) large stagnant zone with small convective area.



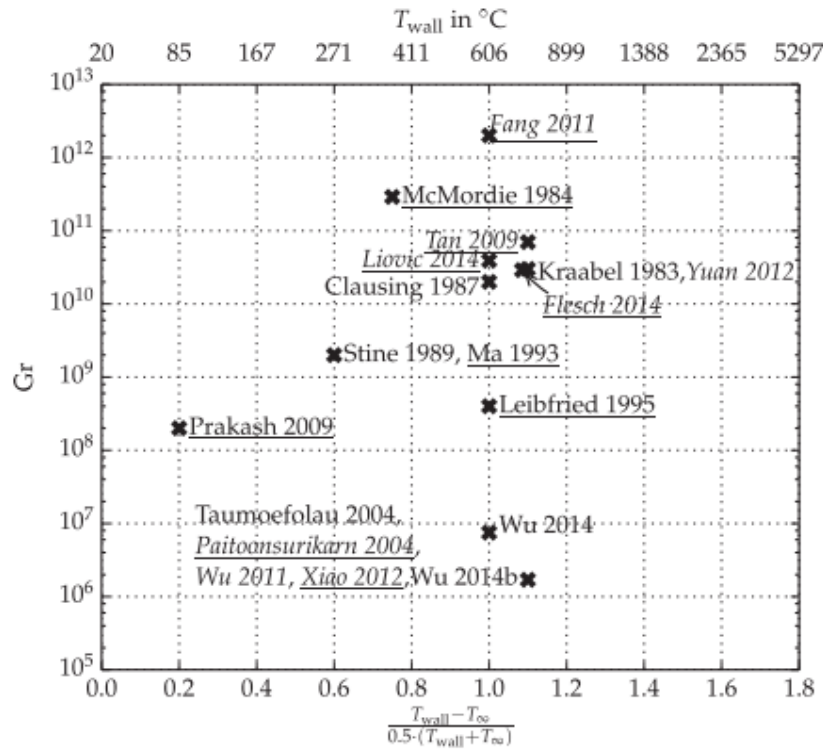
Source: Ma (1993).

Therefore, due to the cavity's inclination, as presented before, is important to analyze different methodologies for the convection losses.

Beforehand, a pre-analysis was carried out COMSOL 5.4 in order to assess the temperature gradient inside the cavity, as well as the zones within it. Considering a

threshold of 523K (250 °C) (arbitrarily chosen since it is slightly above the water outlet temperature, presented in [Chapter 3.4.1.3](#)) for wall temperature in Figure 4.5, Nusselt number correlations for convection losses proposed by Leibfried & Ortjohann (1995) and Stine & McDonald (1989) were assessed, as well as a correlation proposed by Paitoonsurikarn & Lovegrove (2006), not present in the figure below.

Figure 4.5 – Overview of convection loss studies.



Source: Flesch et al. (2015).

4.3.2.1.1. Leibfried & Ortjohann (1995)

Leibfried & Ortjohann (1995) presented a Nusselt number correlation accounting the receiver's cavity angular dependence ($h(\theta, \theta_{max}, \theta_{stag})$ [W/m².K]). Here, θ [°] represents the cavity inclination, θ_{max} [°] stands for the maximum heat loss angle, and θ_{stag} [°] stands for the stagnation angle; the cavity area (A_{cav} [m²]); the aperture area (A_{ap} [m²]); the Grashof number (Gr [-]) (ratio between the Rayleigh and Prandtl numbers); and the ratio of the cavity steel tube (T_w [K]) and ambient temperatures (T_∞ [K]), as presented ahead. The air thermophysical properties were calculated on the film temperature.

$$Nu_L = 0.106 * Gr^{\frac{1}{3}} * \left(\frac{T_w}{T_\infty}\right)^S * \left(4.256 * \frac{A_{ap}}{A_{cav}}\right) * h(\theta, \theta_{max}, \theta_{stag}) \quad [-] \quad (4.14)$$

$$Gr_L = \frac{g \cdot \beta \cdot (T_w - T_\infty) \cdot L_c^3}{\nu^2} = \frac{Ra_L}{Pr} \quad [-] \quad (4.15)$$

$$s = 0.56 - 1.01 \cdot \left(\frac{A_{ap}}{A_{cav}} \right)^{\frac{1}{2}} \quad [-] \quad (4.16)$$

In Eq. (4.15), g [m/s²] stands for the gravity, β [1/K] for the coefficient of thermal expansion, L_c [m] for the characteristic length, and ν [m²/s] for the kinematic viscosity.

As reported by the authors, the angle which the part of the cavity that is situated in the stagnant zone (θ_{stag} [°]), is generally 90° from the horizontal, i.e. the cavity facing downwards, value applied in this work. For the maximum heat loss angle (θ_{max} [°]), Eq. (4.17) is used, being limited to ratio $A_{ap}/A_{cav} \leq 0.2$ (which in this case is 0.175).

$$\theta_{max} = -23^\circ - 260^\circ \cdot \frac{A_{ap}}{A_{cav}} \quad [^\circ] \quad (4.17)$$

An angle of reference ($\bar{\theta}$) is here used:

$$\bar{\theta} = \frac{\theta - \theta_{stag}}{\theta_{max} - \theta_{stag}} \quad [^\circ] \quad (4.18)$$

The convective coefficient ($h(\theta)$) can be determined as function of the angles:

$$h(\theta) = \frac{1}{h_0} \cdot (1 - \cos(\bar{\theta}^{0.85} \cdot \pi)) \quad [-] \quad (4.19)$$

where

$$h_0 = 1 - \cos(\bar{\theta}(\theta = 0^\circ)^{0.85} \cdot \pi) \quad [-] \quad (4.20)$$

4.3.2.1.2. Paitoonsurikarn & Lovegrove (2006)

Paitoonsurikarn & Lovegrove (2006) presented a Nusselt Number correlation dependent on the Rayleigh based on length (Ra_L) and Prandtl (Pr) numbers for free convection, as in Eq. (4.21), for an ensemble length scale L_s [m], presented in Eq. (4.22).

$$Nu_L = 0.0196 \cdot Ra_L^{0.41} \cdot Pr^{0.13} = \frac{h \cdot L_s}{k} \quad [-] \quad (4.21)$$

$$L_s = \left| \sum_{i=1}^3 a_i \cdot \cos(\phi + \psi_i)^{b_i} \cdot L_i \right| \quad [m] \quad (4.22)$$

The parameters a_i , b_i and ψ_i are given by the authors based on empirical adjustments, summarized in Table 4.4. For the sum in Eq. (4.22), L_1 [m] represents the upper cavity diameter, L_2 [m] represents the cavity height, and L_3 [m] represents the

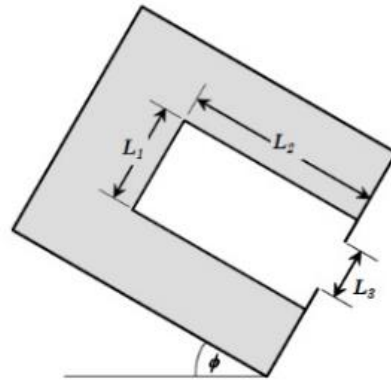
receiver aperture, whereas ϕ [°] stands for the receiver inclination, as in Figure 4.6 ahead.

Table 4.4 – Constants for the ensemble length scale.

i	a_i [-]	b_i [-]	ψ_i [rad]
1	4.08	5.41	-0.11
2	-1.17	7.17	-0.30
3	0.07	1.99	-0.08

Source: Paitoonsurikarn and Lovegrove (2006).

Figure 4.6 – Cavity receiver geometrical parameters.



Source: Paitoonsurikarn and Lovegrove (2006).

The Rayleigh number, for this case, is also calculated using the ensemble length scale, the cavity (T_w [K]) and ambient temperatures (T_∞ [K]), the kinematic viscosity (ν [m²/s]) and thermal diffusivity (α [m²/s]), both parameters of the Prandtl number [-], as shown above. The thermophysical properties of the air were evaluated at the film temperature.

$$Ra_L = \frac{g \cdot \beta \cdot (T_w - T_\infty) \cdot L_s^3}{\nu \cdot \alpha} \quad [-] \quad (4.23)$$

4.3.2.1.3. Stine & McDonald (1989)

The model proposed by Stine & McDonald is an extension of the model proposed by Siebers & Kraabel (1984) in order to include the receiver aperture and tilt angle as parameters. The Nusselt number correlation is a function of the Grashof number based on length, the wall temperature T_w [K], the ambient temperature T_∞ [K], the inclination θ [°], the aperture diameter d_{ap} [m], and the average internal dimension of the cavity L_D [m], as follows:

$$Nu = 0.088 * Gr_L^{\frac{1}{3}} * \left(\frac{T_w}{T_\infty}\right)^{0.18} * (\cos \theta)^{2.47} * \left(\frac{d_{ap}}{L_D}\right)^s \quad [-] \quad (4.24)$$

where

$$s = 1.12 - 0.98 * \left(\frac{d_{ap}}{L_D}\right) \quad [-] \quad (4.25)$$

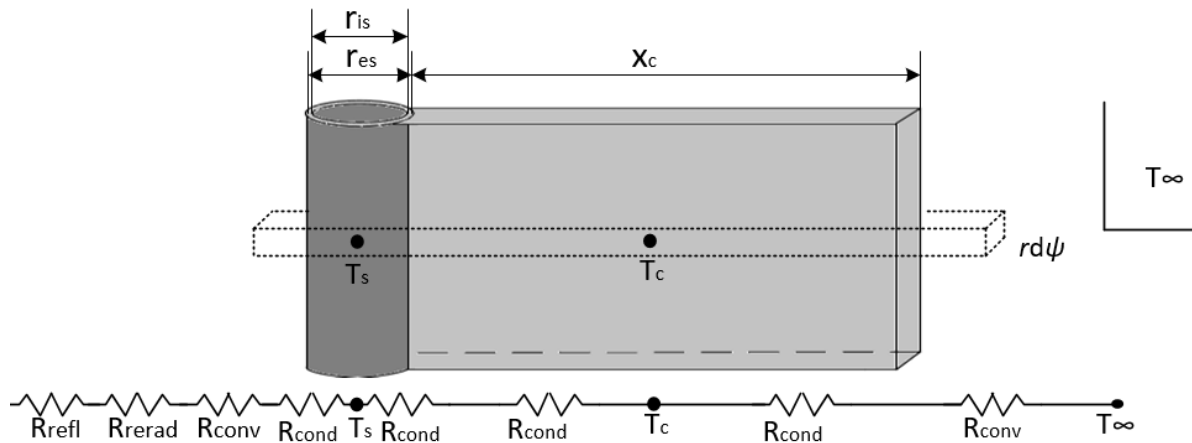
Here, the tilt angle is constrained to 0° (aperture sideways, looking horizontally) to 90° (aperture downwards), and all properties are taken at ambient temperature. Next is presented the conduction over the tube and ceramic foam losses.

4.3.2.2. Heat Transfer Model

The heat transfer through the tube and foam can be calculated by using the thermal resistance concept (INCROPERA et al., 2007). In this case, resistances in series are used to represent the heat transfer mechanisms.

Both the tube and foam were assumed as lumped elements (1-D spatial discretization) with uniform temperature throughout their volume (though differing between Section 1 and 2). Figure 4.7 shows the series resistance concept, where the steel tube is represented in darker gray, whereas the foam is represented in lighter gray. Here, r_{es} represents the external tube radius, while r_{is} represents the internal tube radius, and x_c represents the foam width. T_s and T_f represents both the average steel and ceramic foam temperatures, T_∞ represents the fluid (air) temperature, and $rd\psi$ is the arc length of an infinitesimal element.

Figure 4.7 – Thermal resistance concept for the tube and foam (cross section view of an infinitesimal element).



Source: The author.

The conduction resistance is a relation between the internal (r_i [m]) and external radius (r_e [m]), average thermal conductivity (\bar{k} [W/m.K]) and the surface area (A_s [m²]) for the steel cylinder (for the foam, it was considered a flat wall), whereas the convection resistance is a relation between the average heat convection coefficient (\bar{h} [W/m².K]). It is important to notice the minus signal on Eq. (4.26), which means that if $T_s > T_c$ the steel loses heat to the ceramic foam, and vice-versa. Same is valid for Eq. (4.27) with foam and external ambient.

$$\dot{Q}_{cond} = \dot{Q}_k = -\frac{1}{R_k} * (\bar{T}_s - \bar{T}_c) [W] \quad (4.26)$$

$$\dot{Q}_{conv} = \dot{Q}_{cv} = -\frac{1}{R_{cv}} * (\bar{T}_c - T_\infty) [W] \quad (4.27)$$

The steel and foam resistances (R_k) between T_s [K] and T_c [K] and between T_c and T_∞ [K], as well as the convection resistance are presented ahead, as a relation of the above-mentioned parameters and the geometry due to the internal (steel) and external (ceramic foam) areas. Here L_t [m] and A_s [m²] are the tube's length and surface area of each Section at the considered section, and r [m] the aperture radius. It is important to mention that \bar{r} [m] in Section 2 stands for the average internal and external tube radius.

Table 4.5 – Thermal conduction and convection resistances for each Section.

Section 1
$R_{k_s} = \frac{\ln(r_{es}/r_{is})}{2 * \pi * \bar{k}_s * L_{t_1}}$
$R_{k_c} = \frac{x_c/2}{\bar{k}_c * A_{s_{1c}}}$
$R_{cv_1} = \frac{1}{\bar{h} * A_{s_1}}$
Section 2
$R_{k_s} = \frac{\ln(\bar{r}_{es}/\bar{r}_{is})}{2 * \pi * \bar{k}_s * L_{t_2}}$
$R_{k_c} = \frac{x_c/2}{\bar{k}_c * A_{s_{2c}}}$
$R_{cv_2} = \frac{1}{\bar{h} * A_{s_2}}$

Source: The author.

Table 4.6 shows the conduction and convection heat transfer mechanisms (negative signal representing gradient of temperature).

Table 4.6 – Conduction and convection heat transfer equations for each Section.

Section 1
$\dot{Q}_{k_1} = -\frac{(\bar{T}_s - \bar{T}_c)}{\sum R_k} = -\frac{1}{\left(\frac{\ln(r_{es}/r_{is})}{2 * \pi * \bar{k}_s * L_{t_1}} + \frac{x_c}{\bar{k}_c * A_{s_{1f}}}\right)} * (\bar{T}_s - \bar{T}_c) [W]$
$\dot{Q}_{(k+cv)_1} = -\frac{(\bar{T}_c - T_\infty)}{\sum R} = -\frac{1}{\left(\frac{x_c}{\bar{k}_c * A_{s_{1c}}} + \frac{1}{\bar{h} * A_{s_1}}\right)} * (\bar{T}_c - T_\infty) [W]$
Section 2
$\dot{Q}_{k_2} = -\frac{(\bar{T}_s - \bar{T}_c)}{\sum R_k} = -\frac{1}{\left(\frac{\ln(\bar{r}_{es}/\bar{r}_{is})}{2 * \pi * \bar{k}_s * L_{t_2}} + \frac{x_c}{\bar{k}_c * A_{s_{2f}}}\right)} * (\bar{T}_s - \bar{T}_c) [W]$
$\dot{Q}_{(k+cv)_2} = -\frac{(\bar{T}_c - T_\infty)}{\sum R} = -\frac{1}{\left(\frac{x_c}{\bar{k}_c * A_{s_{2c}}} + \frac{1}{\bar{h} * A_{s_2}}\right)} * (\bar{T}_c - T_\infty) [W]$

Source: The author.

In the proposed method, two important assumptions were carried out: the temperature distribution is constant along the receiver tubers, i.e. isothermal, and the average temperature in the tubes and foam cross section is constant (Biot number $\ll 1$, equal to 0.0001 for the steel and 0.375 for the ceramic foam).

The temporal discretization was made applying a forward Euler approximation explicit time-stepping scheme. Every explicit time-stepping scheme remains stable until certain value of time step, and it must be equal or smaller than the time demanded to transfer information across the shape of spatial discretization scheme (BLAZEK, 2015). Hence, in order to ensure the model's stability, is necessary to calculate the critical time Δt time step, as it follows:

$$\dot{Q} = \frac{\Delta Q}{\Delta t} \rightarrow \Delta t < \frac{\Delta Q}{\dot{Q}} = \frac{m * c_p * \Delta T}{\dot{Q}} [s] \quad (4.28)$$

Herewith, considering an arbitrary maximum ΔT of 10 K during one time step, and using the lowest values of $m * \bar{c}_p$ (lowest thermal inertial), which in this case are from the foam for both Sections, and the DNI of design of 950 W/m² without considering any losses (most critical scenario), it's possible to calculate Δt for both sections:

$$\Delta t_1 = \frac{m_{1c} * c_{pc} * \Delta T}{DNI * \eta_{sf} * \eta_{Aap_1} * A_{mirror}} = 0.66 \text{ s} \quad (4.29)$$

$$\Delta t_2 = \frac{m_{2c} * c_{pc} * \Delta T}{DNI * \eta_{sf} * \eta_{Aap_2} * A_{mirror}} = 1.87 \text{ s} \quad (4.30)$$

The time step is then tuned until the system loses stability or no longer represents the system's initial behavior, i.e. steel and foam temperature variation over the day, with the Forward Euler approximation $\frac{dT}{dt} \approx \frac{\Delta T}{\Delta t} \approx \frac{T^{t+1} - T^t}{t^{t+1} - t^t}$ for the iterations.

Table 4.7 – Energy balance equations for each Section.

Section 1
$\Delta T_s = \frac{1}{m_{s_1} * C_{ps}} * [\dot{Q}_{inc} - (\dot{Q}_{ref} + \dot{Q}_{rad} + \dot{Q}_{conv} + \dot{Q}_{k_1})] * \Delta t_1 \text{ [s]}$
$\Delta T_c = \frac{1}{m_{c_1} * C_{pc}} * [-\dot{Q}_{k_1} + \dot{Q}_{(k+cv)_1}] * \Delta t_1 \text{ [s]}$
Section 2
$\Delta T_s = \frac{1}{m_{s_2} * C_{ps}} * [\dot{Q}_{inc} - (\dot{Q}_{ref} + \dot{Q}_{rad} + \dot{Q}_{conv} + \dot{Q}_{k_2})] * \Delta t_2 \text{ [s]}$
$\Delta T_c = \frac{1}{m_{c_2} * C_{pc}} * [-\dot{Q}_{k_2} + \dot{Q}_{(k+cv)_2}] * \Delta t_2 \text{ [s]}$

Source: The author.

After this step, the minimum value of Δt as time step was applied to calculate the mass flow of water passing in the coils. As mentioned in [Chapter 3.5.1.3](#), the water enters the receiver at 318 K (45 °C), heats up to almost 473 K (200 °C), and exits as superheated steam at 498 K (225 °C). In this conception, an arbitrary steel tube temperature of 523 K (250 °C) was chosen as a threshold from the “recirculating” stage to the “operational” stage. A mass flow relation can be made as it follows, where the

net heat (\dot{Q}_{net}) represents the incident radiation minus the thermal losses for both sections, as applied above:

$$\dot{Q}_{net} = \dot{Q}_{net_1} + \dot{Q}_{net_2} \quad [W] \quad (4.31)$$

Hence:

$$\dot{Q}_{net} = \dot{m} * \int_{T_{in}}^{T_{out}} C_p(T) * dT = \dot{m} * [h(T_{out}(225 \text{ } ^\circ\text{C})) - h(T_{in}(45 \text{ } ^\circ\text{C}))] \rightarrow \dot{m} = \frac{\dot{Q}_{net}}{h(T_{out}(225 \text{ } ^\circ\text{C})) - h(T_{in}(45 \text{ } ^\circ\text{C}))} = \frac{\dot{Q}_{net_1} + \dot{Q}_{net_2}}{h(T_{out}(225 \text{ } ^\circ\text{C})) - h(T_{in}(45 \text{ } ^\circ\text{C}))} \quad \left[\frac{kg}{s}\right] \quad (4.32)$$

Therefore, it is possible to calculate a variable water mass flow rate to maintain the superheated steam outlet temperature (T_{out}) always at 225 °C. In addition, net heat to water must follow two conditions: net heat must be positive (i.e. incident radiation must be higher than thermal losses), and the steel temperature must be higher than 250 °C. The thermal models were implemented firstly on MS Excel, and MATLAB afterwards.

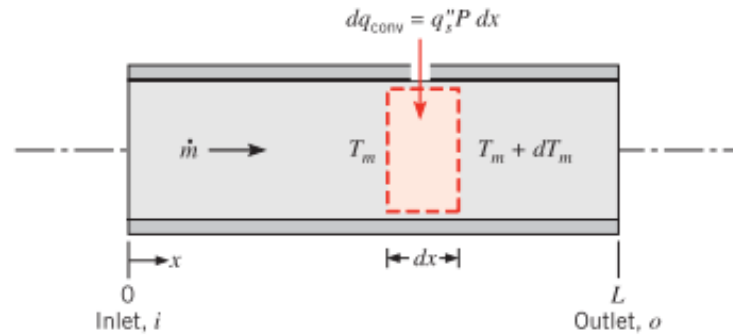
4.3.3. Ceramic Foam Sensitivity Analysis

A sensitivity analysis regarding the ceramic foam insulation length was carried with Leibfried and Ortjohann convective loss method. Four different lengths were applied to the thermal model, including the one used on it ($x_c = 0.05, 0.10, 0.20,$ and 0.30 m), in order to assess how the ceramic foam would influence the thermal losses and the receiver thermal efficiency.

4.3.4. Finite Volume Method

The Finite Volume Method was used to discretize the convective heat transfer and fluid dynamic effects within the tube, yielding in a more detailed model. The receiver was subdivided into three sections, accordingly to each tube diameter and length, as presented in [Chapter 4.3.1](#). The Figure 4.8 depicts the 2D control volume for the internal flow in a tube for an element dx to better understand the concept, even though the analysis was carried in 1-D, i.e. disregarding radial variations.

Figure 4.8 - Control volume for a Finite Volume Method.



Source: Incropera et al. (2007).

The FVM consists in the space discretization in order to solve differential equations, in this case, of heat transfer. Here are applied the 1-D continuity conservation equation, i.e. mass conservation, and 1-D conservation of energy, presented ahead (ROHSENOW; GARTNETT; CHO, 1998), where q_k is the conduction heat transfer, and u_x stands for the velocity:

$$\frac{\partial \rho}{\partial t} = \frac{\partial \rho}{\partial x} \cdot u_x \quad (4.33)$$

$$\frac{\partial \rho h}{\partial t} = \frac{\partial q_k}{\partial x} - \frac{\partial \rho h}{\partial x} \cdot u_x \quad (4.34)$$

To compute the water/steam properties within the tube, a Toolbox from the University of Applied Sciences Zittau/Görlitz was installed on MATLAB, containing the water/steam properties (KRETZSCHMAR, 2020). The Nusselt number [-] was considered 3.66 for laminar flow ($Re_D < 3000$) with constant surface temperature, and based on the Gnielinski correlation for turbulent flow, as in Eq. (4.35) (INCROPERA et al., 2007).

$$Nu_D = \frac{(f_t/8)(Re_D-1000)Pr}{1+12.7(f_t/8)^{1/2}(Pr^{2/3}-1)} [-] \quad (4.35)$$

The Moody/Darcy friction factor for the laminar flow for is shown in Eq. (4.36), whereas the Petukhov correlation was applied for the transient and turbulent flows (Eq. (4.37)), which encompasses large Reynolds numbers ($3000 \leq Re_D \leq 5 \times 10^6$).

$$f_l = \frac{64}{Re_D} [-] \quad (4.36)$$

$$f_t = (0.79 \ln(Re_D) - 1.64)^{-2} [-] \quad (4.37)$$

The convective heat transfer coefficient is then calculated as in Eq. (4.7). The heat transferred to water is computed as follows, where V_{dx} [m³] is the element volume, i.e. $\pi \cdot dx \cdot D$, where dx stands for the element length, and D [m] stands for the tube's diameter:

$$\dot{Q}_{water} = \bar{h}_{conv} \cdot V_{rdx} \cdot (T_s - T_{water}) [W] \quad (4.38)$$

The element outlet enthalpy is calculate based on the heat transferred, the water mass flow, and inlet element enthalpy:

$$h_{out} = \frac{\dot{Q}_{water}}{\dot{m}_{water}} + h_{in} \left[\frac{J}{kg} \right] \quad (4.39)$$

The pressure drop as a function of friction factor (f [-]), density (ρ [kg/m³]), velocity (u [m/s]), element length (dx [m]), and tube diameter (D [m]):

$$dp = - \int_{p_1}^{p_2} dp = f \cdot \frac{\rho \cdot u^2}{2D} \cdot dx [Pa] \quad (4.40)$$

The number of elements for the 1-D mesh was calculated based on the tube model with an enthalpy analysis considering a 0.128 kg/s water mass flow (maximum reached with cavity model), and steel tube at 523 K (250 °C). The criteria was small enough enthalpy variation (< 1%) in the same position over the tube's length when compared with the next doubled number. As previously mentioned, on the FVM, the receiver was segmented in 3 Sections regarding the tube's diameter.

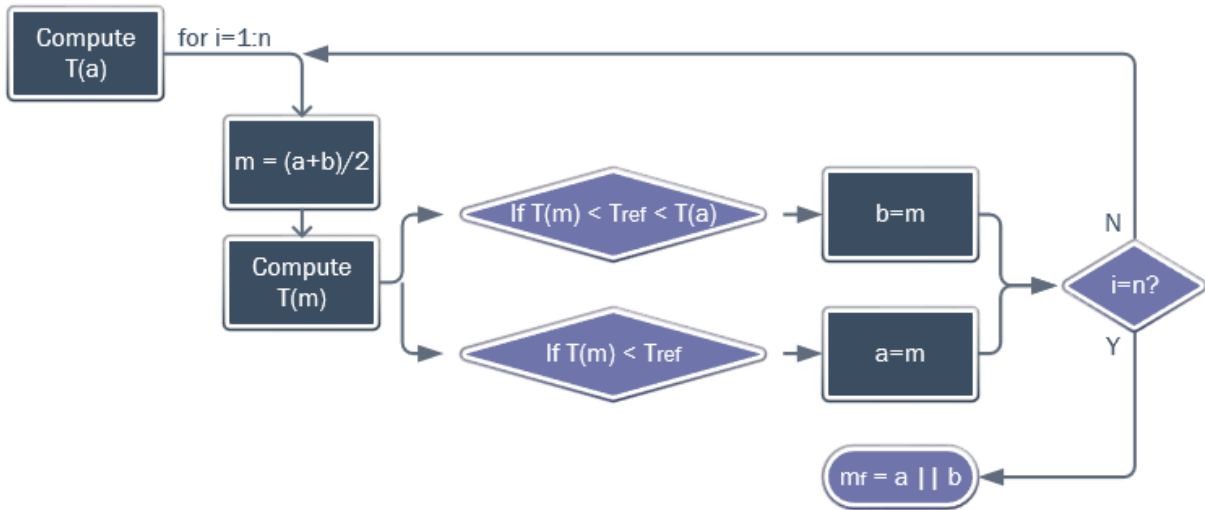
A primary pressure analysis was made in order to assess water outlet temperature, pressure drop, and steam velocity, aiming to find the most suitable pressure for the system. Here, a steady-state analysis with constant DNI value of 950 W/m², again water mass flow of 0.128 kg/s and steel temperature at 250 °C were applied. This step aimed to evaluate if the inlet pressure of 1.4 MPa (14 bar) would be plausible for the system, or if the inlet pressure should be changed.

Next, the Bisection Numerical Method was implemented in order to find the best fit water mass flow regarding the previous time step steel temperature. The Bisection Method is based on the intermediary value theorem, as can be summarized as: within a range [a,b] which contains the root, where "a" is the smaller value and "b" the larger,

is possible to build a succession of intervals, each one being the half of the previous range which contains the root.

In the present case, the root is a reference temperature $T_{ref} = T_{sat}(\rho_{in}) + 10\text{ K}$, where 10 K were added to avoid two-phase region. The main idea is that the smaller mass flow “a” within the range [a,b] results in $T_a \geq T_{ref}$, and $T_b \leq T_{ref}$. After “n” iterations, the water mass flow range is reduced to close values (“a” \approx “b”) where the outlet temperature T_a or T_b would be close enough to T_{ref} . The Bisection algorithm is explained in Figure 4.9:

Figure 4.9 – Bisection method algorithm.



The number of successive intervals “n” [-] can be expressed as follows, where ϵ is the absolute error of 1%:

$$n \geq \frac{\ln\left(\frac{b-a}{\epsilon}\right)}{\ln 2} \quad [-] \quad (4.41)$$

Therefore, the steel temperature could be calculated for each time step “t” for each Section “i” as in Eq. (4.42), now adding the heat transferred to the water, still considering the same thermal losses (reflection, re-radiation, convection, and conduction) and Δt as 3 seconds:

$$\Delta T_{st} = \frac{1}{m_{s_i} * c_{p_s}} * \left((\dot{Q}_{inc} - \dot{Q}_{thermal\ losses}) - \dot{Q}_{water} \right) * \Delta t \quad [K] \quad (4.42)$$

4.3.4. Model Comparison

A comparison of receiver efficiency and injected water mass flow between the previously formulated ANU “steady-state” SG4 and USP “transient” and a steady-state models was carried out. The comparison was made considering two selected days, January 21st and June 21st, considering three different times (solar noon “SN” = 11:35 h, SN + 2 h, and SN + 4 h, UTC-3), and DNI sets (1,000, 900, 800, and 500 W/m²). The operational parameters also changed: inlet pressure of 3.5 MPa (35 bar), and inlet water temperature of 80 °C, and steam temperature of 250 °C.

This comparison was made in order to assess if the receiver model presents reliable and realist results.

4.4. The Compound Parabolic Concentrator (CPC) Receiver

By applying the edge-ray principle into a cone concentrator, a Compound Parabolic Concentrator (CPC) is found. CPCs are non-tracking non-imaging collectors that are very close to being ideal concentrators, also having the maximum theoretical concentration ratio (WINSTON; MIÑANO; BENÍTEZ, 2005).

Sometimes, the CPC is applied on the receiver’s aperture as a secondary concentrator in order to increase the concentration ratio, intercepting most the energy coming from the primary concentrators, i.e. heliostat field in this case. Nevertheless, extra optical devices involve extra optical losses, and the use of the secondary concentrator makes sense if the energy increase due to a decrease in re-radiation exceeds these extra optical losses (SEGAL; EPSTEIN, 1999).

The methodology to simulate the system performance with a CPC applied three different models developed by a personal advising and communication, gathered up together afterwards. It makes use of different parameters of the Caiçara solar field and receptor, which are summarized in Table 4.8. The model does not approach thermal losses (conduction and convection). The CPC model was implemented on MS Excel.

Table 4.8 – Caiçara parameters used in the CPC model.

Parameters	Values
DNI_{design}	950 W/m ²
Mirror Area	450 m ²
Temperature	250 °C (523.15 K)
Mirror Reflectivity Efficiency	0.92
Cosine Efficiency	0.94
Aperture Radius	0.75 m

Source: Personal Communication.

Firstly, the Caiçara solar field properties such as heliostat configuration and solar field layout, as presented in “The Heliostat Field” subsection, were placed in Tonatiuh, resulting in the efficiency matrix, with mean flux ($\dot{q}(r_{ap})$ [W/m²]), power on aperture ($\dot{Q}(r_{ap})$ [W]) , and collection efficiency ($\eta_{col}(r_{ap})$ [-]) as functions of the receiver radius, as well as the solar field efficiency (η_{sf} [-]), as presented in Eq. (4.1).

The net power reaching the receiver with the DNI_{design} can be determined as:

$$\dot{Q}_{sf} = DNI_{design} * A_{mirror} [W] \quad (4.43)$$

Therefore, the net power reaching the CPC is:

$$\dot{Q}_{CPCin} = \dot{Q}_{sf} * \eta_{sf} [W] \quad (4.44)$$

The second step uses the properties of the Caiçara solar field and a CPC attached to the receiver, and applies a Monte-Carlo Ray Tracing (MCRT) model that uses the CPC properties such as the CPC radius (r_{CPC} [m]) and the CPC concentration ratio (C_{CPC} [-]) to generate the CPC efficiency ($\eta_{CPC}(r_{CPC}, C_{CPC})$ [-]), as well as the flux as functions of CPC radius, CPC concentration and entering flux, which comes from the previous step ($\dot{q}_{CPC}(r_{CPC}, C_{CPC}, \dot{q}(r_{ap}))$ [$\frac{W}{m^2}$]). This model also gives as output the reflection efficiency ($\eta_{refl_{CPC}}$ [-]), and the efficiency of the beams that passes through the CPC ($\eta_{through_{CPC}}$ [-]).

Thus, the CPC efficiency can be established as the relation ahead, as function of beams that passed through the CPC ($\eta_{throughCPC}$ [-]) and the beams that were reflected by it ($\eta_{reflCPC}$ [-]):

$$\eta_{CPC} = (C_{CPC} * \eta_{throughCPC})^{\eta_{reflCPC}} [-] \quad (4.45)$$

Hence, the net power that leaves the CPC (\dot{Q}_{CPCout} [W]) can be expressed as the relation between the net power coming in the CPC and its efficiency, as well as the flux leaving it (\dot{q}_{CPCout} [W/m²]):

$$\dot{Q}_{CPCout} = \dot{Q}_{CPCin} * \eta_{CPC} [W] \quad (4.46)$$

$$\dot{q}_{CPCout} = \dot{Q}_{CPCout} * A_{ap} = \dot{Q}_{CPCout} * (\pi * r_{ap}^2) \left[\frac{W}{m^2} \right] \quad (4.47)$$

Finally, the cavity receiver is modeled as follows, not approaching the losses, as mentioned above:

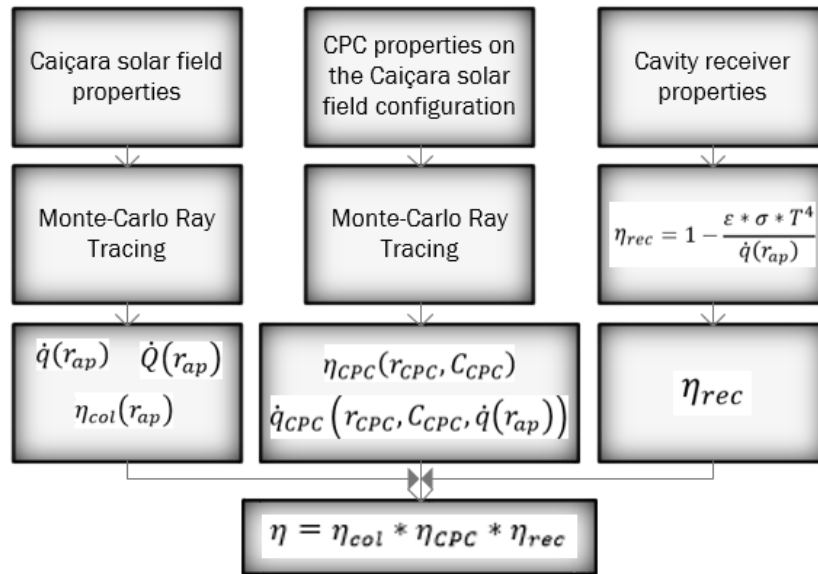
$$\eta_{rec} = 1 - \frac{\varepsilon * \sigma * T^4}{\dot{q}_{CPCout}} [-] \quad (4.48)$$

Thus, gathering the three models, the total efficiency of the current system with the CPC attached to the receiver can be calculated as:

$$\eta = \eta_{col} * \eta_{CPC} * \eta_{rec} [-] \quad (4.49)$$

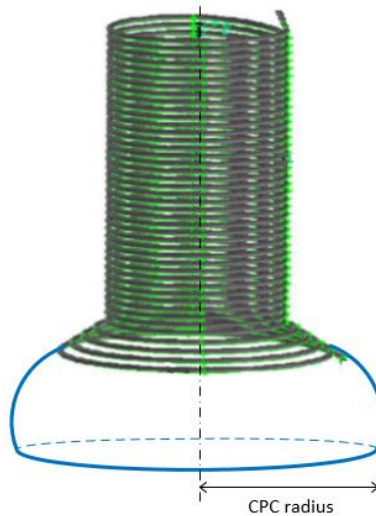
The flowchart in Figure 4.10 describes the logical approach of three models, as mentioned above, while Figure 4.11 depicts the schematic design of the CPC attached to the cavity receiver.

Figure 4.10 – Separate models for the Solar Field, CPC and cavity receiver efficiency calculation.



Source: The author.

Figure 4.11 – 3-D CPC-type attached to the solar receiver.



Source: The author.

4.5. The Quartz Window Receiver

A quartz window (SiO_4) is used to selectively transmit determined wavelengths to the inside of the cavity receiver, as well as to reduce losses (e.g. convection losses). Here, the receiver aperture is covered by a spectrally selective quartz window with optical properties summarized in Table 4.9, where E_λ stands for the emittance, R_λ stands for the reflectance, and V_λ stands for the transmittance (MAAG; FALTER; STEINFELD, 2011).

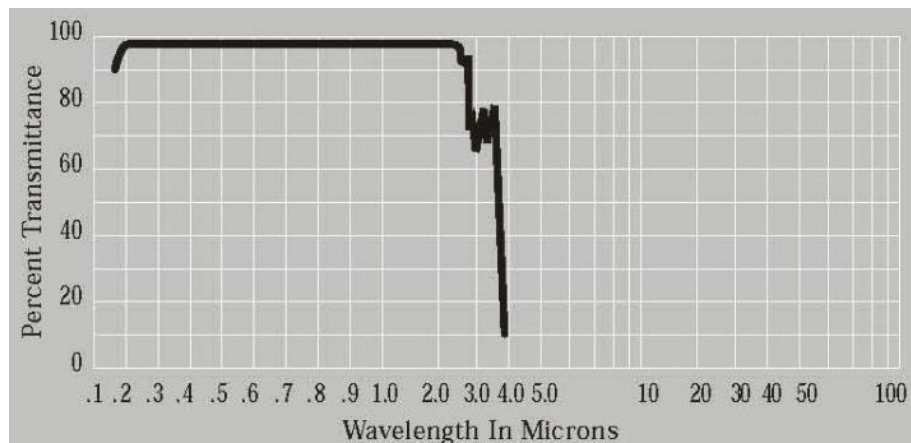
Table 4.9 – Quartz window optical properties.

Spectral band [μm]	E_λ	R_λ	V_λ
0-0.1	0.90	0.10	0.00
0.1-3	0.01	0.06	0.93
3- ∞	0.90	0.10	0.00

Source: The author, adapted from Maag, Falter & Steinfeld (2011).

Thus, this window is used to selective transmit the infrared radiation to the cavity. Figure 4.12 shows the transmittance curve of a quartz.

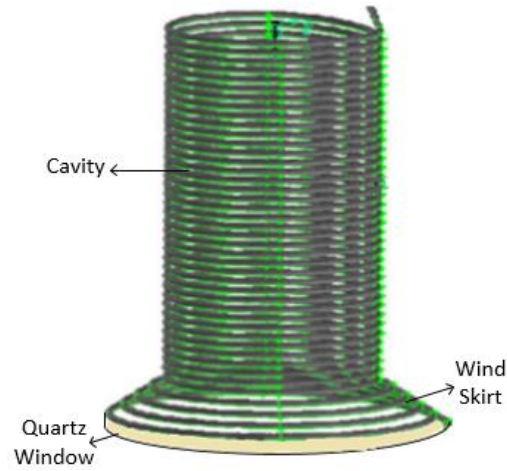
Figure 4.12 – Quartz transmittance as function of wavelength.



Source: Janis (2019).

In this case, the window is exposed to concentrated solar radiation, assumed to have the spectral distribution proportional to Planck's blackbody ($T_{\text{source}} = 5,780 \text{ K}$). Several assumptions are made, such as: diffuse window, no conductive or convective heat transfer between the window and cavity, opaque-gray-diffuse cavity walls, and uniform radiative heat flux, temperature (fixed for the cavity) and properties on both window surfaces. Figure 4.13 shows the schematic of the quartz window and receiver (with non-real dimensions).

Figure 4.13 – Solar receiver and quartz window scheme.



Source: The author.

The radiosity method for semitransparent enclosures is used to determine the system's equations in a spectral-dependent context, where the subscript "w" stands for window, and "c" for cavity (SIEGEL, 1973; MAAG; FALTER; STEINFELD, 2011):

$$-\frac{1-E_{\lambda,c}}{E_{\lambda,c}} \frac{dq_c}{d\lambda} + \frac{1}{E_{\lambda,w}} \frac{dq_w}{d\lambda} = -F_{W-c} * e_{\lambda b}(T_c) + 2 * e_{\lambda b}(T_w) - \frac{dq_{e,w}}{d\lambda} \quad (4.50)$$

$$\frac{1}{E_{\lambda,c}} (1 - R_{\lambda,c} F_{c-c}) \frac{dq_c}{d\lambda} - \frac{R_{\lambda,w}}{E_{\lambda,w}} F_{c-w} \frac{dq_w}{d\lambda} = (1 - F_{c-c}) * e_{\lambda b}(T_c) - (1 + R_{\lambda,w} - V_{\lambda,w}) * F_{c-w} * e_{\lambda b}(T_w) + \frac{R_{\lambda,w}(1-R_{\lambda,w})-V_{\lambda,w}(1-V_{\lambda,w})}{E_{\lambda,w}} * F_{c-w} * \frac{dq_{e,w}}{d\lambda} \quad (4.51)$$

The parameters $\frac{dq_c}{d\lambda}$ and $\frac{dq_w}{d\lambda}$ can be found for each wavelength interval through linear equation solving. For the cavity, the considered parameters are:

Table 4.10 – Cavity optical properties

E_{λ}	R_{λ}	V_{λ}
0.85	0.15	0

Source: The author.

The view factor, also called radiation share factor (i.e. proportion of radiation that leaves some surface and strikes the next) for the cavity-cavity can be determined through the reciprocity relations ahead:

$$F_{W-c} * A_w = F_{c-w} * A_c \rightarrow F_{c-w} = F_{W-c} * \frac{A_w}{A_c} [-] \quad (4.52)$$

$$F_{c-c} = 1 - F_{c-w} [-] \quad (4.53)$$

The incoming radiation per spectral band into the window and cavity (temperature dependent), as well as the outside incoming radiation can be determined as follows, where $\dot{q}_{e_w} = \dot{Q}_{inc}/A_{ap}$ [W/m²]. An important assumption was carried out: the window temperature grows linearly as function of the cavity temperature as $T_w = (0.6(T_c - T_\infty) + T_\infty)$ [K], which means that neither the cavity or the ceramic foam temperatures could be below the ambient temperature.

$$e_{\lambda b}(T_c)|_{\lambda_1}^{\lambda_2} = \sigma T_c^4 * (f(\lambda_2, T_c) - f(\lambda_1, T_c)) \left[\frac{W}{m^2} \cdot \mu m K \right] \quad (4.54)$$

$$e_{\lambda b}(T_w)|_{\lambda_1}^{\lambda_2} = \sigma T_w^4 * (f(\lambda_2, T_w) - f(\lambda_1, T_w)) \left[\frac{W}{m^2} \cdot \mu m K \right] \quad (4.55)$$

$$\frac{dq_{e_w}}{d\lambda} |_{\lambda_1}^{\lambda_2} = \dot{q}_{e_w} * (f(\lambda_2, T_{source}) - f(\lambda_1, T_{source})) \left[\frac{W}{m^2} \cdot \mu m K \right] \quad (4.56)$$

Thus, the incoming radiation per spectral band can be represented as the sum at each wavelength range analyzed, as presented in Table 4.9:

$$\dot{q}_c = \sum_{i=1}^3 q_{c\lambda_i} \left[\frac{W}{m^2} \right] \quad (4.57)$$

$$\dot{q}_w = \sum_{i=1}^3 q_{w\lambda_i} \left[\frac{W}{m^2} \right] \quad (4.58)$$

The temperature variations for each iteration can be determine as follows, similarly to Table 4.7, also applying $\Delta t = 3$ seconds for time discretization (forward Euler approximation), but now considering the receiver as a whole, i.e. wind skirt and cavity together:

$$\Delta T_s = \frac{1}{m_{s_{1+2}} * c_{p_s}} * \left[\sum_{i=1}^3 \dot{q}_{c\lambda_i} * A_{ap} - \dot{Q}_{k_{1+2}} \right] * \Delta t \text{ [K]} \quad (4.59)$$

$$\Delta T_f = \frac{1}{m_{f_{1+2}} * c_{p_f}} * \left[\sum_{i=1}^3 \dot{q}_{c\lambda_i} * A_{ap} - \dot{Q}_{(k+c)_{1+2}} \right] * \Delta t \text{ [K]} \quad (4.60)$$

This method follows the same criteria for steam generation presented for the cavity, i.e. cavity temperature must be 523 K (250 °C), and net heat (incident radiation minus thermal losses) must be positive.

The quartz window thermal model was implemented on MATLAB.

5. Results and Discussion

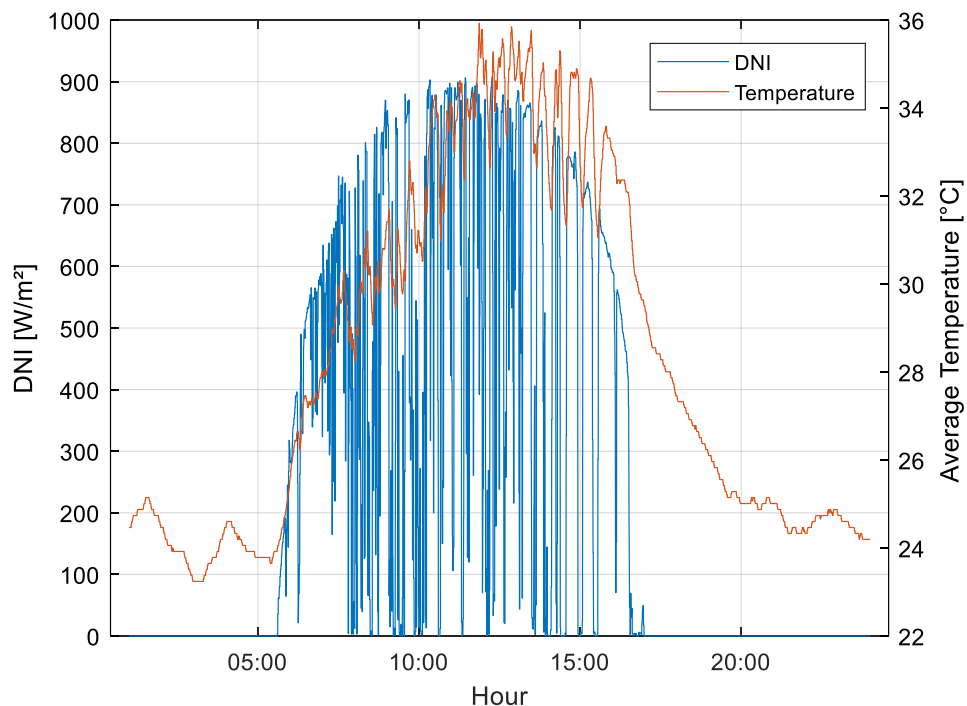
5.1. Meteorological Data

The date of May 16th, 2018, was the first available day with meteorological data measured *in situ*, hence being chosen to analyze the mathematical equations and simulation. Firstly, the meteorological data was reduced in order to remove non-possible values, applying those values in the simulation of components.

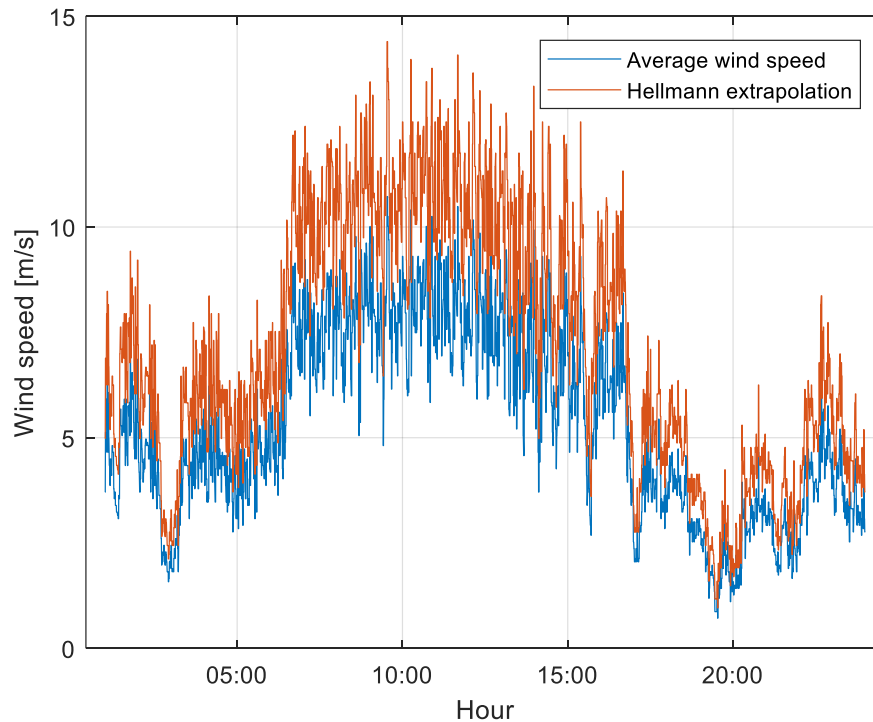
The data reduction was made on MS Excel. Figure 5.1 (a) shows the DNI and ambient temperature behavior over the day mentioned, as well as the wind speed at ground level (Figure 5.1. (b)), measured by the weather station, and the wind speed extrapolation (Hellmann exponential law) (BAUELOS-RUEDAS; ANGELES-CAMACHO; SEBASTIN, 2011) to be applied in a convection zone assessment explained in [Chapter 5.3.1.1](#). As can be seen, the DNI, ambient temperature, and wind speed present the same trend, increasing its values when the sun is up high, i.e. solar noon, decreasing when it is night.

Figure 5.1 – (a) DNI (blue) and Temperature (orange); and (b) wind speed at ground level (blue) and extrapolation (orange) variations throughout the day.

(a)



(b)



Source: The author.

Caiçara do Rio do Vento, due to its tropical location (near the Equator's line), has less inclined beams over the year reaching the surface when compared with higher latitude fields, like in Spain or USA, which means in theory smaller seasonal variations annually, as shown in Pereira et al. (2017).

Added to that, the location has relatively less air mass for the beams to pass through (KLEISSL, 2013), which can also explain the heliostats closer to the tower, as shown in the next item.

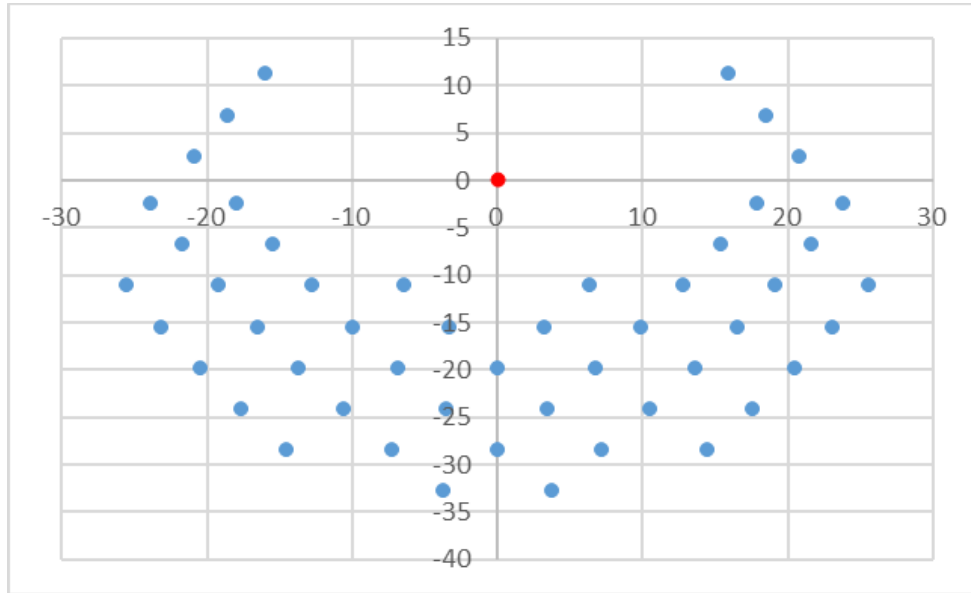
5.2. The Heliostat Field

Commonly, as presented in [Chapter 3.5](#), cavity receivers are used in polar fields. Brazil is mostly located in the Southern hemisphere, so the heliostat field will be north oriented, i.e. the heliostats are located in the south part of the plant facing/tracking the sun beam up to the tower, located in the northern part of the plant.

Nevertheless, as can be seen in Figure 5.2, where each blue dot represents one heliostat, and the red dot represents the tower/receiver pair, the optimum field layout is partially surrounding, i.e. some heliostats are in the northern part of the field

(first and fourth quadrants), due to the low latitude of the plant's location (5.71°S, 36.07° W).

Figure 5.2 – Heliostat's Cartesian positions (blue dots) in relation to the tower (red dot).



Source: DLR.

The solar field design point (sun in Zenith) efficiency η_{sf} [-] was calculated to be 0.795, with 58% of the power reaching Section 1 and 42% entering Section. The efficiency was also calculated based on the solar position throughout the day. Given the efficiencies obtained in Tonatiuh ([Appendix B](#)), it was possible to establish a relation through a two variable non-linear regression.

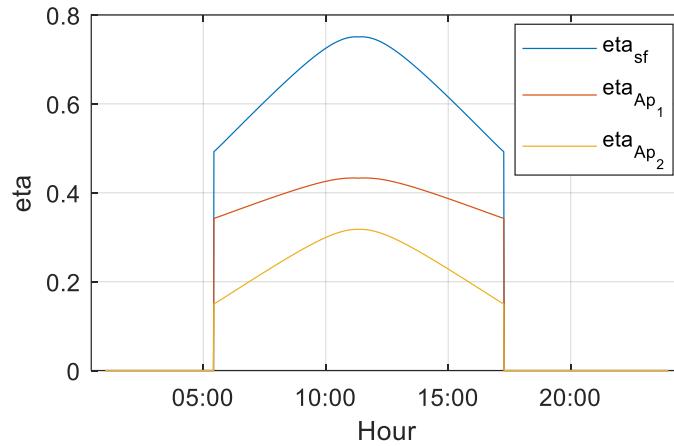
$$\eta_{sf} = 0.484 + 1.14 * 10^{-4} \gamma_{az} + 3.93 * 10^{-3} \varphi_{el} \quad [-] \quad (5.1)$$

$$\eta_{Ap_2} = 0.148 + 2.09 * 10^{-5} \gamma_{az} + 2.49 * 10^{-3} \varphi_{el} \quad [-] \quad (5.2)$$

$$\eta_{Ap_1} = \eta_{sf} - \eta_{Ap_2} \quad [-] \quad (5.3)$$

Figure 5.3 shows the total, as well as the Sections' efficiency for May 16th, 2018, as functions of the sun's position, i.e. azimuth and elevation angles.

Figure 5.3 – Total, Section 1, and Section 2 efficiencies for May 16th, 2018.



Source: The author.

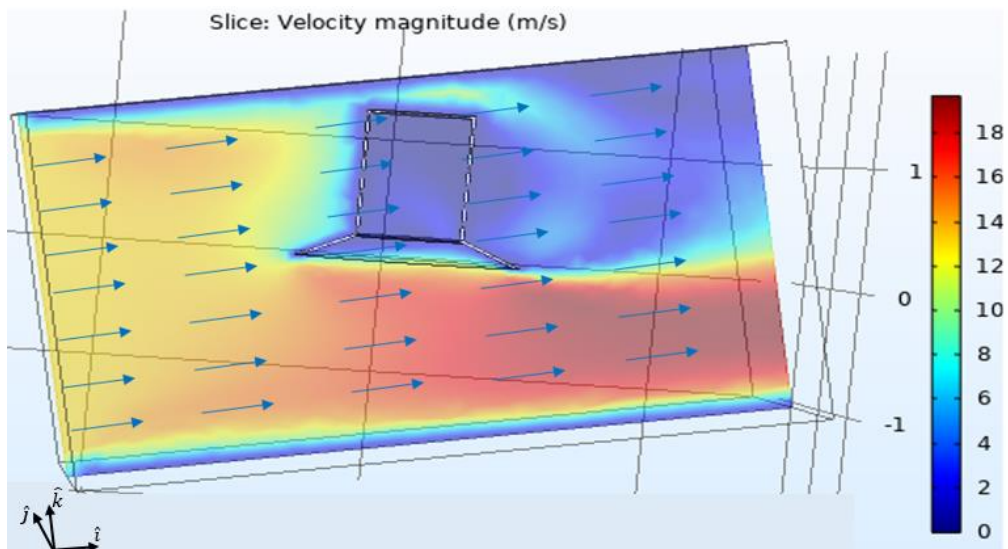
5.3. The Receiver

5.3.1. Thermal Model Results

5.3.1.1. Stagnation and Convective Zones

The stagnation and convective zones were assessed in COMSOL 5.4. Figure 5.4 shows a cross-section result obtained for a wind speed of 13 m/s (maximum reached in May 16th, 2018) entering orthogonally to the front plane (accounted on \hat{i} only). As can be seen, inside the cavity the velocity is almost zero everywhere, which means that exists a large stagnation zone, and a small area convective zone in the “brim”, represented in a bright green, coinciding with Figure 4.4 (b).

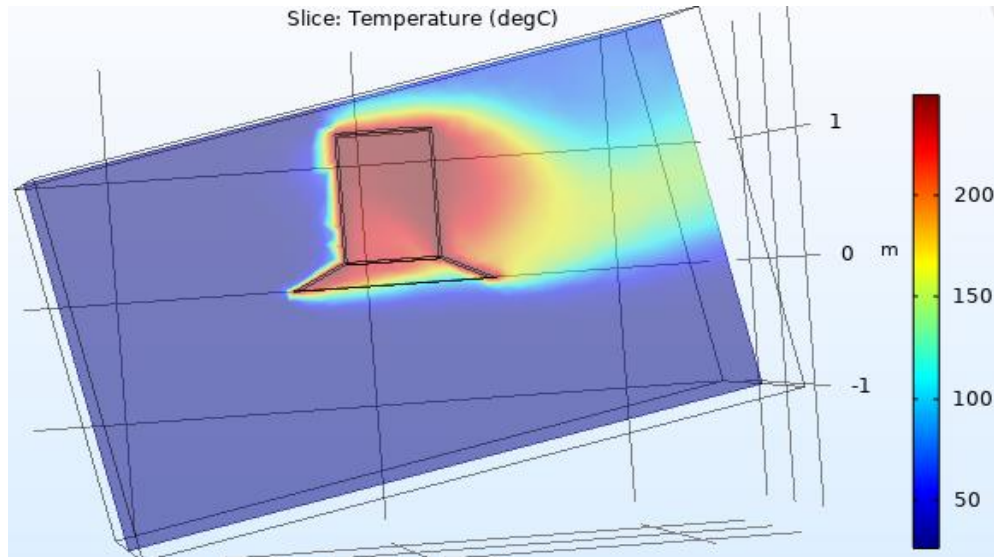
Figure 5.4 – COMSOL’s velocity profile, convective and stagnant zones within the receiver.



Source: The author.

Figure 5.5 shows the temperature profile within and outside the cavity in a cross-section snapshot from COMSOL, considering the receiver in steady state, i.e. 523 K (250 °C). The fluid temperature next to the receiver, as well as immediately behind it is approximately 250 °C, whereas around it, it resulted in ambient temperature ($T_{\infty} = 25$ °C).

Figure 5.5 – COMSOL’s temperature profile in the cavity.



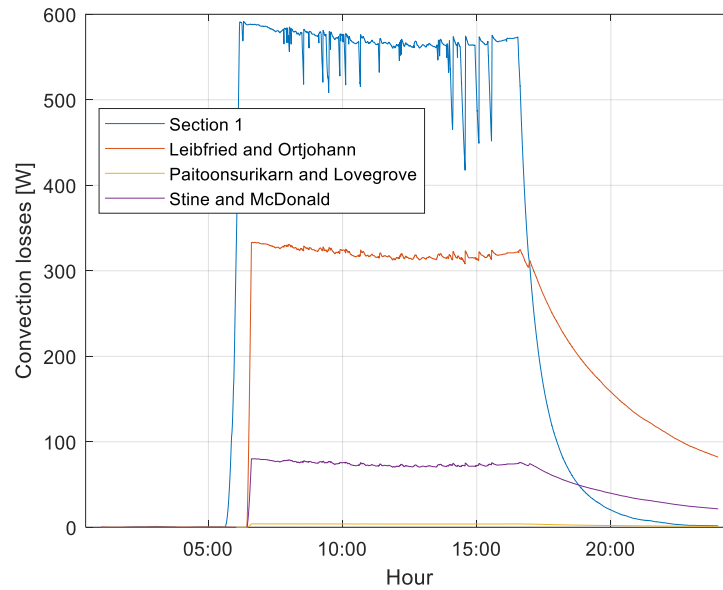
Source: The author.

This CFD validation was carried out in order to assess if the convection thermal losses methods implemented would culminate in tangible results.

5.3.1.2. Convection methodology

Figure 5.6 describes convection losses throughout the day. Section 1 presented the higher losses, followed by Stine & McDonald, Leibfried & Ortjohann, and finally Paitoonsurikarn & Lovegrove methods, the latter seeming to underestimate the losses. “S1” response do DNI variations is more sensitive than “S2”, which indicates the presence of a stagnation zone and quiescent convection thermal losses. Even though there is a significant discrepancy over the methodologies, convection losses are too small when compared with the others. “S1” was expected to present higher losses in comparison with “S2”, due to the direct contact with wind.

Figure 5.6 – Convective losses for both Sections.



Source: The author.

Since Leibfried & Ortjohann method presented intermediary results, it was chosen to calculate “S2” convective losses along the work. Nevertheless, validation through experimental analysis would help to assess which methodology fits better to the present case, as well as new convective loss correlation.

5.3.1.3. Model Results and Simulation

The thermal resistances ($1/R$) for the conduction and convection processes in the tube, foam, and to the environment, were calculated, and the heat transfer equations are presented ahead:

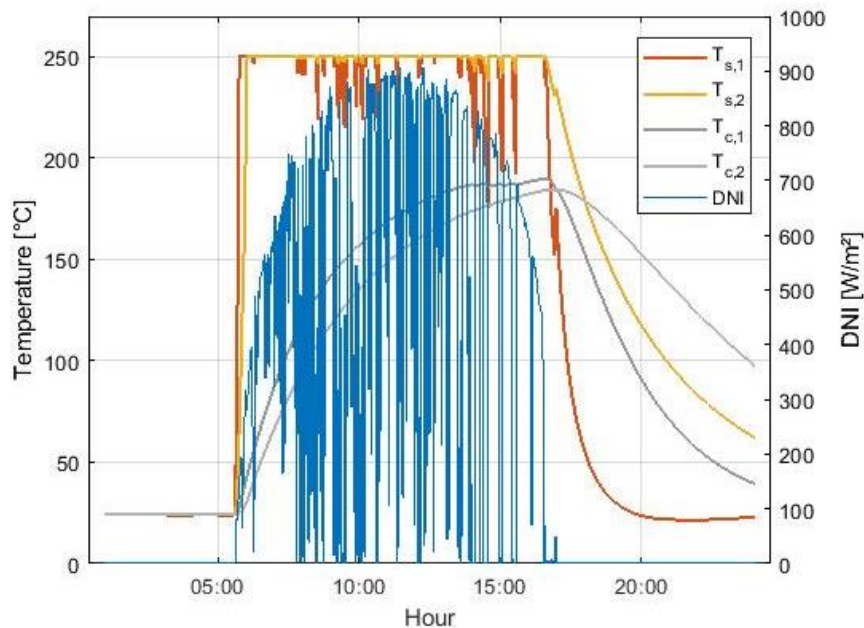
Table 5.1 – Thermal resistances applied in the model.

Section 1
$\dot{Q}_{k_1} = 0.843 * (\bar{T}_s - \bar{T}_c) \left[\frac{W}{K} \right]$
$\dot{Q}_{(k+cv)_1} = 0.229 * (\bar{T}_s^{t+1} - \bar{T}_c) \left[\frac{W}{K} \right]$
Section 2
$\dot{Q}_{k_2} = 1.382 * (\bar{T}_s - \bar{T}_c) \left[\frac{W}{K} \right]$
$\dot{Q}_{(k+cv)_2} = 0.376 * (\bar{T}_s^{t+1} - \bar{T}_c) \left[\frac{W}{K} \right]$

Source: The author.

Time discretization was performed through the forward Euler approximation, with $\Delta t = 3$ s sufficient for ensuring numerical stability. The steel tube (T_s) and ceramic foam (T_c) – henceforth always transformed from Kelvin to degrees Celsius – temperature behavior for both sections was calculated throughout the day, as presented graphically in Figure 5.7, which also shows the DNI. The steel temperature walks *pari passu* with the DNI, dropping abruptly with cloud passages. The operational temperature threshold of 250 °C can be easily seen, where the temperature is almost quiescent. Also, while $T_{s,1}$ take a shorter time to reach the operational temperature of 250 °C and thermal equilibrium in the evening, $T_{s,2}$ steel takes longer to reach the operational state, and ends the day with ca. 90 °C, due to its larger mass. Due to its characteristics, the foam temperature for both sections never reach steady state in the end of the day.

Figure 5.7 – DNI, steel and foam temperatures for Section 1 and Section 2.

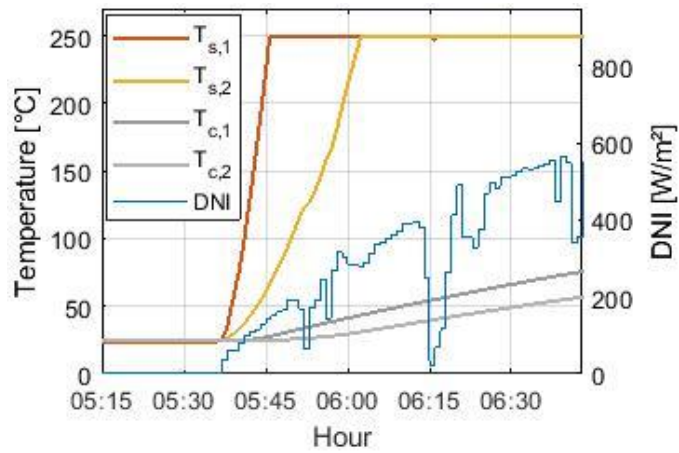


Source: The author.

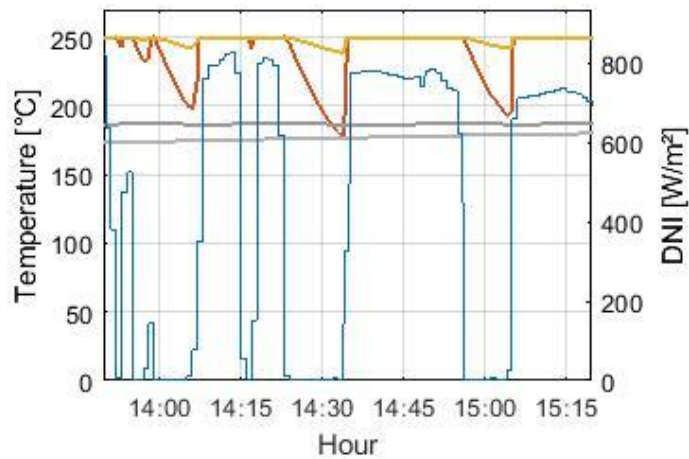
Figure 5.8 demonstrates the steel and ceramic temperature variations due to the transient nature of the DNI, showing the start-up, cloud passage, and shutdown phases. As can be noticed in Figure 5.8 (a), the operational temperature is reached ca. 0.3 h after sunrise for Section 1, due to lower mass, whereas takes almost 45 minutes for Section 2.

Figure 5.8 – DNI, “S1”, and “S2” temperature transient behavior on start-up (a), cloud passage (b), and shutdown (c).

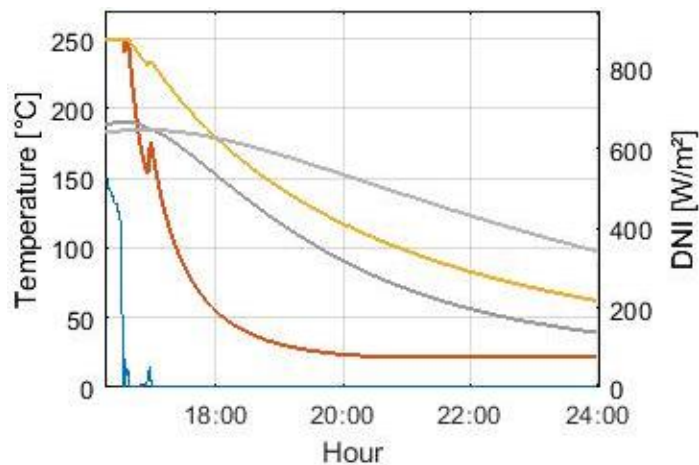
(a)



(b)



(c)



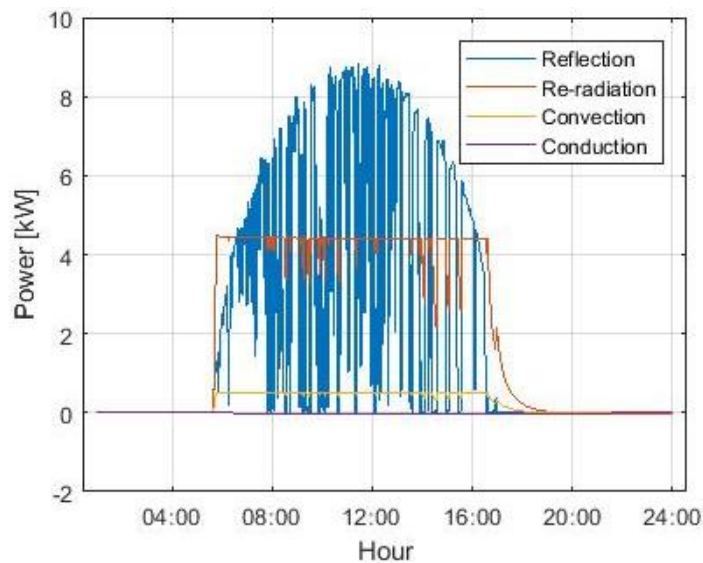
Source: The author.

Figure 5.8 (b) shows the intermittencies clearly, when a ca. 15 min cloud passage caused a sudden drop of DNI from 800 W/m² to zero and back, a significant

drop (ca. 25 up to 50 °C) is observed in Section 1, whereas the temperature of Section 2 remains practically constant. Finally, during shutdown, as shown in Figure 5.8 (c), a remaining temperature of 90 °C for Section 2 is observed at 24:00 h, 7 h after sunset, whereas Section 1 had reached thermal equilibrium. Due to its characteristics, the ceramic foam stays nearly flat in both sections throughout the day, as mentioned above.

Figure 5.9 shows reflection, convection, re-radiation, and conduction added to convection to the outer losses behavior for Section 1. As it can be notice, reflection losses are majority, followed by re-radiation (which follows closely DNI variations), and convective and conduction losses by far. When intermittences occur, thermal losses follow the same path, with conduction losses being negative, losing heat to the environment.

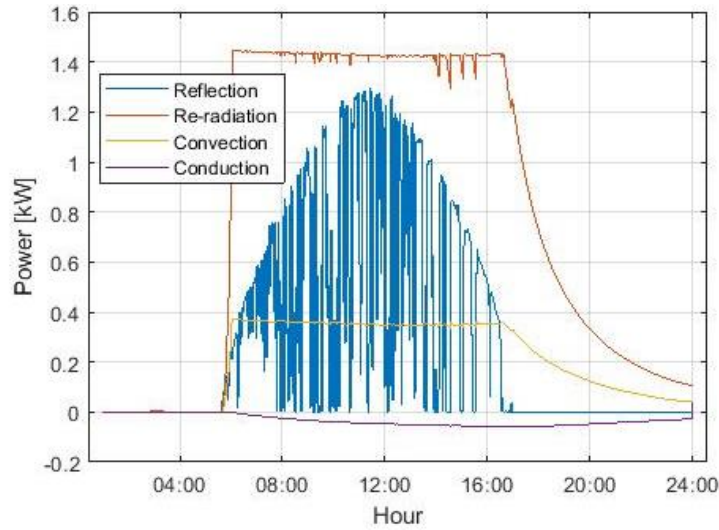
Figure 5.9 – “S1” reflection, convection, re-radiation losses, and conduction added to outer convection losses.



Source: The author.

However, Section 2 demonstrates a different pattern, as shown in Figure 5.10. In the cavity, re-radiation losses are predominant. This is due to the incident radiation that bounces around in the cavity, where the re-radiation happens at temperatures above of the surface that is transferring heat, as mentioned above, as well as for the low emissivity for the cavity itself (ϵ_{ap} is 0.99 for Section 1), so that almost all radiation that enters the cavity stays inside.

Figure 5.10 – “S2” reflection, convection, re-radiation losses, and conduction added to outer convection losses.

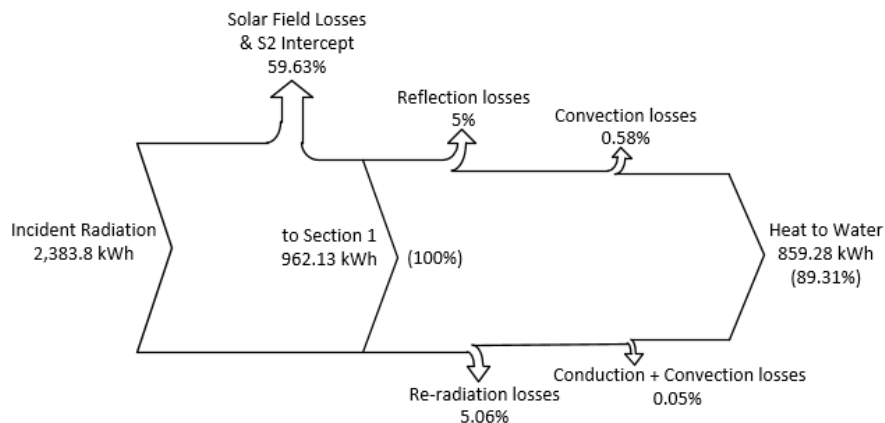


Source: The author.

These results are in agreement with data present in the literature. Ma (1993) reports that convective losses are low when the cavity is facing downwards, like this proposition, where those losses are negligible. Hinojosa et al. (2005) also comments that re-radiation losses are more significant than convective losses for large temperature differences (between 100 K and 400 K), such as this study, where the difference in temperature when the steel achieves 523.15 K (250 °C) is slightly above 200 K.

Figure 5.11 shows Section 1 energy flow through a Sankey diagram. As can be seen, 89.31% of the energy that reaches the receiver is transferred to the water, and re-radiation and reflection losses accounts as the highest thermal losses.

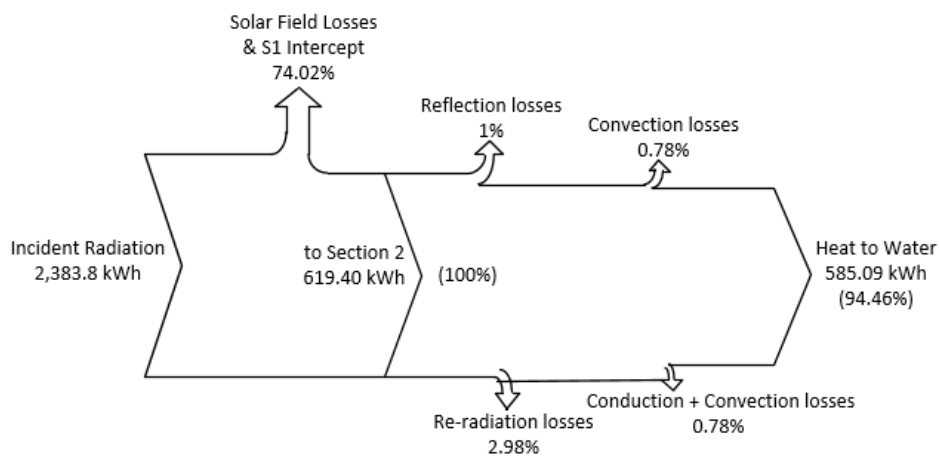
Figure 5.11 – Sankey diagram for Section 1.



Source: The author.

Following the same line, Figure 5.12 depicts the energy flow diagram for Section 2. Even though the energy that reaches Section 2 is smaller than Section 1 due to a smaller collecting area, its efficiency is higher. This reflects how well designed is the solar cavity for the desired operation. Reflection and re-radiation losses accounts the highest share, whereas convection and conduction losses are negligible, i.e. below 1%.

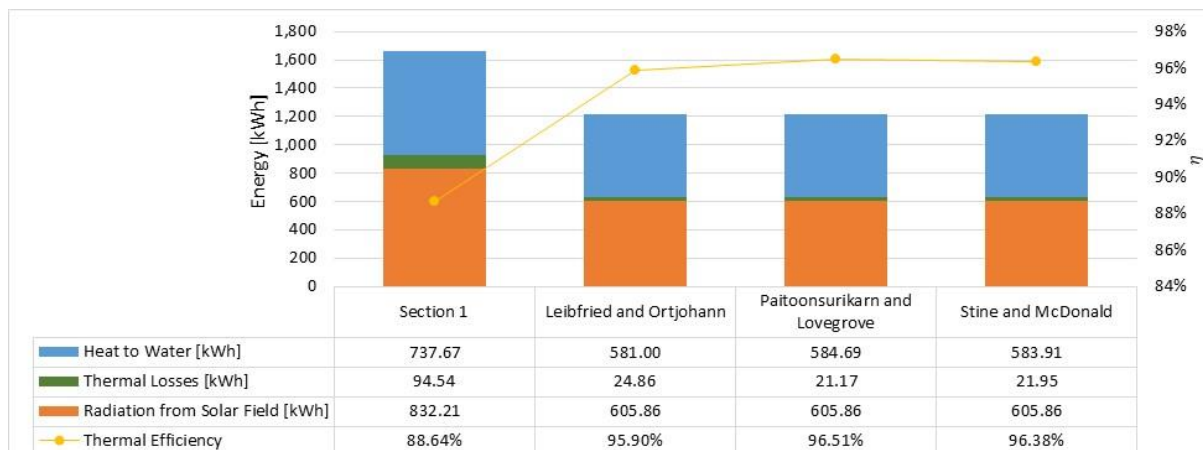
Figure 5.12 – Sankey diagram for Section 2.



Source: The author.

Figure 5.13 shows an energy comparative analysis for both sections and proposed method, as well as the thermal efficiency on the right axis. As can be seen, Section 1, as commented above, presented a lower thermal efficiency when compared with Section 2, in which thermal efficiency was similar for all methods.

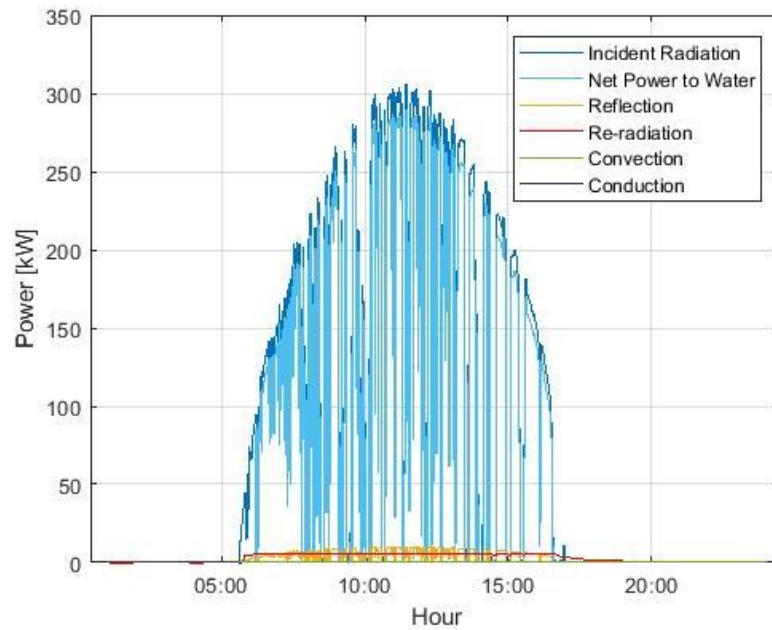
Figure 5.13 – Energy, thermal losses, and incident radiation from solar field for Sections 1 and 2, for May 16th, 2018.



Source: The author.

Nonetheless, is crucial to analyze the receiver as a whole, in order to assess its thermal efficiency. Considering both sections, thermal losses are extremely low when compared to the net heat transferred to the water, with re-radiation losses presenting the highest share, followed by reflection, as shown in Figure 5.14.

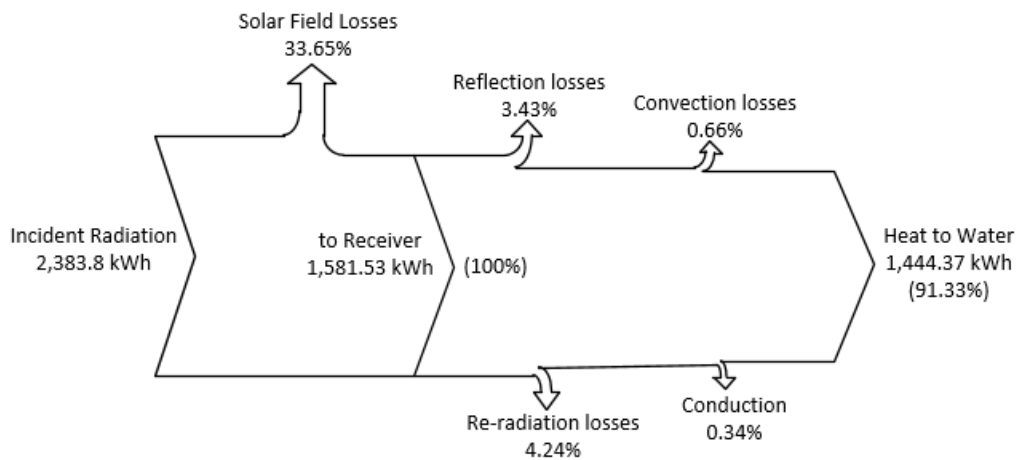
Figure 5.14 – Incident radiation, thermal losses, and net power transferred to the water.



Source: The author.

Figure 5.15 depicts the Sankey diagram for these thermal losses. The energy reaching the receiver is 1,581.53 kWh. The net heat transferred to water is 1,444.37 kWh, which also express the receiver efficiency, η_{rec} , of 91.33%.

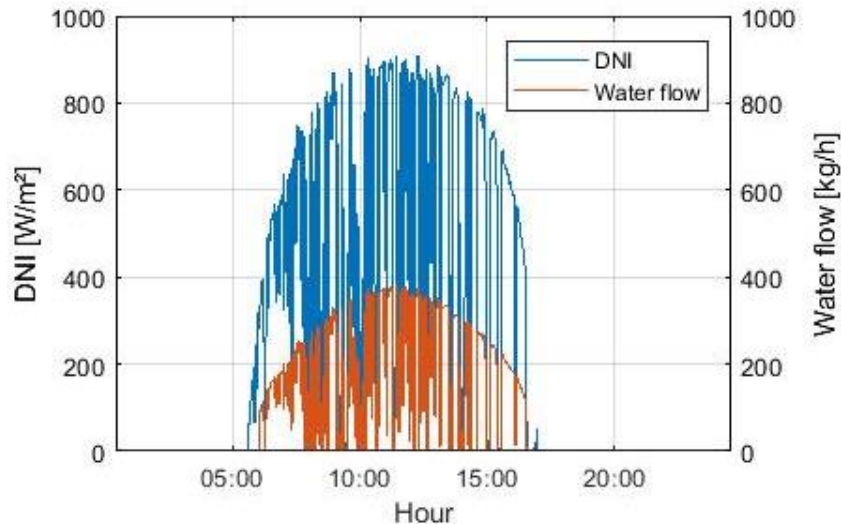
Figure 5.15 – Sankey diagram for the average thermal losses.



Source: The author.

Herewith, by applying the concept of net heat proposed in Eq. (4.32), it was possible to calculate the water mass flow throughout the day, as shown in Figure 5.16. The steam generation on May 16th, 2018, resulted in 1,898.93 kg.

Figure 5.16 – DNI and water mass flow pattern throughout the day.



Source: The author.

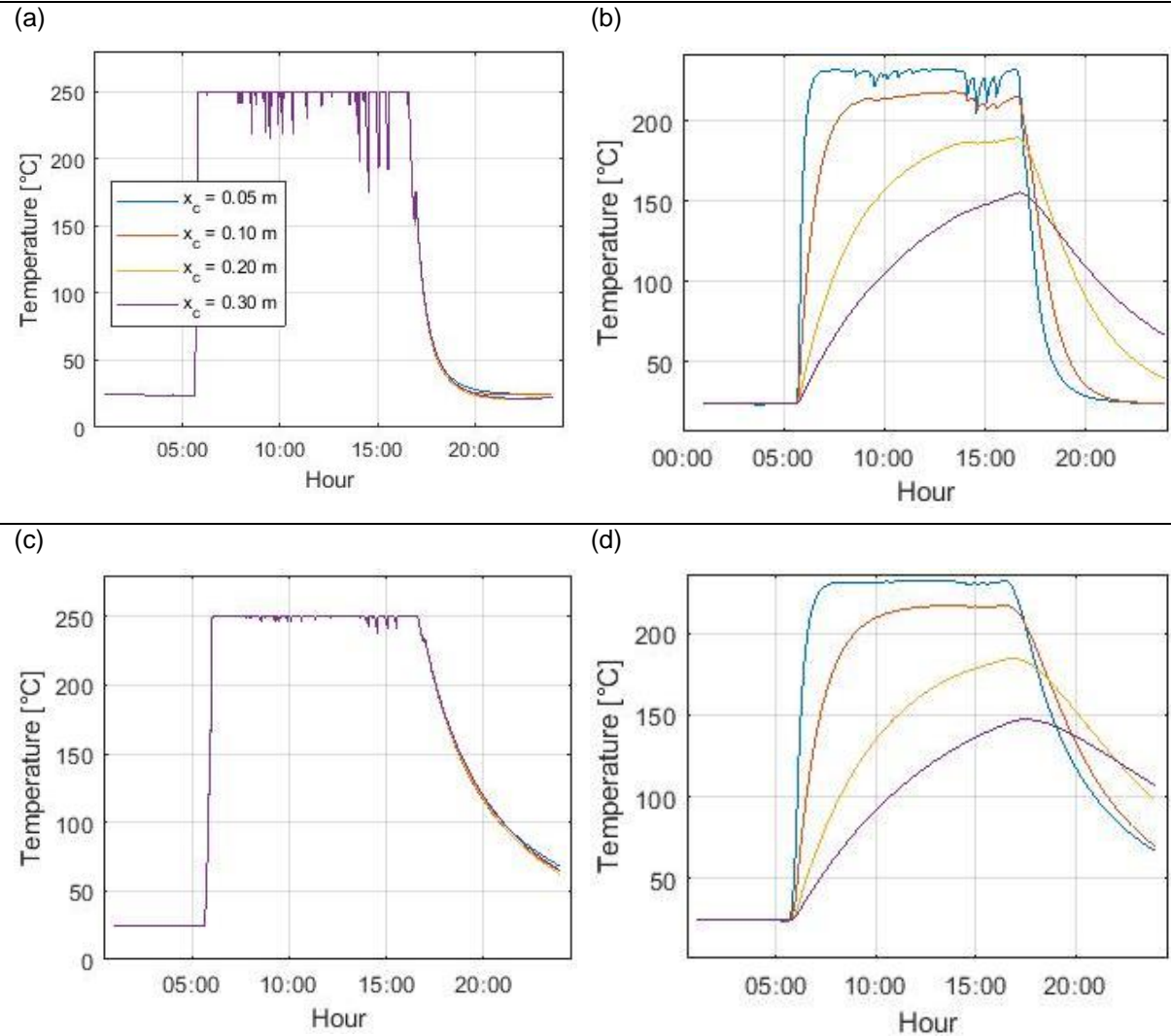
5.3.2. Ceramic Foam Sensitivity Analysis

The ceramic foam sensitivity analysis was carried in order to assess how the insulation length would affect the receiver's thermal losses, hence, the receiver's thermal efficiency.

Figure 5.17 depicts the steel and foam temperature behavior for Section 1 and Section 2. As can be seen, "S1" and "S2" steel temperatures present low sensitivity regarding the insulation length, with the curves almost overlapped for all periods: startup, cloud transients, and shutdown periods, again with a higher sensibility over intermittences. The smooth variations in "S2" can be explained by its higher thermal mass, as the results shown in [Chapter 5.3.1.3](#).

Nevertheless, the ceramic foam presents a high sensitive behavior for the different insulation dimensions. For smaller lengths, e.g. $x_c = 0.05$ m, it reaches *quasi* steady-state quicker, showing temperature variations as in Figure 5.17 (c), also declining to thermal equilibrium quicker, whereas larger insulation lengths have low sensitivity to intermittences, as in both cases for $x_c = 0.20$ and 0.30 m, where the system never reaches steady-state and thermal equilibrium in the shutdown.

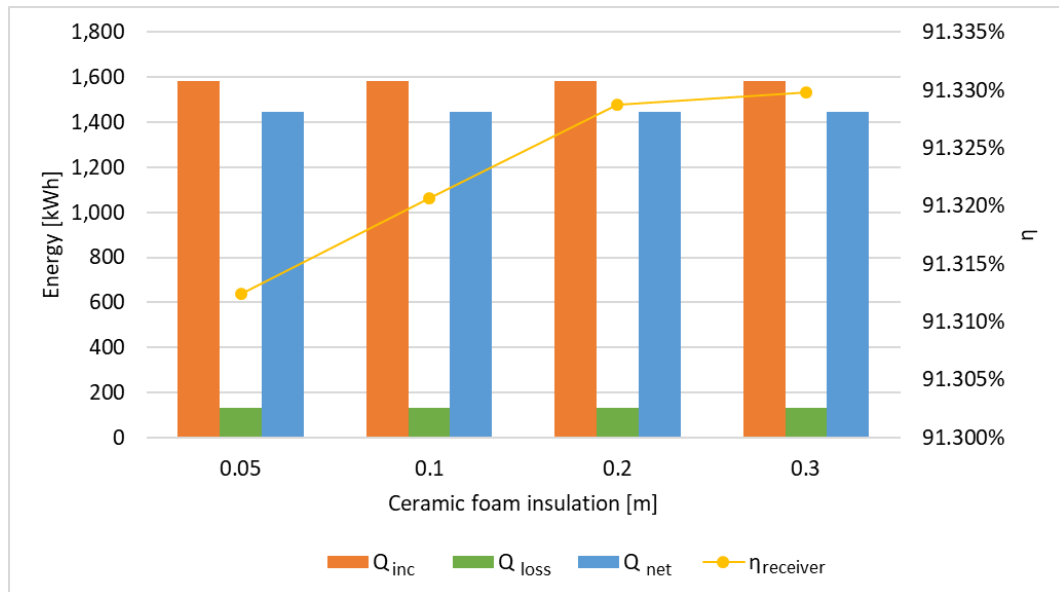
Figure 5.17 – Steel and ceramic foam temperatures, respectively, over the day for Section 1 (a) and (b), and Section 2, (c) and (d).



Source: The author.

Figure 5.18 demonstrates the energy over the day for the incident radiation, thermal losses, and net heat provided to water *versus* the efficiency as a response of the insulation variation. The energy presents a similar trend, like the efficiency, which changes little (only 0.017%). Even though thermal losses looks similar in magnitude, the efficiencies for larger insulation lengths are higher, due to less conduction and convection to the outside of the cavity losses.

Figure 5.18 – Incident radiation, thermal losses, net heat to water, and thermal efficiency regarding the insulation length.



Source: The author.

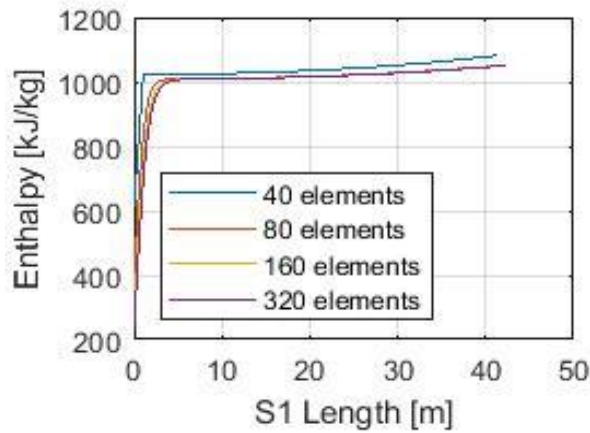
These quite similar efficiency results can be explained to the fact that in one hand, when the insulation is smaller e.g. 0.5 m, the system takes less time to reach operational state, whereas when the insulation is larger e.g. 0.30 m, the system has less thermal losses. Also, $x_c = 0.20$ m seems to be enough for the present application since its efficiency is quite close to $x_c = 0.30$, the highest.

5.3.3. Finite Volume Method

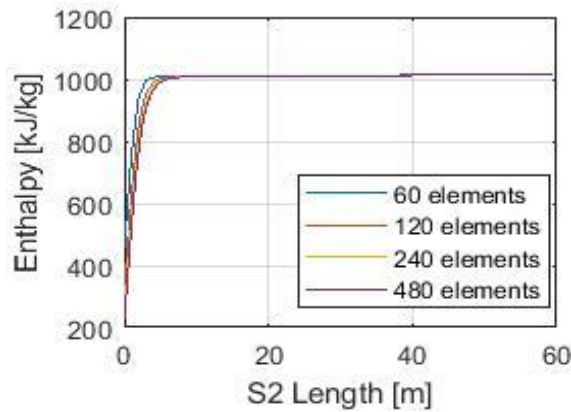
The Finite Volume Method was implemented to calculate the hydrodynamic effects within the tube, in order to reach a more reliable model. Firstly, the the number of elements was calculated, starting with ca. one element per meter regarding each Sections' length. Thus, "S1" started with 40 elements, "S2" with 60 elements, and "S3" with 20 elements, and quadruplicated. With the number of elements triplicated, the enthalpy was small enough to reach the selection criteria, as shown in Figure 5.19, ahead.

Figure 5.19 – Enthalpy criteria to select the number of elements for each Section.

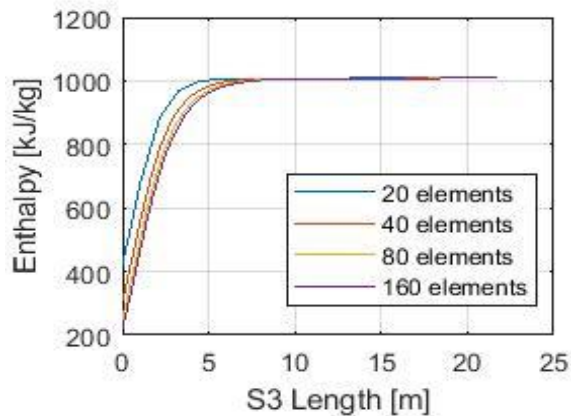
(a)



(b)



(c)



Source: The author.

Table 5.2 shows the pressure analysis results. The system had no convergence for 1.4 MPa (14 bar), where the pressure drop was too high. The steam outlet velocity for 2 MPa was too high for the expander, thus resulting in 2.5 MPa (25 bar) to be the most suitable pressure, used along the analysis.

Table 5.2 – Pressure analysis results.

Inlet pressure (MPa)	Outlet pressure (MPa)	Pressure Drop (MPa)	Outlet velocity (m/s)
2.0	0.566	1.434	57.92
2.5	1.671	0.829	18.62
3.0	2.354	0.646	13.13
3.5	2.967	0.533	10.35
4.0	3.544	0.456	8.63
4.5	4.099	0.401	7.43

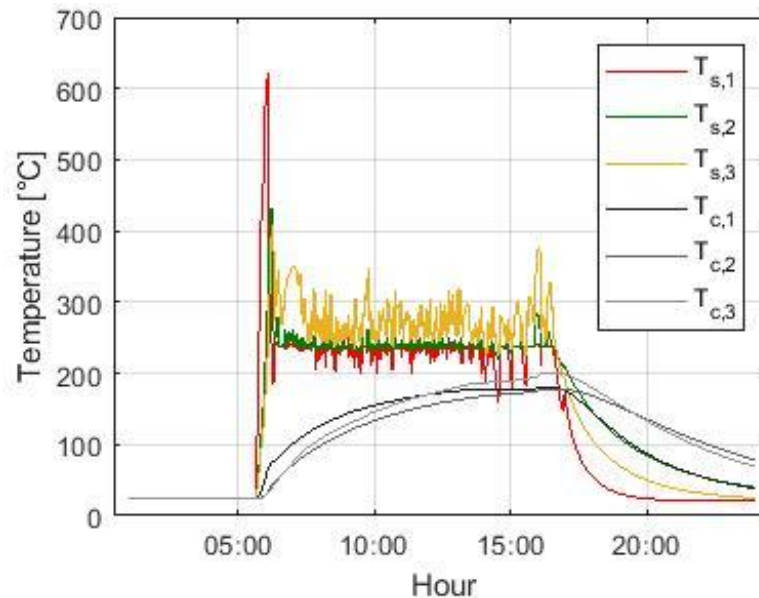
Source: The author.

Therefore, the reference temperature to be applied in the Bisection method is $T_{ref} = T_{sat}(p_{in}) + 10 \text{ K}$, or approximately 508 K (235 °C), for p_{in} of 2.5 MPa (25 bar), as abovementioned.

On issue found in the Bisection method implementation is that the method tends to go to the highest value of the mass flow range, thus resulting in an on/off operational stage, i.e. the steam generation is not constant. To solve this, the flow range for each time step was discretized accordingly to the incoming radiation.

The temperature results for the steel tubes and ceramic foam over May 16th, 2018, are depicted in Figure 5.20 ahead.

Figure 5.20 – Steel tube and ceramic foam temperature patterns for May 16th, 2018.



Source: The author.

As expected, the steel temperature follows closely the DNI pattern, as shown ahead. “S1” reaches a higher temperature when warming up due to low thermal mass, as previously mentioned. When the system starts, i.e. steel temperature for all Sections

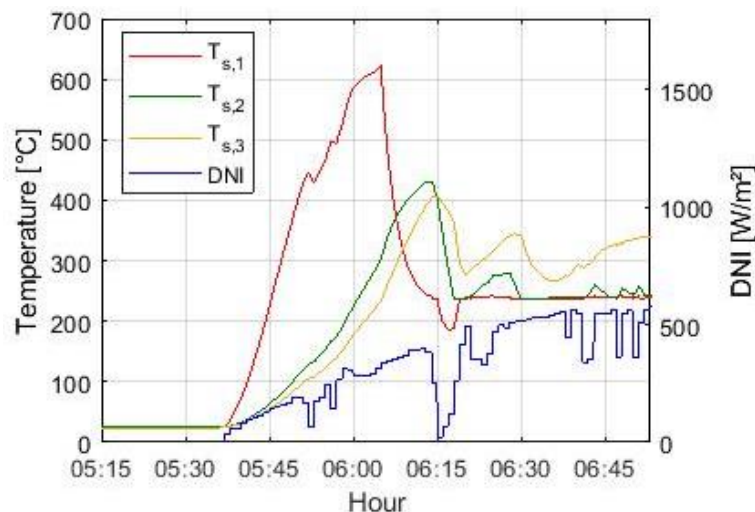
is above 225 °C, with water passing through the coils for steam generation, therefore reducing Section 1 steel temperature. As can be noticed, when compared to the previous model, the steel temperature reaches higher temperatures, especially in Section 3. Due to its characteristics, the foam temperature for the three sections never reach steady state, i.e. thermal equilibrium, in the end of the day.

Figure 5.21 details the steel temperature start-up, cloud passage, shutdown, and the DNI patterns over the assessed day. During start-up (Figure 5.21 (a)), $T_{s,1}$ reaches a 600 °C after ca. 20 minutes, decreasing to T_{ref} (235 °C) when operational phase started, i.e. all Sections reached T_{ref} . Here is important to notice that even though Section 2 has a larger mass than Section 3, $T_{s,2}$ reaches T_{ref} before than $T_{s,3}$, due to the irradiation discretization assumption, i.e. of all incoming radiation that reaches the cavity, 70% is directed to Section 2 (the lower part of the cavity) and 30% is directed to Section 3 (the cavity dome).

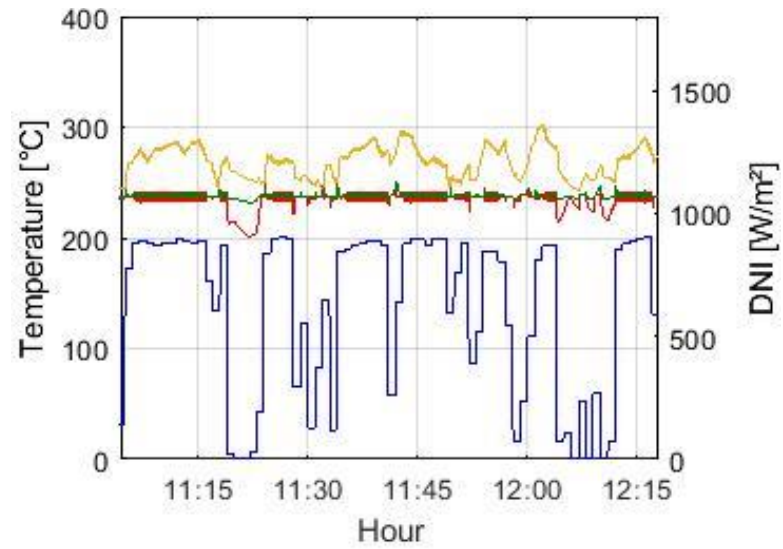
The transient aspect is shown in Figure 5.21 (b), where can it be observed over the cloud passage e.g. just after 11:15 A.M $T_{s,1}$ and $T_{s,3}$ temperature decreases due to low thermal mass, whereas $T_{s,3}$ continues almost flat. This influence can again be seen at shutdown, shown in Figure 5.22 (c), where $T_{s,1}$ reaches thermal equilibrium firstly, followed by $T_{s,3}$, whereas $T_{s,2}$ ends the day with ca. 40 °C. Here, even though Section 1 has a larger mass than Section 3, $T_{s,3}$ was higher than $T_{s,1}$, and this explains the time to reach thermal equilibrium.

Figure 5.21 – DNI, “S1”, “S2”, and “S3” steel tube temperature transient behavior on start-up (a), cloud passage (b), and shutdown (c).

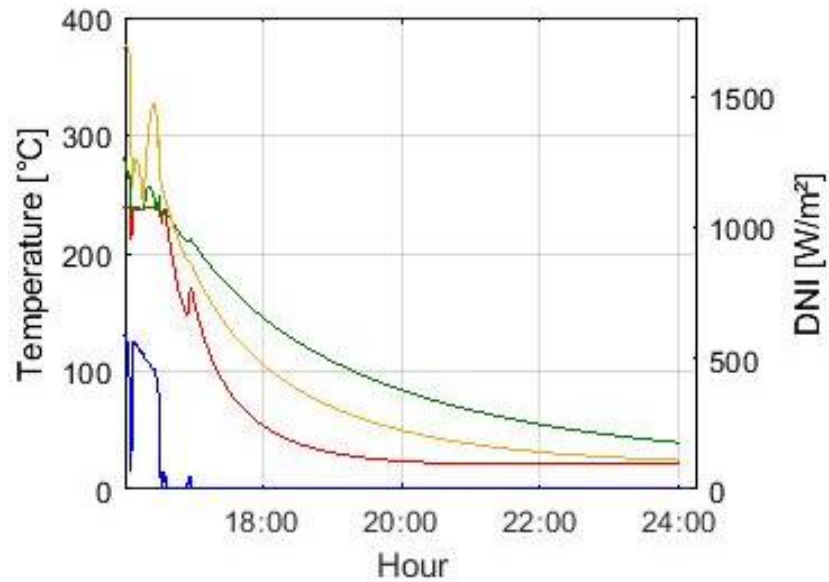
(a)



(b)



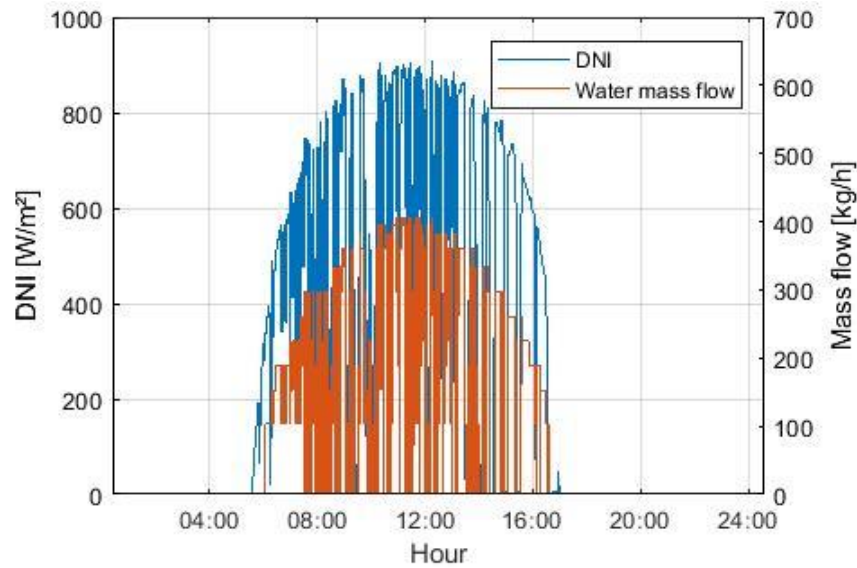
(c)



Source: The author.

Figure 5.22 shows the DNI pattern and water mass flow behavior for May 16th, 2018. The water mass flow follows closely the DNI variations throughout the day, as explained in the previous model. Nevertheless, with the Bisection model applied, the steam generation can be flattened more easily, reaching *quasi* steady-state in some small periods e.g. ca. 15 minutes.

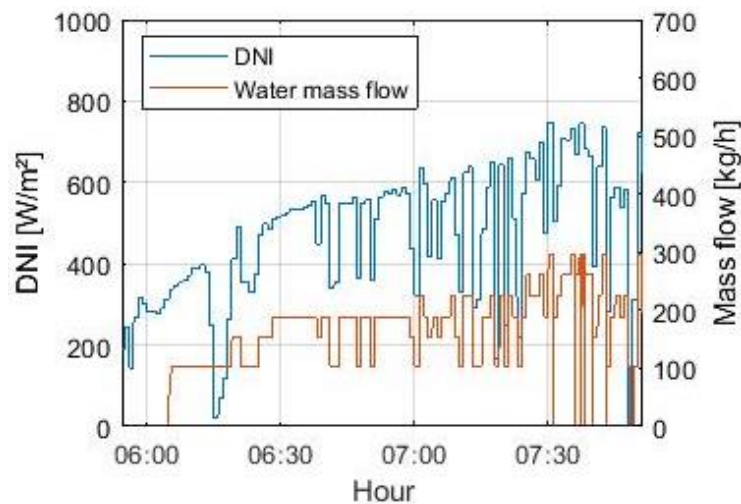
Figure 5.22 – DNI and water mass flow considering dynamic effects within the tube.



Source: The author.

This behavior can be specific seen in Figure 5.23, which also shows the DNI and mass flow behavior between 6:00 and 7:30 A.M. Here, when DNI increases, the flow also increases in order to maintain the steel temperature close to the reference temperature, and when DNI decreases to zero, the steel temperature decreases below the reference point, and the mass flow goes to zero.

Figure 5.23 – Detailed DNI vs water mass flow.



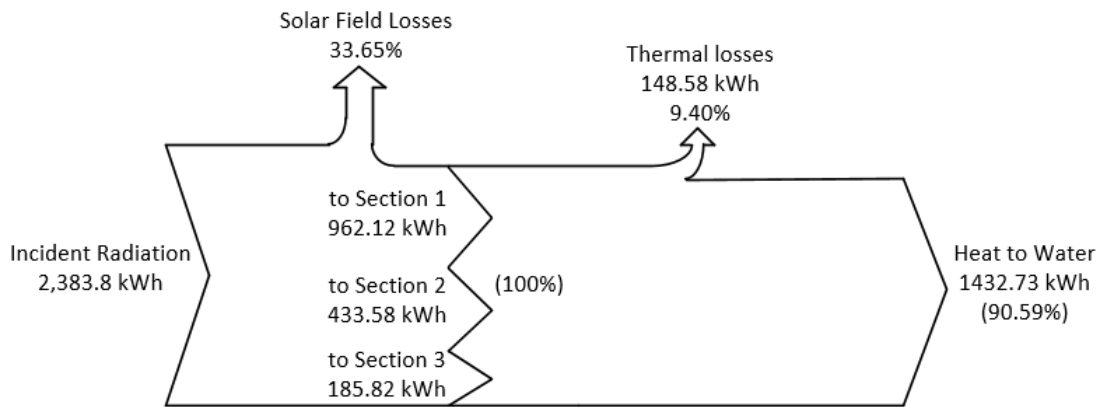
Source: The author.

The average pressure drop was 610 kPa (6.1 bar). Nevertheless, the outlet velocity was highly variable regarding the DNI, since it varies with the mass flow. So in this case, when DNI values are low (e.g. 500 W/m²), the mass flow is very low

(approximately 0.05 kg/s), and the outlet velocity is ca. 5 m/s, which is not suitable for the expander. For higher DNI values (e.g. 900, 1,000 W/m²), in another hand, the outlet velocity ranges from 10 to 15 m/s.

The Sankey diagram presented in Figure 5.24 shows the incident radiation incoming for each Section, as well as thermal losses, and heat to water. Considering the heat transferred to the water, and the dynamic effects within the tube, and considering small flows (below 0.5 kg/s), the system’s efficiency reduced from 91.33% from the previous model, to 90.59% in the present model, resulting in 1,883.54 kg of steam generation.

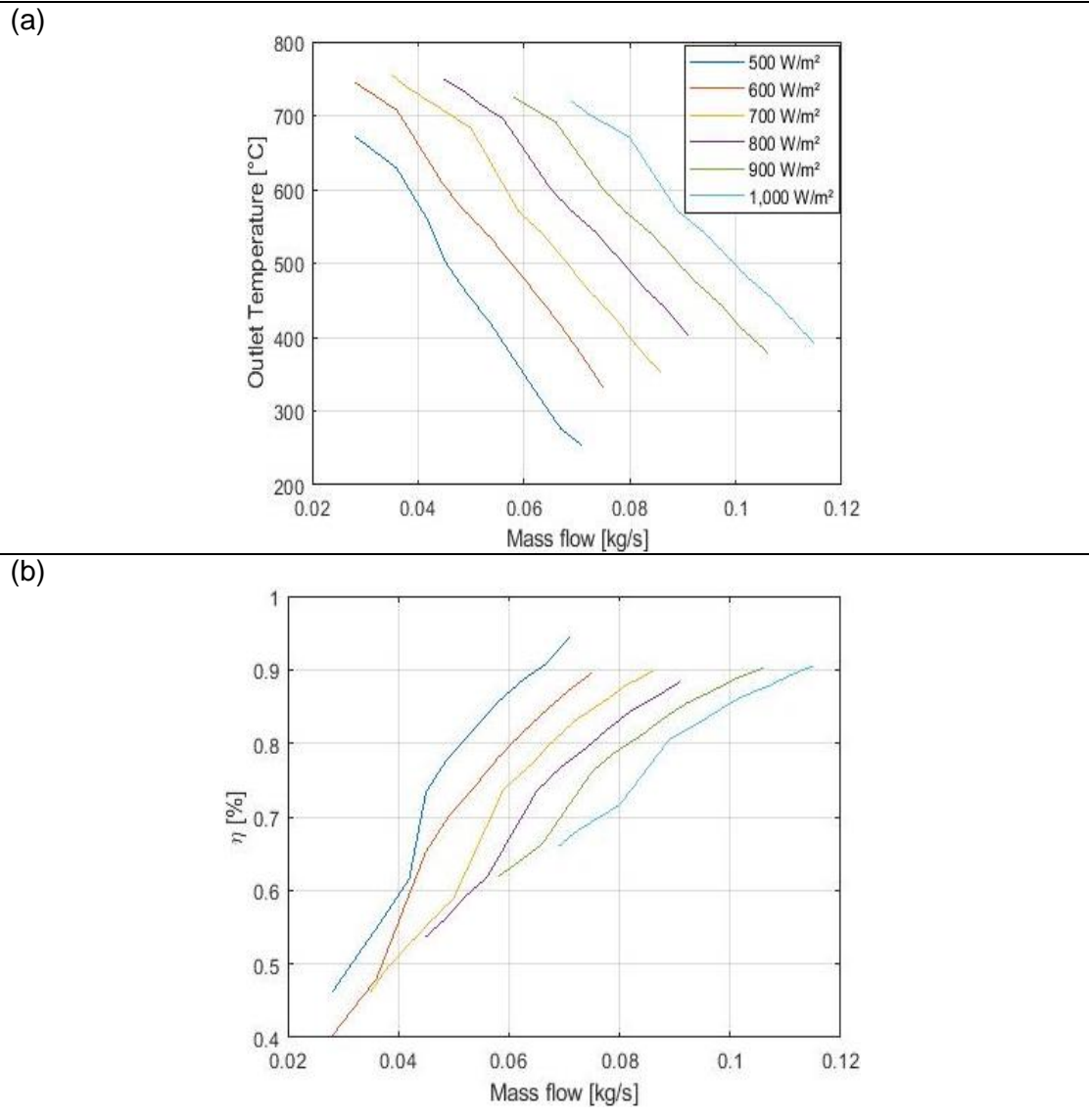
Figure 5.24 – Sankey diagram for May 16th, 2018, considering the dynamic effects within the tube.



Source: The author.

Figure 5.25 shows a steady-state analysis for the outlet steam temperature and receiver thermal efficiency as function of inlet water mass flow for different DNI values, considering design point efficiency, and the reference temperature. Outlet temperature increases with smaller mass flow, while thermal efficiency increases with higher mass flow, reaching maximum values where the inlet flow is close to the optimum value to reach the reference temperature. This analysis is helpful to reach maximum efficiency with variable flow and DNI values.

Figure 5.25 – Variation of steam outlet temperature (a) and thermal efficiency (b) as function of inlet water mass flow and DNI.



Source: The author.

5.3.4. Model Comparison

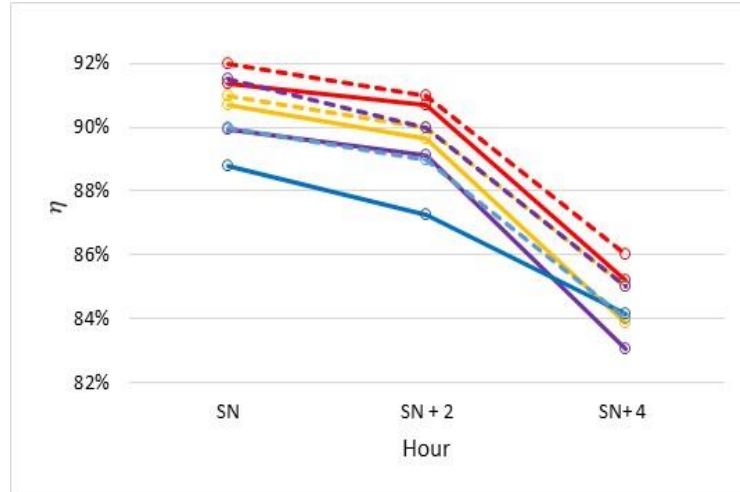
A results comparison of receiver efficiency and injected water mass flow between the ANU steady-state (“SS”) ANU SG4 and the USP transient (“T”) models is present ahead.

Figure 5.26 shows the results for the receiver efficiency on January 21st (a) and June 21st (c), as well as water inlet mass flow on the same days (b and d, respectively).

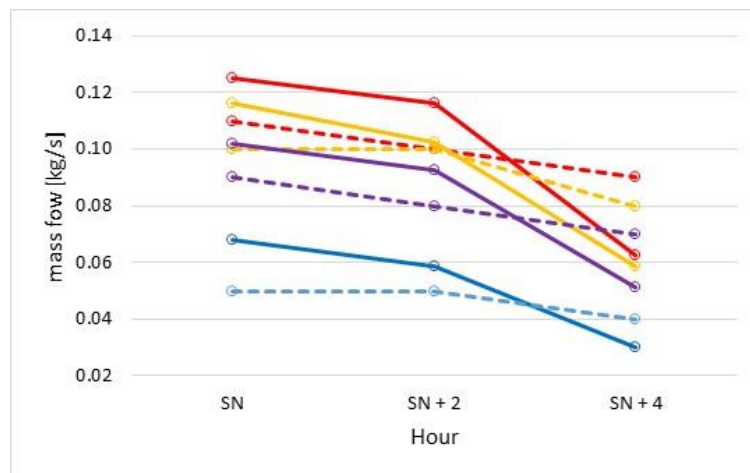
Figure 5.26 – “T” and “SS” comparisons for (a) thermal efficiency, and (b) water mass flow, for January and June 21st.

January 21st

(a)

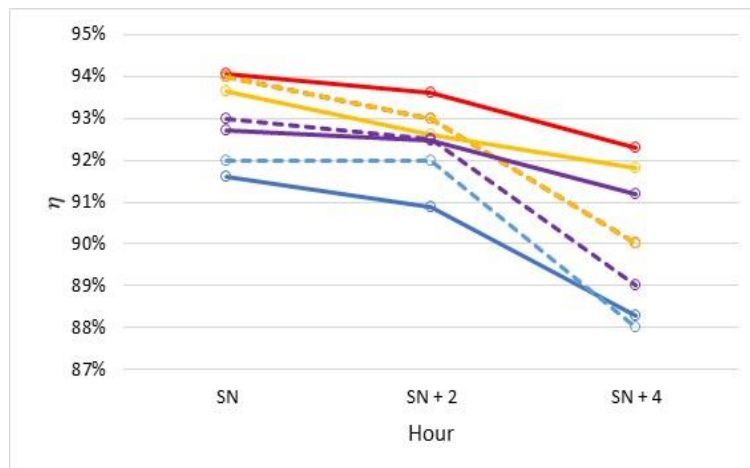


(b)

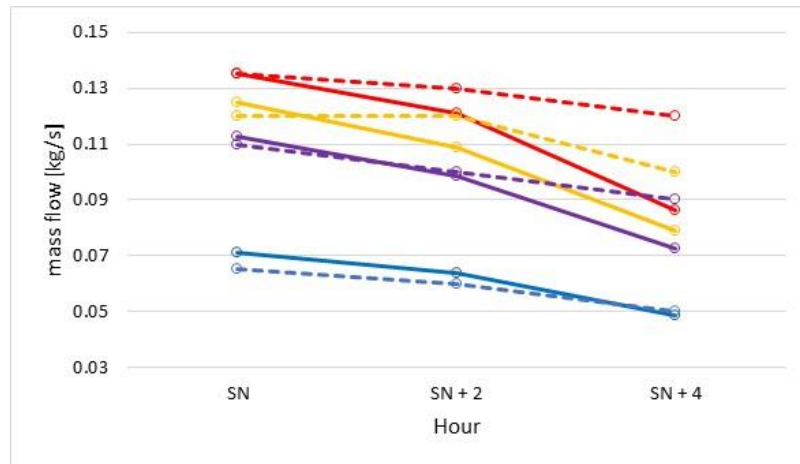


June 21st

(c)



(d)



—○— 1000 W/m² "T" - -○- - 1000 W/m² "SS" —○— 900 W/m² "T" - -○- - 900 W/m² "SS"
—○— 800 W/m² "T" - -○- - 800 W/m² "SS" —○— 500 W/m² "T" - -○- - 500 W/m² "SS"

Source: The author.

Comparison of receiver efficiencies and water mass flow shows a good agreement for both days for the majority of the results.

Approaching January 21st, thermal efficiency results are similar, except for low DNI values e.g. 500 W/m². Regarding the water mass flow, "T" models seems to overestimate it for SN and SN + 2, and underestimates it for SN + 4, especially regarding 1,000 W/m².

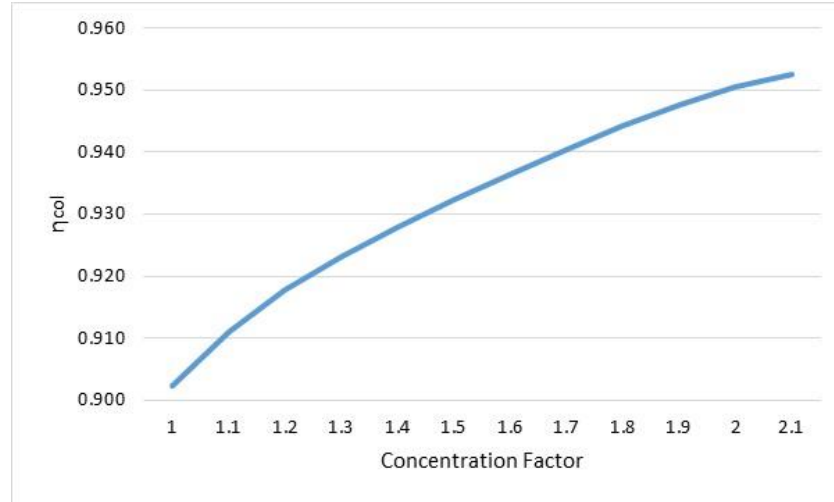
For June 21st, on the other hand, still regarding the water mass flow, "T" and "SS" have similar results except for SN + 4, where for higher DNI values the results have a discrepancy. Moving toward the thermal efficiency, "T" and "SS" values are also similar for SN and SN + 2, whereas for SN + 4 with higher DNI values the efficiencies present a larger discrepancy.

Even though some discrepancies between the results appeared, "T" model shows a good reliability, with realistic results.

5.4. The Compound Parabolic Receiver

The CPC-type results were calculated in MS Excel. The collecting efficiency as function of the concentration factor is shown in Figure 5.27. As expected, the collecting efficiency tends to increase as the concentration factor, i.e. CPC-type, increases, since more mirror area is added, hence, collecting more solar beams.

Figure 5.27 – Collecting efficiency as function of the Concentration Factor.



Source: The author.

With a curve fitting, a relation between the CPC aperture radius and the collection efficiency could be established, as follows:

$$\eta_{col} = -4.649 \cdot 10^{-15} r_{ap}^5 + 1.652 \cdot 10^{-11} r_{ap}^4 - 2.100 \cdot 10^{-8} r_{ap}^3 + 1.021 \cdot 10^{-5} r_{ap}^2 - 1.421 \cdot 10^{-4} r_{ap} \quad [-] \quad (5.4)$$

In the second step, approaching the CPC in the Caiçara system configuration, also via a curve fitting, was possible to establish a relation between the reflection efficiency ($\eta_{refl_{CPC}}$), as well as the solar beams that passed through the CPC, and the CPC Concentration Factor (C_{CPC} [-]), as follows:

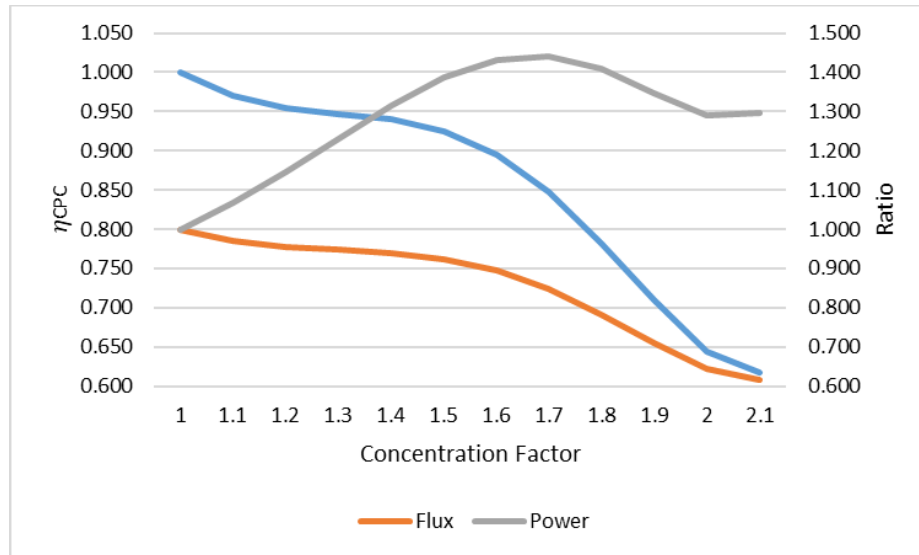
$$\eta_{refl_{CPC}} = 10.985 C_{CPC}^5 - 86.312 C_{CPC}^4 + 268.486 C_{CPC}^3 - 413.909 C_{CPC}^2 + 317.599 C_{CPC} - 96.847 \quad [-] \quad (5.5)$$

$$\eta_{through_{CPC}} = 2.598 C_{CPC}^5 - 18.393 C_{CPC}^4 + 50.681 C_{CPC}^3 - 68.274 C_{CPC}^2 + 45.120 C_{CPC} - 10.731 \quad [-] \quad (5.6)$$

Thus, the relation between η_{CPC} [-] and the above parameters can be determined, as in Eq. (4.45). The Figure 5.28 below shows the CPC efficiency, i.e. ratio between the power that leaves the CPC and the power that reaches the CPC, as function of Concentration Factor (ratio between the CPC radius and receiver radius), as well as the direct fraction of the CPC, i.e. ratio between output flux and input flux fraction. As we can observe, the efficiency decreases as the Concentration Factor

increases. The CPC has the feature of increasing the net power while decreasing the flux into the receiver.

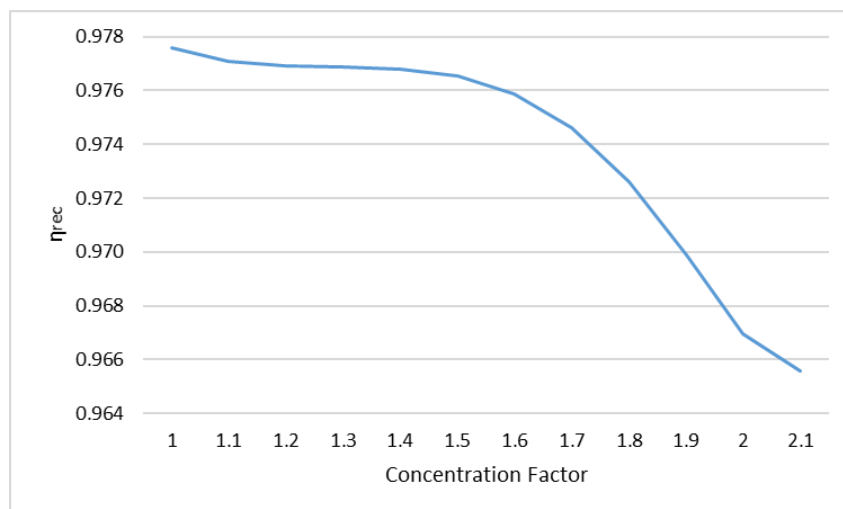
Figure 5.28 – CPC efficiency, flux and power ratios as functions of the Concentration Factor.



Source: The author.

In the next step, the relations presented in Eq. (4.45) and Eq. (4.46) could be expressed graphically. Figure 5.29 shows this relation between the cavity receiver efficiency (η_{rec} [-]) and the CPC Concentrating Factor, in terms of entering flux into the receiver (\dot{q}_{CPCout} [W/m²]). It is observed that the cavity receiver efficiency decreases with the increase in Concentrating Factor, since it has a direct relation with the flux, which decreases with the increasing Concentration Factor.

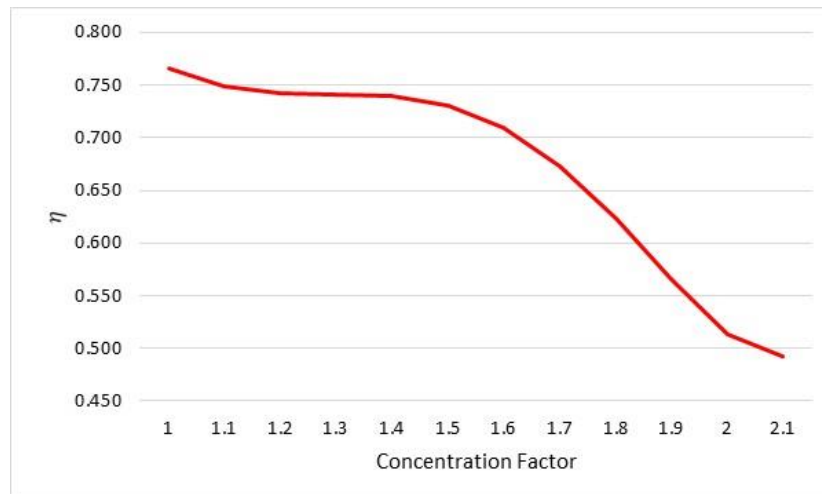
Figure 5.29 – Receiver efficiency as function of Concentration Factor.



Source: The author.

Lastly, by covering the efficiencies together, as presented in Eq. (4.49), the total efficiency (η [-]) could be determined as function of Concentrating Factor, as shown in Figure 5.30. As we can see, the total system efficiency decreases as the Concentrating Factor increases. The maximum efficiency is reached when Concentrating Factor equal to 1, demonstrating that the cavity receiver is already optimized for the Caiçara heliostat solar field, and the CPC wouldn't increase its efficiency if applied in the system. This can be explained by the incoming radiation from some heliostats (especially the farthest ones), which can have acute angles very close to the acceptance angle explained in [Chapter 3.2.2](#), where the radiation strikes the parabolic mirror, bounces around and goes off the CPC.

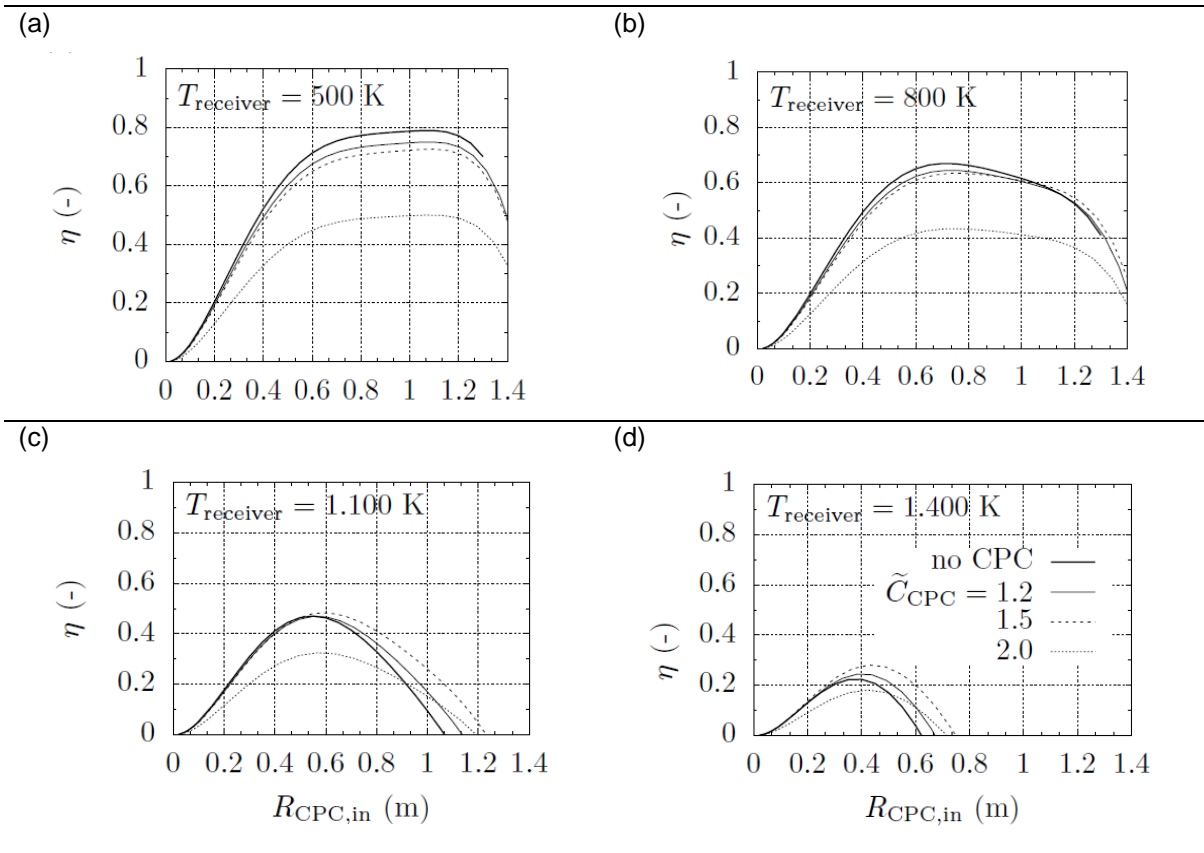
Figure 5.30 – Total efficiency as function of Concentrating Factor.



Source: The author.

Nevertheless, in this project, the cavity temperature is considered to be slightly above 500 K. For higher temperatures, with an increasing CPC radius, the CPC efficiency is higher than no CPC applied, like this case. Figure 5.31 shows this behavior graphically, where in Figure 5.31 (a) and (b), with temperatures of 500 K and 800 K, the efficiency with no CPC is higher, whereas in Figure 5.31 (c) and (d), with temperatures of 1100 K and 1400 K, the use of CPC starts to become advantageous. Another study carried by Segal & Epstein (1999) presented similar results, where a secondary concentrator is energetically reasonable when the working temperature is above circa 1,000 K or higher.

Figure 5.31 – CPC efficiency as function of temperature and CPC radius.



Source: Personal Communication.

5.5. The Quartz Window Receiver

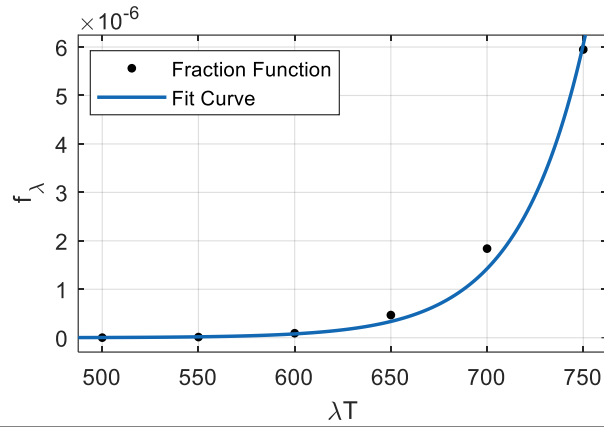
The quartz window was analyzed to select the wavelengths passing through the window, as well as to reduce losses (e.g. convective).

For the quartz window to the receiver cavity (F_{w-c}) is 1, and the view factor of the window to the window (F_{w-w} [-]) is 0, i.e. the radiation that enters the cavity stays inside. From Eq. (4.52), with a ration between window and cavity areas of 0.472, F_{c-w} [-] results in 0.472 as well. Hence, F_{c-c} [-] results in 0.528.

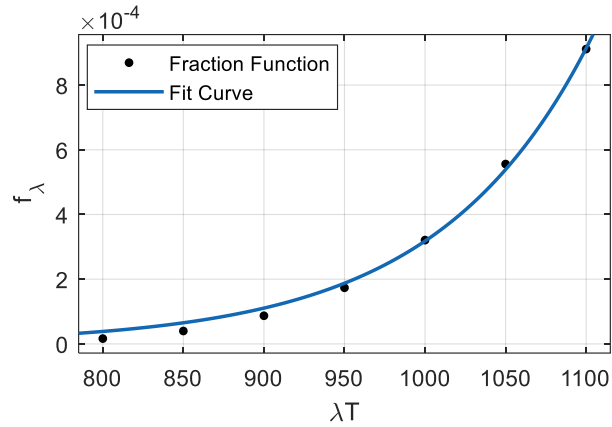
The window temperature was assumed to be 60% of cavity temperature for the iterations, and the source temperature is at 5,780 K, which are the temperatures considered to solve Eqs. (4.50) and (4.51). The fractional function was calculated in each time step through exponential and power approximations with tabulated data (STEINFELD; Z'GRAGGEN, 2010), ranging from 500 K to 1,600 K (i.e. operational temperature continues 250 °C, or 523.15 K, where $\lambda T|_{3\mu m}$ results in 1,569.45, since $\lambda T|_{\infty}$ equals to 1), as presented in Figure 5.32 (a), (b), and (c).

Figure 5.32 – Fractional function curve fitting.

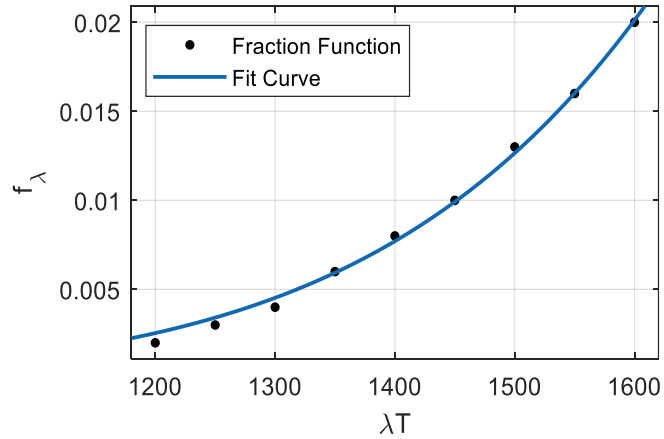
(a)



(b)



(c)



Source: The author.

Therefore, λT [$\mu\text{m.K}$] segmentations are presented ahead, whereas the equations for incoming radiation per wavelength interval, solving Eqs. (4.54) and (4.55), are depicted in [Appendix C](#).

- $\lambda T \leq 750 \cdot 10^{-6} \mu\text{m.K}$:

$$f_{\lambda} = 2.29 \cdot 10^{-15} * e^{0.02893 * \lambda T} \quad (5.7)$$

- $750 \cdot 10^{-6} \mu\text{m.K} < \lambda T \leq 1,100 \cdot 10^{-6} \mu\text{m.K}$:

$$f_{\lambda} = 8.26 \cdot 10^{-9} * e^{0.01056 * \lambda T} \quad (5.8)$$

- $1,100 \cdot 10^{-6} \mu\text{m.K} < \lambda T \leq 1,600 \cdot 10^{-6} \mu\text{m.K}$:

$$f_{\lambda} = 1.90 \cdot 10^{-25} * \lambda T^{7.185} \quad (5.9)$$

The incoming radiation on the window $\frac{dq_{e,w}}{d\lambda}$ for each wavelength interval is shown in Table 5.3. As can be noticed, the first and third intervals present no incoming radiation from the source.

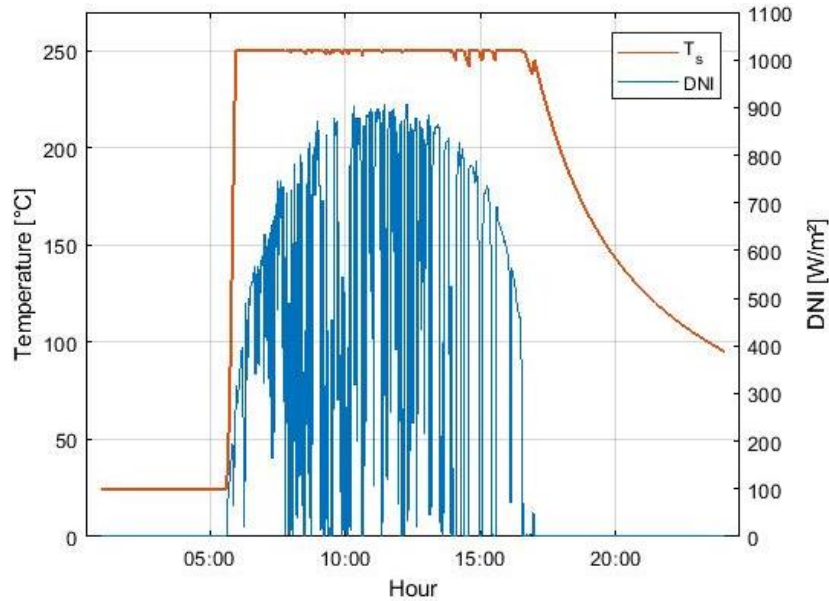
Table 5.3 – Incoming radiation on the window for each wavelength interval.

Wavelength	$\lambda T_{\text{source}}$ [$\mu\text{m.K}$]	f_{λ}	$\frac{dq_{e,w}}{d\lambda}$
$\lambda_1 = 0 \mu\text{m}$	0	0	
$\lambda_2 = 0.1 \mu\text{m}$	578	≈ 0	0
$\lambda_1 = 0.1 \mu\text{m}$	578	≈ 0	$\frac{\dot{Q}_{inc}}{A_{ap}}$
$\lambda_2 = 3 \mu\text{m}$	17,340	≈ 1	
$\lambda_1 = 3 \mu\text{m}$	17,340	≈ 1	
$\lambda_2 = \infty \mu\text{m}$	∞	1	0

Source: The author.

The temperature behavior for the steel tube as a comparison with DNI fluctuations is shown in Figure 5.33. The steel shows a quite similar pattern when compared to Section 2 for the cavity itself, with small sensibility for DNI variations throughout the day, since the masses from Section 1 and Section 2 are considered together on this analysis, i.e. large thermal mass. This influence can be again seen at the shutdown period, where the steel temperature never reaches thermal equilibrium at 24:00, ending the day at ca. 100 °C, similar trend to the cavity itself, again.

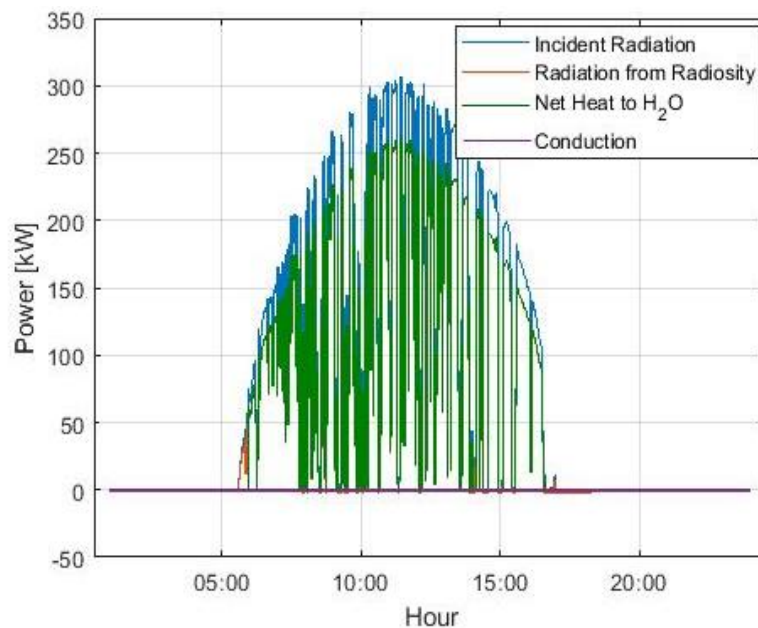
Figure 5.33 – DNI, steel and ceramic foam behaviors for May 16th, 2018, applying a quartz window.



Source: The author.

Figure 5.34 depicts the incident radiation incoming from solar field, the entering radiation in the cavity calculated through the radiosity method, the net heat transferred to water, and thermal losses through conduction and outer convection. Entering radiation and net heat are overlapped (similar values). Thermal losses in this case are also, as in the cavity itself, too small when compared to net heat.

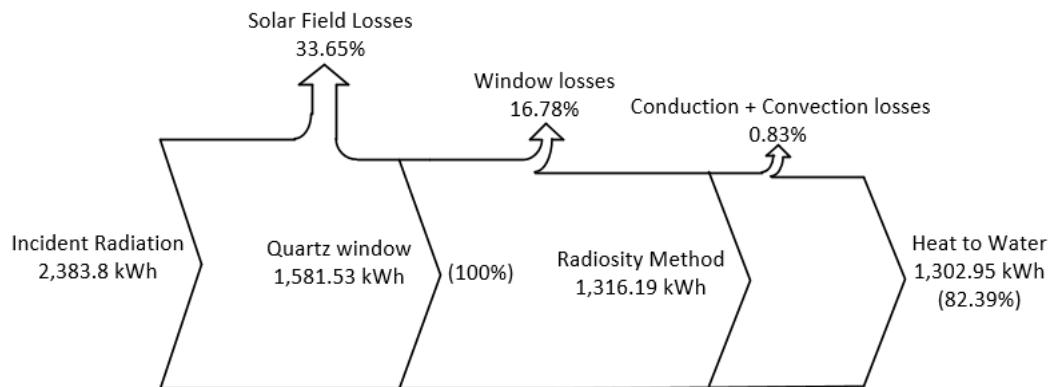
Figure 5.34 – Incident radiation from solar field, radiation from radiosity method, net heat transferred to water, and thermal losses.



Source: The author.

Figure 5.35 shows the energy flow through a Sankey diagram. The window losses are 16.78%, with 1,316.19 kWh of energy entering the cavity. Thermal losses by conduction and outer convection comprises less than 1% of the energy in the receiver, with 1,302.95 kWh transferred to the water by following the same criteria presented in [Chapter 4.5](#). Consequently, the receiver thermal efficiency with the quartz window applied is 82.39%, which is 8.94% lower than the cavity alone.

Figure 5.35 – Sankey diagram for the quartz window.

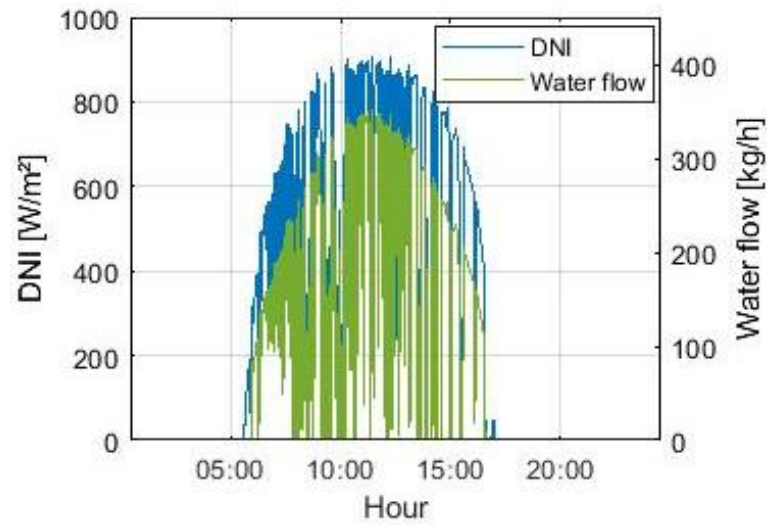


Source: The author.

Therefore, for the present case, i.e. lower temperature with an already designed cavity receiver, the quartz window would culminate in a poor improvement. These results are in accordance with data from Z'graggen & Steinfeld, (2004), where the insertion of a window has a negative effect on the absorption efficiency at lower temperatures, such as the analyzed case.

Figure 5.36 shows the water mass flow throughout the day. As can be noticed, the flow presents the same pattern as the net heat transferred to water, shown in Figure 5.34. The steam generation for May 16th, 2018, is 1,713.05 kg.

Figure 5.36 – DNI and water flow for May 16th, 2018, applying the quartz window.



Source: The author.

Two auxiliary (opaque and transparent) windows were also assessed as a way to validate the proposed model. Their results are on [Appendix D](#).

6. Conclusions

According to the proposed objectives, some conclusions can be taken. Firstly, it is expected that central receiver plant with cavity implemented in low latitudes, as the assessed case, to present a higher efficiency than central receiver plants in higher latitudes, as power plants worldwide.

The receiver's simulation reached reasonable, with trends similar to studies in the literature. On the other hand, the CPC-type and quartz window would not have been improvements to the system, since the results have shown lower efficiencies than the cavity itself, which demonstrating that the cavity is well designed.

The ceramic foam sensitivity analysis results presented a small thermal efficiency delta regarding the smallest insulation (0.05 m) and the largest insulation (0.30 m), with the proposed insulation (0.20 m) to be adequate for the receiver.

In order to achieve even more realistic results, a Finite Volume Method was implemented to assess the hydrodynamic conditions within the tube. The results demonstrated that the *a priori* inlet pressure of 1.4 MPa (14 bar) would be inapplicable, since the outlet steam velocity and pressure decay would be too high. Hence, the inlet pressure should be changed, as proposed, to 2.5 MPa (25 bar). Lastly, the receiver model attached to the tube model yielded realistic results, as could be noticed with the comparative analysis carried between the ANU "steady-state" and USP "transient" models, proving the latter's viability.

7. Future Work Recommendation

Further improvements and researches could be shaped. Firstly, the water mass flow ranges used in the Bisection Method could be meliorate, and consequently the steam generation could increase. Added to this, a physical analysis of the receiver must be carried, in order to validate the USP “transient” model, as well as to establish a Nusselt number correlation for the given receiver, which carries to more realist convection losses results.

References

- ABBASI-SHAVAZI, E.; HUGHES, G. O.; PYE, J. D. Investigation of heat loss from a solar cavity receiver. **Proceedings of the SolarPACES 2014 Conference**, v. 00, 2014. Available in: <<http://stg.anu.edu.au/publications/assets/inproc/abbasi-solarpaces-2014.pdf>>.
- ÁVILA-MARÍN, A. L. Volumetric receivers in Solar Thermal Power Plants with Central Receiver System technology: A review. **Solar Energy**, v. 85, n. 5, p. 891–910, May 2011. Available in: <<https://linkinghub.elsevier.com/retrieve/pii/S0038092X11000302>>.
- BAILEY, H. et al. **Distributed Generation and its Implications for the Utility Industry**. 1. ed. ISBN 978-0-12-800240-7. Elsevier, 2014.
- BAUELOS-RUEDAS, F.; ANGELES-CAMACHO, C.; SEBASTIN. Methodologies Used in the Extrapolation of Wind Speed Data at Different Heights and Its Impact in the Wind Energy Resource Assessment in a Region. **Wind Farm - Technical Regulations, Potential Estimation and Siting Assessment**, 2011. Available in: <<http://www.intechopen.com/books/wind-farm-technical-regulations-potential-estimation-and-siting-assessment/methodologies-used-in-the-extrapolation-of-wind-speed-data-at-different-heights-and-its-impact-in-th>>.
- BEHAR, O.; KHELLAF, A.; MOHAMMEDI, K. A review of studies on central receiver solar thermal power plants. **Renewable and Sustainable Energy Reviews**, v. 23, p. 12–39, 2013. Available in: <<http://dx.doi.org/10.1016/j.rser.2013.02.017>>.
- BEZERRA, Pedro Henrique Silva; SERAPHIM, Odivaldo José; OLIVEIRA, Celso Eduardo Lins de. PREVISÃO DE PERFORMANCE ENERGÉTICA POR MEIO DE SIMULAÇÃO TRANSIENTE DE UM SISTEMA CSP COM TORRE CENTRAL INTEGRADO A ATIVIDADES AGROINDUSTRIAIS. **Energia na Agricultura**, [s.l.], v. 33, n. 3, p. 264-269, 13 dez. 2018. EIA Energy in Agriculture. <http://dx.doi.org/10.17224/energagric.2018v33n3p264-269>.
- BLANCO, M. J.; SANTIGOSA, L. R. **Advances in Concentrating Solar Thermal Research and Technology**. 1. ed. Cambridge: Woodhead, 2017.
- BLAZEK, J. Temporal Discretization. In: BLAZEK, J. (Ed.). **Computational Fluid**

Dynamics: Principles and Applications. 3. ed. Oxford: Elsevier, 2015. p. 167–211.

BLÁZQUEZ, R.; CARBALLO, J.; SILVA, M. Optical design and optimization of parabolic dish solar concentrator with a cavity hybrid receiver. **AIP Conference Proceedings**, v. 1734, n. May, 2016.

CASTRO, G. M. **AVALIAÇÃO DO VALOR DA ENERGIA PROVENIENTE DE USINAS HELIOTÉRMICAS COM ARMAZENAMENTO NO ÂMBITO DO SISTEMA INTERLIGADO NACIONAL**. 2015. Universidade Federal do Rio de Janeiro, 2015.

ÇENGEL, Y. A.; BOLES, M. A. **Thermodynamics: An Engineering Approach**. 8. ed. New York: McGraw-Hill Education, 2015.

CLAUSING, A. M. An analysis of convective losses from cavity solar central receivers. **Solar Energy**, v. 27, n. 4, p. 295–300, 1981. Available in: <<http://www.sciencedirect.com/science/article/pii/0038092X81900621>>.

CLAUSING, A. M. Convective Losses From Cavity Solar Receivers - Comparisons Between Analytical Predictions and Experimental Results. **Journal of Solar Energy Engineering**, v. 105, n. 1, p. 29, 1983. Available in: <<http://solarenergyengineering.asmedigitalcollection.asme.org/article.aspx?articleid=1453985>>.

CLAUSING, A. M.; WALDVOGEL, J. M.; LISTER, L. D. Natural Convection From Isothermal Cubical Cavities With a Variety of Side-Facing Apertures. **Journal of Heat Transfer**, v. 109, n. 2, p. 407, 1987. Available in: <<http://heattransfer.asmedigitalcollection.asme.org/article.aspx?articleid=1439319>>.

CORGOZINHO, I. M.; HENRIQUE, J.; NETO, M. Modelo De Simulação De Uma Planta Solar-Elétrica Utilizando O Software Trnsys. In: V Congresso Brasileiro de Energia Solar, **Anais...**2014.

DELLICOMPAGNI, P. et al. Simulation and testing of a solar reciprocating steam engine. **Energy**, v. 151, p. 662–674, 2018. Available in: <<https://doi.org/10.1016/j.energy.2018.03.110>>.

DLR. **Volumetric receivers - heat conductors under extreme temperatures**. Available in: <https://www.dlr.de/sf/en/desktopdefault.aspx/tabid-10693/18599_read-43284/>. Access in: 16 Jan. 2019.

DUFFIE, J. a.; BECKMAN, W. a.; WOREK, W. M. **Solar Engineering of Thermal Processes**. 4. ed. New Jersey: John Wiley & Sons, 2013. v. 4

EPE. **Demanda de Energia 2050**. Rio de Janeiro: Ministério de Minas e Energia (MME), 2016.

EPE. **Balanço Energético Nacional 2018: Relatório Síntese - Ano Base 2017 / Empresa de Pesquisa Energética**. - Rio de Janeiro: EPE, 2018.

FANG, J. B. et al. Thermal performance simulation of a solar cavity receiver under windy conditions. **Solar Energy**, v. 85, n. 1, p. 126–138, 2011. Available in: <<http://dx.doi.org/10.1016/j.solener.2010.10.013>>.

FEDERAL FOREIGN OFFICE. **The German Energiewende** Berlin Federal Foreign Office, 2016. Available in: <<https://www.auswaertiges-amt.de/blob/610620/5d9bfec0ab35695b9db548d10c94e57d/the-german-energiewende-data.pdf>>.

FLESCH, R. et al. On the influence of wind on cavity receivers for solar power towers: An experimental analysis. **Applied Thermal Engineering**, v. 87, p. 724–735, 2015. Available in: <<http://dx.doi.org/10.1016/j.applthermaleng.2015.05.059>>.

FLESCH, R. et al. Reducing the convective losses of cavity receivers. **AIP Conference Proceedings**, v. 1734, n. May, 2016.

GARCIA, C. **Modelagem e Simulação de Processos Industriais e de Sistemas Eletromecânicos**. 1. ed. São Paulo: EDUSP, 1997.

GARCIA, M. E.; RAMOS, F. A.; CASTRO, T. L. C. de. **Guia de Licenciamento Ambiental de Heliotérmicas: Subsídios para Avaliação de Impacto Ambiental**. Available in: <http://energiaheliotermica.gov.br/pt-br/system/files/papers/2017_garcia_ramos_e_castro_guia_para_licenciamento_ambiental.pdf>.

GONZALEZ, M. M.; PALAFOX, J. H.; ESTRADA, C. A. Numerical study of heat transfer by natural convection and surface thermal radiation in an open cavity receiver. **Solar Energy**, v. 86, n. 4, p. 1118–1128, 2012.

GREEN. **Projeto Smile**. Available in: <<http://www.usp.br/green/smile.html>>. Access

in: 10 Jan. 2018.

HARRIS, J. A.; LENZ, T. G. Thermal Performance of Solar Concentrator/Cavity Receiver Systems. **Solar Energy**, v. 34, n. 2, p. 135–142, 1985.

HINOJOSA, J. F. et al. Numerical study of transient and steady-state natural convection and surface thermal radiation in a horizontal square open cavity. **Numerical Heat Transfer; Part A: Applications**, v. 48, n. 2, p. 179–196, 2005.

HINRICHS, R. A.; KLEINBACH, M. **Energia e Meio Ambiente**. 3. ed. New York: Thomson, 2003.

HO, C. K. et al. Characterization of Pyromark 2500 for High-Temperature Solar Receivers. **ASME 2012 6th International Conference on Energy Sustainability, Parts A and B**, v. 136, n. February 2014, p. 509, 2012. Available in: <<http://proceedings.asmedigitalcollection.asme.org/proceeding.aspx?doi=10.1115/ES2012-91374>>.

HO, C. K. Advances in central receivers for concentrating solar applications. **Solar Energy**, v. 152, p. 38–56, 2017. Available in: <<http://dx.doi.org/10.1016/j.solener.2017.03.048>>.

HO, C. K.; IVERSON, B. D. Review of high-temperature central receiver designs for concentrating solar power. **Renewable and Sustainable Energy Reviews**, v. 29, p. 835–846, 2014. Available in: <<http://dx.doi.org/10.1016/j.rser.2013.08.099>>.

HOFFSCHMIDT, B. Receivers for Solar Tower Systems. In: SFERA2, Font Romeu. **Anais...** Font Romeu: 2014. Available in: <[http://sfera2.sollab.eu/uploads/images/networking/SFERA SUMMER SCHOOL 2014 - PRESENTATIONS/SolarTowerReceivers - Bernhard Hoffschmidt.pdf](http://sfera2.sollab.eu/uploads/images/networking/SFERA_SUMMER_SCHOOL_2014_-_PRESENTATIONS/SolarTowerReceivers_-_Bernhard_Hoffschmidt.pdf)>. Access in: 11 Feb. 2019.

HORTA, P. **Process Heat Collectors: State of the Art and Available Medium Temperature Collectors**. Solar Heat & Cooling Programme. SHC Task 49. Solar Heat Integration in Industrial Processes. Technical Report A.1.3. Available in: <https://task49.iea-shc.org/Data/Sites/1/publications/Task%2049%20Deliverable%20A1.3_20160504.pdf>. Access in: 22 Apr. 2020.

IEA. **Chapter 1: Introduction and scope - World Energy Outlook 2017: World Energy Outlook**. OECD, 14 Nov. 2017. Available in: <https://www.iea.org/media/weowebiste/2017/Chap1_WEO2017.pdf>. Access in: 4 June 2019.

INCROPERA, F. P. et al. **Fundamentals of Heat and Mass Transfer**. 7. ed. Jefferson City: John Wiley & Sons, 2007.

KALOGIROU, S. **Solar energy engineering: processes and systems**. 1° ed. Oxford: Elsevier, 2009.

KARDITSAS, P. J.; BAPTISTE, M.-J. **Austenitic Stainless Steel (316)**. Available in: <<http://www-ferp.ucsd.edu/LIB/PROPS/PANOS/>>. Access in: 22 Jan. 2019.

KLEISSL, J. **Solar Energy Forecasting and Resource Assessment**. 1. ed. Oxford: Elsevier, 2013.

KOLB, G. J. et al. **Heliostat Cost Reduction Study ASME Energy Sustainability Conference**. Available in: <http://www.osti.gov/bridge/product.biblio.jsp?query_id=1&page=0&osti_id=912923>.

KUMAR, N. S.; REDDY, K. S. Numerical investigation of natural convection heat loss in modified cavity receiver for fuzzy focal solar dish concentrator. **Solar Energy**, v. 81, n. 7, p. 846–855, 2007.

LANGER, N. **SURVEY OF POTENTIAL HYBRIDISATION OPTIONS FOR CONCENTRATING SOLAR POWER PLANTS IN BRAZIL**. Brasília: Projeto Energia Heliotérmica, 2016. Available in: <http://energiaheliotermica.gov.br/pt-br/system/files/papers/2016_langer_survey_of_potential_hybridisation.pdf>. Access in: 2 July 2019.

LEE, K. L. et al. An investigation into the effect of aspect ratio on the heat loss from a solar cavity receiver. **Solar Energy**, v. 149, p. 20–31, 2017. Available in: <<http://dx.doi.org/10.1016/j.solener.2017.03.089>>.

LEIBFRIED, U.; ORTJOHANN, J. Convective Heat Loss from Upward and Downward-Facing Cavity Solar Receivers: Measurements and Calculations. **Journal of Solar Energy Engineering**, v. 117, n. 76, p. 10, 1995. Available in: <<http://solarenergyengineering.asmedigitalcollection.asme.org/article.aspx?articleid=>

1455456>.

LI, X. et al. Thermal model and thermodynamic performance of molten salt cavity receiver. **Renewable Energy**, v. 35, n. 5, p. 981–988, 2010. Available in: <<http://dx.doi.org/10.1016/j.renene.2009.11.017>>.

LIEDKE, P. et al. Precise low cost chain gears for heliostats. **AIP Conference Proceedings**, v. 1734, p. 0–7, 2016.

LODI, C. **Perpectivas para a Geração de Energia Elétrica no Brasil Utilizando a Tecnologia Solar Térmica Concentrada**. 2011. Universidade Federal do Rio de Janeiro, 2011. Available in: <<http://scholar.google.com/scholar?hl=en&btnG=Search&q=intitle:No+Title#0>>.

LOVEGROVE, K.; STEIN, W. **Concentrating solar power technology - Principles, developments and applications**. 1. ed. Oxford: Woodhead, 2012. v. 21

MA, R. Y. **Wind effects on convective heat loss from a cavity receiver for a parabolic concentrating solar collector**. Sandia Report Contract SAND92-7293. New Mexico, 1993.

MAAG, G.; FALTER, C.; STEINFELD, A. Temperature of a Quartz/Sapphire Window in a Solar Cavity-Receiver. **Journal of Solar Energy Engineering**, v. 133, n. 1, p. 4, 2011. Available in: <<http://solarenergyengineering.asmedigitalcollection.asme.org/article.aspx?articleid=1458019>>.

MAAG, G.; OLIVEIRA, K. T.; OLIVEIRA, C. E. L. **Hybrid Solar Tower Pilot Plants for Co-Generation of Heat and Power for Brazilian Agro-Industry**. In: Proceedings of ISES Solar World Congress 2015, November 2015, Daegu, South Korea.

MAGANHA, M. F. B. **Guia técnico ambiental da indústria de produtos lácteos**. Available in: <<https://cetesb.sp.gov.br/consumosustentavel/wp-content/uploads/sites/20/2013/11/laticinio.pdf>>. Access in: 24 jan. 2019.

MALAGUETA, D. C.; SZKLO, A. S.; DUTRA, R. M. **Análise Paramétrica De Uma Planta Csp-Iscs De Trigerção Para Um Hospital Em Bom Jesus Da Lapa**. In: V Congresso Brasileiro de Energia Solar, Recife. **Anais...** Recife: 2014.

MCDONALD, C. G. **Heat loss from an open cavity**. SANDIA REPORT CONTRACT SAND95-2939. New Mexico, 1995. Available in: <<https://www.osti.gov/servlets/purl/188598>>.

MEHOS, M. **Worldwide Deployment of CSP - Concentración Solar de Potencia, una Opción Clave para la Transición Energética**. Santiago, 2019. Available in: <https://www.fraunhofer.cl/content/dam/chile/es/documents/csetdocument/presentaciones/02-05-2019/190425 MMehos NREL.pdf?fbclid=IwAR3kSsT_b9bG4MdgpFrT-VKOqYOcuQuhuRo6mNw7XKWgEHILfm5-8FnGltU>. Access in: 3 May 2019.

NASCIMENTO, R. S. DO; ALVES, G. M. **Fontes alternativas e renováveis de energia no Brasil: Métodos e benefícios ambientais**. XX Encontro Latino Americano de Iniciação Científica, XVI Encontro Latino Americano de Pós-Graduação e VI Encontro de Iniciação à Docência, p. 1–6, 2016.

NREL. **Reference Air Mass 1.5 Spectra**. Available in: <<https://www.nrel.gov/grid/solar-resource/spectra-am1.5.html>>. Access in: 14 May 2019.

OLIVEIRA, A.; SALOMÃO, L. A. **Setor elétrico brasileiro: Estado e mercado**. Rio de Janeiro, RJ: Synergia Editora, 2017. ap. 6. (FGV energia). ISBN 978-85-68483-53-4.

PAITOONSURIKARN, S.; LOVEGROVE, K. **A new correlation for predicting the free convection loss from solar dish concentrating receivers**. Proceedings of the 44th Conference of the Australia and New Zealand Solar Energy Society (ANZSES), Canberra, Australia, n. 1989, p. 1–9, 2006.

PARENTE, R. **MODELO GENÉRICO PARA FINANCIAMENTO DE UMA USINA HELIOTÉRMICA APLICANDO LINHAS DE FINANCIAMENTO DISPONÍVEIS NO BRASIL: Sistema BNDES e BEB**. Available in: <http://energiaheliotermica.gov.br/pt-br/system/files/papers/2015_parente_modelo_generico_para_financiamento.pdf>.

PEREIRA, E. B. et al. **Atlas Brasileiro de Energia Solar**. 2. ed. São José dos Campos: TBN, 2017.

PFAHL, A. et al. Autonomous light-weight heliostat with rim drives. **Solar Energy**, v. 92, p. 230–240, 2013.

PLOTKIN, A. R. et al. **SOLAR RECEIVER STEAM GENERATOR DESIGN FOR THE IVANPAH SOLAR ELECTRIC GENERATING SYSTEM**. In: ASME 2011 Power Conference, Denver. Anais... Denver: 2011. Available in: <<http://proceedings.asmedigitalcollection.asme.org/>>.

PRAKASH, M.; KEDARE, S. B.; NAYAK, J. K. Investigations on heat losses from a solar cavity receiver. **Solar Energy**, v. 83, n. 2, p. 157–170, 2009. Available in: <<http://dx.doi.org/10.1016/j.solener.2008.07.011>>.

PRAKASH, M.; KEDARE, S. B.; NAYAK, J. K. Determination of stagnation and convective zones in a solar cavity receiver. **International Journal of Thermal Sciences**, v. 49, n. 4, p. 680–691, 2010. Available in: <<http://dx.doi.org/10.1016/j.ijthermalsci.2009.06.015>>.

PRINSLOO, G.; DOBSON, R. **SOLAR TRACKING: High precision solar position algorithms, programs, software and source-code for computing the solar vector, solar coordinates & sun angles in Microprocessor, PLC, Arduino, PIC and PC-based sun tracking devices or dynamic sun following hardware**. 1. ed. Stellenbosch: SolarBooks, 2015.

PYE, J. et al. Experimental testing of a high-flux cavity receiver. **AIP Conference Proceedings**, v. 1850, p. 9, 2017.

QIU, G.; LIU, H.; RIFFAT, S. Expanders for micro-CHP systems with organic Rankine cycle. **Applied Thermal Engineering**, v. 31, n. 16, p. 3301–3307, 2011. Available in: <<http://dx.doi.org/10.1016/j.applthermaleng.2011.06.008>>.

RABL, A. **Active Solar Collectors and Their Applications**. 1. ed. Oxford: Oxford University Press, 1985.

RAGHEB, M. **Solar Thermal Power and Energy Storage**, 2014. Available in: <http://www.solarthermalworld.org/sites/gstec/files/story/2015-04-18/solar_thermal_power_and_energy_storage_historical_perspective.pdf>.

REINER, B. et al. **TOWER CSP TECHNOLOGY: STATE OF THE ART AND MARKET OVERVIEW**. Available in: <http://energiaheliotermica.gov.br/pt-br/system/files/papers/2014_buck_tower_csp_techology_0.pdf>. Access in: 15 Jan. 2018.

REN21. **RENEWABLES 2017: GLOBAL STATUS REPORT**Global Status Report.

Available in: <[http://www.ren21.net/wp-content/uploads/2017/06/17-](http://www.ren21.net/wp-content/uploads/2017/06/17-8399_GSR_2017_Full_Report_0621_Opt.pdf)

[8399_GSR_2017_Full_Report_0621_Opt.pdf](http://dx.doi.org/10.1016/j.rser.2016.10.049)><<http://dx.doi.org/10.1016/j.rser.2016.10.049>><<http://www.ren21.net/status-of-renewables/global-status-report/>>.

<<http://www.ren21.net/status-of-renewables/global-status-report/>>.

Access in: 4 June 2019.

REN21. **Renewables 2018 Global Status Report**Global Status Report. [s.l: s.n.].

Available in: <[http://www.ren21.net/wp-content/uploads/2018/06/17-](http://www.ren21.net/wp-content/uploads/2018/06/17-8652_GSR2018_FullReport_web_final_.pdf)

[8652_GSR2018_FullReport_web_final_.pdf](http://www.ren21.net/wp-content/uploads/2018/06/17-8652_GSR2018_FullReport_web_final_.pdf)>. Access in: 4 June 2019.

ROHSENOW, W. M.; GARTNETT, J. P.; CHO, Y. I. **Handbook of Heat Transfer**. 3. ed. ISBN 0-07-053555-8. McGraw-Hill, 1998.

SAMANES, J.; GARCÍA-BARBERENA, J.; ZAVERSKY, F. Modeling Solar Cavity

Receivers: A Review and Comparison of Natural Convection Heat Loss Correlations.

Energy Procedia, v. 69, p. 543–552, 2015. Available in:

<<http://dx.doi.org/10.1016/j.egypro.2015.03.063>>.

SCHLIPF, D.; STENGLIN, M.; SCHNEIDER, G. **THERMAL STORAGE CSP**

TECHNOLOGY: STATE OF THE ART AND MARKET OVERVIEW. Available in:

<[http://energiaheliotermica.gov.br/pt-](http://energiaheliotermica.gov.br/pt-br/system/files/papers/2014_schlipf_thermal_storage_csp_technology.pdf)

[br/system/files/papers/2014_schlipf_thermal_storage_csp_technology.pdf](http://energiaheliotermica.gov.br/pt-br/system/files/papers/2014_schlipf_thermal_storage_csp_technology.pdf)>. Access

in: 9 Jan. 2018.

SEGAL, A. **OPTICS OF SOLAR CONCENTRATORSSFERA Summer School**.

Odeillo, 2010.

SEGAL, A.; EPSTEIN, M. Comparative performances of “tower-top” and “tower-

reflector” central solar receivers. **Solar Energy**, v. 65, n. 4, p. 207–226, 1999.

SHARMA, A. K. et al. Solar industrial process heating: A review. **Renewable and**

Sustainable Energy Reviews, v. 78, n. December 2016, p. 124–137, 2017.

SIEBERS, D. L.; KRAABEL, J. S. **Estimating convective energy losses from solar**

central receivers. Available in: <<http://www.osti.gov/scitech/biblio/6906848>>. Access

in: 12 fev. 2019.

SIEGEL, R. **Net Radiation Method for Enclosure Systems Involving Partially**

Transparte Walls. NASA Technical Note. Washington D.C., 1973.

SORIA, R.; SCHAEFFER, R.; SZKLO, A. **CONFIGURAÇÕES PARA OPERAÇÃO DE PLANTAS HELIOTÉRMICAS CSP COM ARMAZENAMENTO DE CALOR E HIBRIDIZAÇÃO NO BRASIL**. In: V Congresso Brasileiro de Energia Solar, Recife. Anais... Recife: Plataforma Energia Heliotérmica, 2014. Available in: <http://energiaheliotermica.gov.br/pt-br/system/files/papers/2017_ramirez_road_map_for_creation_of_advanced_meteorological_data_sets.pdf>.

STEINFELD, A.; SCHUBNELL, M. Optimum aperture size and operating temperature of a solar cavity-receiver. **Solar Energy**, v. 50, n. 1, p. 19–25, 1993.

STEINFELD, A.; Z'GRAGGEN, A. **Radiation Heat Transfer Lectures in Fall 10**. Zürich. ETH Zurich, 2010.

STINE, W. B.; MCDONALD, C. G. **Cavity Receiver Convective Heat Loss**. In: Proceedings of International Solar Energy Society Solar World Congress, Kobe, Japan. Anais... Kobe, Japan: 1989.

TAUMOEFOLOU, T. et al. Experimental Investigation of Natural Convection Heat Loss From a Model Solar Concentrator Cavity Receiver. **Journal of Solar Energy Engineering**, v. 126, n. 2, p. 801, 2004. Available in: <<http://solarenergyengineering.asmedigitalcollection.asme.org/article.aspx?articleid=1457030>>.

THIRUMALAI, N. C. et al. **Global Review of Solar Tower Technology**. [s.l: s.n.]. Available in: <<https://www.seriius.org/pdfs/global-review-solar-tower-technology.pdf>>. Access in: 30 Jan. 2019.

TIBA, C. et al. Metodologia para elaboração de mapas de radiação solar para Minas Gerais. **V Congresso Brasileiro de Energia Solar**, p. 10, 2014. Available in: <http://energiaheliotermica.gov.br/pt-br/system/files/papers/2014_tiba_metodologia_para_elaboracao_de_mapas.pdf>.

VIANA, T. S. et al. Assessing the potential of concentrating solar photovoltaic generation in Brazil with satellite-derived direct normal irradiation. **Solar Energy**, v. 85, n. 3, p. 486–495, 2011.

WAGNER, M. J. **Simulation and Predictive Performance Modeling of Utility-**

Scale Central Receiver System Power Plants. 2008. University of Wisconsin-Madison, Madison, 2008. Available in:
<<http://sel.me.wisc.edu/publications/theses/wagner08.zip>>.

WAN, Z. et al. Experimental study on thermal performance of a water/steam cavity receiver with solar simulator. **Energy Procedia**, v. 142, p. 265–270, 2017. Available in: <<https://doi.org/10.1016/j.egypro.2017.12.042>>.

WINSTON, R.; MIÑANO, J. C.; BENÍTEZ, P. NONIMAGING OPTICAL SYSTEMS. In: **Nonimaging Optics**. 1. ed. Burlington: Elsevier, 2005. p. 43–68.

WU, S. Y. et al. Experimental investigation on heat loss of a fully open cylindrical cavity with different boundary conditions. **Experimental Thermal and Fluid Science**, v. 45, p. 92–101, 2013. Available in:
<<http://dx.doi.org/10.1016/j.expthermflusci.2012.10.010>>.

Z'GRAGGEN, A.; STEINFELD, A. Radiative Exchange Within a Two-Cavity Configuration With a Spectrally Selective Window. **Journal of Solar Energy Engineering**, v. 126, n. 2, p. 819, 2004. Available in:
<<http://solarenergyengineering.asmedigitalcollection.asme.org/article.aspx?articleid=1457038>>.

Appendix A

The heliostat field coordinates in relation to the tower Cartesian position (x;y = 0;0).

Heliostat #	X axis (North+)	Y axis (East+)
1	-24.15	3.518
2	-24.15	-3.518
3	-28.48	0
4	-19.82	6.82
5	-24.15	10.55
6	-19.82	-6.82
7	-19.82	0
8	-19.82	13.64
9	-28.48	7.25
10	-24.15	-10.55
11	-28.48	-7.25
12	-19.82	-13.64
13	-15.49	16.51
14	-15.49	3.303
15	-15.49	9.908
16	-15.49	-9.908
17	-15.49	-3.303
18	-19.82	20.46
19	-24.15	17.59
20	-15.49	-16.51
21	-11.16	19.17
22	-24.15	-17.59
23	-15.49	23.12
24	-32.81	3.732
25	-11.16	-19.17
26	-11.16	12.78
27	-6.83	21.62
28	-32.81	-3.732
29	-28.48	14.5
30	-19.82	-20.46
31	-11.16	-12.78
32	-2.5	23.85
33	-11.16	6.391
34	-6.83	-21.62

35	11.16	15.98
36	-11.16	25.56
37	-28.48	-14.5
38	2.5	20.86
39	-11.16	-6.391
40	-15.49	-23.12
41	-2.5	-23.85
42	-2.5	17.88
43	2.5	-20.86
44	-6.83	15.44
45	11.16	-15.98
46	-11.16	-25.56
47	6.83	18.53
48	-6.83	-15.44
49	-2.5	-17.88
50	6.83	-18.53

Appendix B

Solar field efficiency as function of solar angles.

Azimuth (γ_{az})	Elevation (φ_{el})	Total efficiency (η_{sf})	Section 1 ($\eta_{A_{ap1}}$)	Section 2 ($\eta_{A_{ap2}}$)
30	15	0.493	0.309	0.184
30	30	0.691	0.419	0.272
30	45	0.764	0.456	0.308
30	60	0.800	0.467	0.333
30	75	0.812	0.466	0.346
60	15	0.795	0.595	0.200
60	30	0.548	0.291	0.257
60	45	0.676	0.392	0.284
60	60	0.718	0.395	0.323
60	75	0.779	0.438	0.341
90	15	0.800	0.645	0.155
90	30	0.458	0.195	0.231
90	45	0.636	0.326	0.263
90	60	0.683	0.350	0.310
90	75	0.753	0.604	0.333
120	15	0.783	0.588	0.149
120	30	0.482	0.187	0.195
120	45	0.580	0.254	0.243
120	60	0.656	0.431	0.295
120	75	0.725	0.442	0.326
150	45	0.768	0.448	0.225
150	60	0.795	0.516	0.283
150	75	0.633	0.349	0.320
180	60	0.705	0.384	0.279
180	75	0.757	0.603	0.319
210	45	0.702	0.546	0.226
210	60	0.756	0.524	0.284
210	75	0.649	0.449	0.321
240	15	0.716	0.46	0.154
240	30	0.763	0.474	0.200
240	45	0.522	0.181	0.244
240	60	0.620	0.439	0.296
240	75	0.679	0.410	0.327
270	15	0.742	0.432	0.156
270	30	0.776	0.445	0.232
270	45	0.481	0.163	0.264
270	60	0.668	0.328	0.312
270	75	0.707	0.359	0.334
300	15	0.774	0.435	0.200
300	30	0.792	0.792	0.256
300	45	0.562	0.562	0.289
300	60	0.693	0.693	0.328
300	75	0.748	0.748	0.341
330	15	0.803	0.803	0.181
330	30	0.807	0.807	0.269
330	45	0.496	0.496	0.310
330	60	0.696	0.696	0.331
330	75	0.782	0.782	0.346
360	45	0.805	0.805	0.318
360	60	0.816	0.816	0.340

360	75	0.788	0.788	0.348
360	90	0.818	0.818	0.339

Appendix C

First spectral band:

- $\lambda_1 = 0 \text{ } \mu\text{m}$ and $\lambda_2 = 0.1 \text{ } \mu\text{m}$, for $\lambda T \leq 750 \cdot 10^{-6} \text{ } \mu\text{m}\cdot\text{K}$:

$$e_{\lambda b}(T_c)|_0^{0.1} = \sigma T_c^4 * (2.29 \cdot 10^{-15} * e^{0.02893 * \lambda_2 T_c} - 2.29 \cdot 10^{-15} * e^{0.02893 * \lambda_1 T_c})$$

$$e_{\lambda b}(T_w)|_0^{0.1} = \sigma T_w^4 * (2.29 \cdot 10^{-15} * e^{0.02893 * \lambda_2 T_w} - 2.29 \cdot 10^{-15} * e^{0.02893 * \lambda_1 T_c})$$

$$= \sigma(0.6(T_c - T_\infty) + T_\infty)^4$$

$$* (2.29 \cdot 10^{-15} * e^{0.02893 * \lambda_2 * (0.6(T_c - T_\infty) + T_\infty)} - 2.29 \cdot 10^{-15} * e^{0.02893 * \lambda_1 * (0.6(T_c - T_\infty) + T_\infty)})$$

- $\lambda_1 = 0 \text{ } \mu\text{m}$ and $\lambda_2 = 0.1 \text{ } \mu\text{m}$, for $750 \cdot 10^{-6} \text{ } \mu\text{m}\cdot\text{K} < \lambda T \leq 1,100 \cdot 10^{-6} \text{ } \mu\text{m}\cdot\text{K}$:

$$e_{\lambda b}(T_c)|_0^{0.1} = \sigma T_c^4 * (8.26 \cdot 10^{-9} * e^{0.01056 * \lambda_2 T_c} - 8.26 \cdot 10^{-9} * e^{0.01056 * \lambda_1 T_c})$$

$$e_{\lambda b}(T_w)|_0^{0.1} = \sigma T_w^4 * (8.26 \cdot 10^{-9} * e^{0.01056 * \lambda_2 T_w} - 8.26 \cdot 10^{-9} * e^{0.01056 * \lambda_1 T_c})$$

$$= \sigma(0.6(T_c - T_\infty) + T_\infty)^4$$

$$* (8.26 \cdot 10^{-9} * e^{0.01056 * \lambda_2 * (0.6(T_c - T_\infty) + T_\infty)} - 8.26 \cdot 10^{-9} * e^{0.01056 * \lambda_1 * (0.6(T_c - T_\infty) + T_\infty)})$$

- $\lambda_1 = 0 \text{ } \mu\text{m}$ and $\lambda_2 = 0.1 \text{ } \mu\text{m}$, for $1,100 \cdot 10^{-6} \text{ } \mu\text{m}\cdot\text{K} < \lambda T \leq 1,600 \cdot 10^{-6} \text{ } \mu\text{m}\cdot\text{K}$:

$$e_{\lambda b}(T_c)|_0^{0.1} = \sigma T_c^4 * (1.90 \cdot 10^{-25} * \lambda_2 T_c^{7.185} - 1.90 \cdot 10^{-25} * \lambda_1 T_c^{7.185})$$

$$e_{\lambda b}(T_w)|_0^{0.1} = \sigma T_w^4 * (1.90 \cdot 10^{-25} * \lambda_2 T_w^{7.185} - 1.90 \cdot 10^{-25} * \lambda_1 T_w^{7.185})$$

$$= \sigma(0.6(T_c - T_\infty) + T_\infty)^4 * (1.90 \cdot 10^{-25} * \lambda_2 * (0.6(T_c - T_\infty) + T_\infty)^{7.185} - 1.90 \cdot 10^{-25}$$

$$* \lambda_1 * (0.6(T_c - T_\infty) + T_\infty)^{7.185})$$

Second spectral band:

- $\lambda_1 = 0.1 \text{ } \mu\text{m}$ and $\lambda_2 = 3 \text{ } \mu\text{m}$, for $\lambda T \leq 750 \cdot 10^{-6} \text{ } \mu\text{m}\cdot\text{K}$:

$$e_{\lambda b}(T_c)|_{0.1}^3 = \sigma T_c^4 * (2.29 \cdot 10^{-15} * e^{0.02893 * \lambda_2 T_c} - 2.29 \cdot 10^{-15} * e^{0.02893 * \lambda_1 T_c})$$

$$e_{\lambda b}(T_w)|_{0.1}^3 = \sigma T_w^4 * (2.29 \cdot 10^{-15} * e^{0.02893 * \lambda_2 T_w} - 2.29 \cdot 10^{-15} * e^{0.02893 * \lambda_1 T_c})$$

$$= \sigma(0.6(T_c - T_\infty) + T_\infty)^4$$

$$* (2.29 \cdot 10^{-15} * e^{0.02893 * \lambda_2 * (0.6(T_c - T_\infty) + T_\infty)} - 2.29 \cdot 10^{-15} * e^{0.02893 * \lambda_1 * (0.6(T_c - T_\infty) + T_\infty)})$$

- $\lambda_1 = 0.1 \text{ } \mu\text{m}$ and $\lambda_2 = 3 \text{ } \mu\text{m}$, for $750 \cdot 10^{-6} \text{ } \mu\text{m}\cdot\text{K} < \lambda T \leq 1,100 \cdot 10^{-6} \text{ } \mu\text{m}\cdot\text{K}$:

$$e_{\lambda b}(T_c)|_{0.1}^3 = \sigma T_c^4 * (8.26 \cdot 10^{-9} * e^{0.01056 * \lambda_2 T_c} - 8.26 \cdot 10^{-9} * e^{0.01056 * \lambda_1 T_c})$$

$$e_{\lambda b}(T_w)|_{0.1}^3 = \sigma T_w^4 * (8.26 \cdot 10^{-9} * e^{0.01056 * \lambda_2 T_w} - 8.26 \cdot 10^{-9} * e^{0.01056 * \lambda_1 T_c})$$

$$= \sigma(0.6(T_c - T_\infty) + T_\infty)^4$$

$$* (8.26 \cdot 10^{-9} * e^{0.01056 * \lambda_2 * (0.6(T_c - T_\infty) + T_\infty)} - 8.26 \cdot 10^{-9} * e^{0.01056 * \lambda_1 * (0.6(T_c - T_\infty) + T_\infty)})$$

- $\lambda_1 = 0.1 \text{ } \mu\text{m}$ and $\lambda_2 = 3 \text{ } \mu\text{m}$, for $1,100 \cdot 10^{-6} \text{ } \mu\text{m}\cdot\text{K} < \lambda T \leq 1,600 \cdot 10^{-6} \text{ } \mu\text{m}\cdot\text{K}$:

$$e_{\lambda b}(T_c)|_{0.1}^3 = \sigma T_c^4 * (1.90 \cdot 10^{-25} * \lambda_2 T_c^{7.185} - 1.90 \cdot 10^{-25} * \lambda_1 T_c^{7.185})$$

$$\begin{aligned}
e_{\lambda b}(T_w)|_{0.1}^3 &= \sigma T_w^4 * (1.90.10^{-25} * \lambda_2 T_w^{7.185} - 1.90.10^{-25} * \lambda_1 T_w^{7.185}) \\
&= \sigma(0.6(T_c - T_\infty) + T_\infty)^4 * (1.90.10^{-25} * \lambda_2 * (0.6(T_c - T_\infty) + T_\infty)^{7.185} - 1.90.10^{-25} \\
&\quad * \lambda_1 * (0.6(T_c - T_\infty) + T_\infty)^{7.185})
\end{aligned}$$

Third spectral band:

- $\lambda_1 = 3 \mu\text{m}$ and $\lambda_2 = \infty \mu\text{m}$, for $\lambda T \leq 750.10^{-6} \mu\text{m.K}$:

$$e_{\lambda b}(T_c)|_{0.1}^3 = \sigma T_c^4 * (1 - 2.29.10^{-15} * e^{0.02893 * \lambda_1 T_c})$$

$$\begin{aligned}
e_{\lambda b}(T_w)|_{0.1}^3 &= \sigma T_w^4 * (1 - 2.29.10^{-15} * e^{0.02893 * \lambda_1 * 0.6(T_c - T_\infty) + T_\infty}) \\
&= \sigma(0.6(T_c - T_\infty) + T_\infty)^4 * (1 - 2.29.10^{-15} * e^{0.02893 * \lambda_1 * (0.6(T_c - T_\infty) + T_\infty)})
\end{aligned}$$

- $\lambda_1 = 3 \mu\text{m}$ and $\lambda_2 = \infty \mu\text{m}$, for $750.10^{-6} \mu\text{m.K} < \lambda T \leq 1,100 .10^{-6} \mu\text{m.K}$:

$$e_{\lambda b}(T_c)|_{0.1}^3 = \sigma T_c^4 * (1 - 8.26.10^{-9} * e^{0.01056 * \lambda_1 T_c})$$

$$\begin{aligned}
e_{\lambda b}(T_w)|_{0.1}^3 &= \sigma T_w^4 * (1 - 8.26.10^{-9} * e^{0.01056 * \lambda_1 T_c}) \\
&= \sigma(0.6(T_c - T_\infty) + T_\infty)^4 * (1 - 8.26.10^{-9} * e^{0.01056 * \lambda_1 * (0.6(T_c - T_\infty) + T_\infty)})
\end{aligned}$$

- $\lambda_1 = 3 \mu\text{m}$ and $\lambda_2 = \infty \mu\text{m}$, for $1,100.10^{-6} \mu\text{m.K} < \lambda T \leq 1,600 .10^{-6} \mu\text{m.K}$:

$$e_{\lambda b}(T_c)|_{0.1}^3 = \sigma T_c^4 * (1 - 1.90.10^{-25} * \lambda_1 T_c^{7.185})$$

$$\begin{aligned}
e_{\lambda b}(T_w)|_{0.1}^3 &= \sigma T_w^4 * (1 - 1.90.10^{-25} * \lambda_1 T_w^{7.185}) \\
&= \sigma(0.6(T_c - T_\infty) + T_\infty)^4 * (1 - 1.90.10^{-25} * \lambda_1 * (0.6(T_c - T_\infty) + T_\infty)^{7.185})
\end{aligned}$$

Appendix D

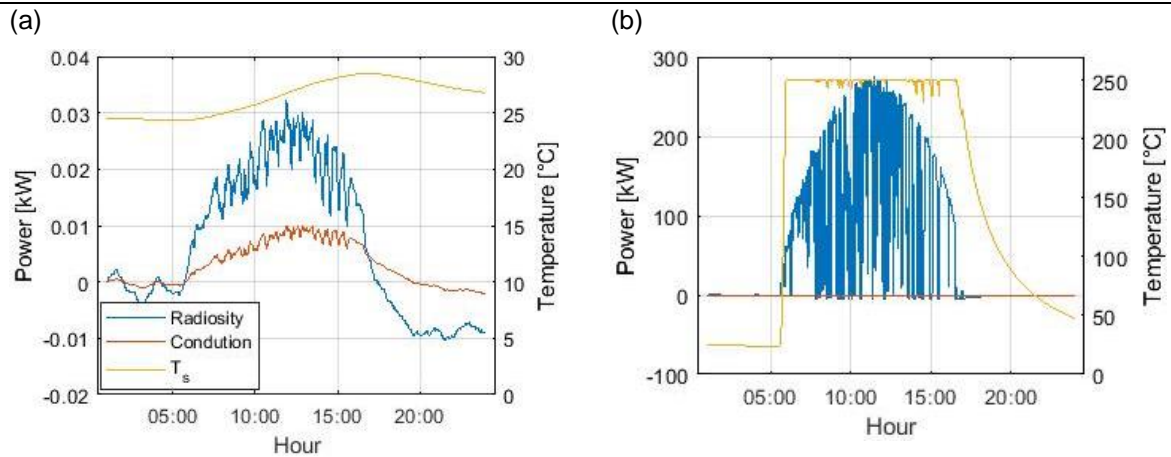
- Opaque window optical properties:

Spectral band [μm]	E_λ	R_λ	V_λ
0-0.1	0.85	0.15	0.00
0.1-3	0.85	0.15	0.00
3- ∞	0.85	0.15	0.00

- Transparent window optical properties:

Spectral band [μm]	E_λ	R_λ	V_λ
0-0.1	0.005	0.005	0.99
0.1-3	0.005	0.005	0.99
3- ∞	0.005	0.005	0.99

- Temperature behavior, radiation and thermal losses for (a) the opaque, and (b) transparent windows:



- Efficiency comparison between windows.

	Quartz Window	Opaque Window	Transparent Window
η	83.87%	0.00%	84.04%